INVESTIGATION OF AIR BUBBLE MOTION IN WATER THROUGH A VERTICAL NARROW RECTANGULAR CHANNEL BY USING IMAGE PROCESSING TECHNIQUES

Sancak ÖZDEMİR

AUGUST 2005

INVESTIGATION OF AIR BUBBLE MOTION IN WATER THROUGH A VERTICAL NARROW RECTANGULAR CHANNEL BY USING IMAGE PROCESSING TECHNIQUES

A THESIS SUBMITTED TO
THE GRADUATE SCHOOL OF NATURAL AND APPLIED SCIENCES
OF
MIDDLE EAST TECHNICAL UNIVERSITY

BY

SANCAK ÖZDEMİR

IN PARTIAL FULFILLMENT OF THE REQUIREMENTS
FOR
THE DEGREE OF DOCTOR OF PHILOSOPHY
IN
MECHANICAL ENGINEERING

AUGUST 2005

Approval of the Graduate School of Natural and Applied Sciences

Prof.Dr. Canan ÖZGEN
Director

I certify that this thesis satisfies all the requirements as a thesis for the degree of Doctor of Philosophy.

Prof.Dr. Kemal İDER
Head of Department

This is to certify that we have read this thesis and that in our opinion it is fully adequate, in scope and quality, as a thesis for the degree of Doctor of Philosophy.

Prof. Dr. A. Orhan YEŞİN
Supervisor

Examining Committee Members

Prof. Dr. Ediz PAYKOÇ (METU, ME) _____

Prof. Dr. Orhan YEŞİN (METU, ME) _____

Prof. Dr. Kahraman ALBAYRAK (METU, ME) _____

Prof. Dr. Nafiz ALEMDAROĞLU (METU, AEE) _____

Prof. Dr. L. Berrin ERBAY (Osmangazi Unv.) _____

I hereby declare that all information in this document has been obtained and presented in accordance with academic rules and ethical conduct. I also declare that, as required by these rules and conduct, I have fully cited and referenced all material and results that are not original to this work.

Name, Last name : Sancak Özdemir

Signature :

ABSTRACT

INVESTIGATION OF AIR BUBBLE MOTION IN WATER THROUGH A VERTICAL NARROW RECTANGULAR CHANNEL BY USING IMAGE PROCESSING TECHNIQUES

Özdemir, Sancak

Ph.D., Department of Mechanical Engineering

Supervisor: Prof. Dr. A. Orhan YEŞİN

August 2005, 133 pages

This thesis presents the study of air bubble motion in stagnant water and in upward flowing water through a vertical narrow rectangular channel of 2.1X66.5 mm cross section by using image processing and analyzing techniques. The investigated bubble size range is 2 - 70 mm in area equivalent bubble diameter and mean water flow velocity is 0-25 cm/s. This study focuses on the quantitative assessment of bubble size (perimeter, area, volume, width and height), shape, path and rising velocity.

The observed bubble shapes consist of circular, ellipse, ellipse wobbling, hat wobbling, cap-hat, cap and cap-bullet types. Ellipse wobbling and hat wobbling type bubble region show transition from ellipsoidal to circular cap region.

The results of the ellipse bubble tests were compared with the rise velocity correlation of ellipsoidal bubbles in infinite medium and an empirical correlation for two dimensional ellipse bubbles was obtained. The cap bubble rise velocities measured in this study were compared with the correlations in literature and a new

empirical correlation which is different from those given in the literature was obtained from the experimental results of this study.

The trends of the cap bubble deformation which is defined as bubble height to bubble width ratio, for various water streams are almost similar in behavior. Therefore, a correlation was obtained from the measured cap bubble deformation values in water stream.

The experimental results show that the bubble relative velocity under co-current flow conditions for area equivalent bubble diameter to channel width ratio, $\lambda_{ae}<0.6$ is less than that under stagnant water condition. After bubble shapes reach to the slug type ($\lambda_{ae} \geq 0.6$), relative bubble velocities pass over the terminal bubble velocities in stagnant water. If the water velocity is increased further, the bubble relative velocity increases in the slug bubble region. Rising velocities of slug bubbles were analyzed using the experimental data and a new correlation for slug bubble rise velocity was proposed for flowing water condition.

Keywords: Bubble Motion, Bubble Rising Velocity, Narrow Rectangular Channel, Bubble Shape, Bubble Path

ÖZ

DİKEY DAR DİKDÖRTGEN BİR KANALDA SU İÇİNDE HAVA KABARCIĞI HAREKETİNİN GÖRÜNTÜ İŞLEME TEKNİKLERİ KULLANILARAK İNCELENMESİ

Özdemir, Sancak

Doktora, Makina Mühendisliği Bölümü

Tez Yöneticisi: Prof. Dr. A. Orhan YEŞİN

Ağustos 2005, 133 sayfa

Bu tezde, kesiti 2.1x66.5 mm olan dikey dar dikdörtgen bir kanal boyunca durgun suda ve yukarı yönde akan suda hava kabarcığı hareketinin görüntü işleme ve analiz teknikleri kullanılarak incelenmesi sunulmaktadır. İncelenen kabarcık boyutu aralığı, alan eşdeğeri kabarcık çapı olarak 2-70 mm ve ortalama su akış hızı 0-25 cm/s dir. Bu çalışma kabarcık boyutunun (çevre, alan, hacim, genişlik ve yükseklik), şeklinin, izlediği yolun ve yükselme hızının nicel olarak incelenmesi üzerine odaklanmıştır.

Gözlemlenen kabarcık şekilleri dairesel, eliptik, salınan eliptik, salınan şapka, şapka-kasket, kasket ve mermi-kasket tiplerinden oluşmaktadır. Salınan eliptik ve salınan şapka tipli kabarcık bölgesi eliptik bölgeden dairesel kasket bölgesine geçişi göstermektedir.

Eliptik kabarcık deneylerinin sonuçları, sonsuz ortamdaki eliptik kabarcıkların yükselme hızı eşilişkisiyle karşılaştırılarak, iki boyutlu eliptik kabarcıklar için bir eşilişki elde edilmiştir. Bu çalışmada ölçülen kasket tipi kabarcıkların yükselme

hızları literatürdeki eşilişkiler ile karşılaştırılmış ve literatürde verilenlerden farklı bir eşilişki elde edilmiştir.

Kabarcık yüksekliğinin enine oranı olarak tanımlanan kasket tipi kabarcık deformasyonun, farklı hızlarda akan su içindeki davranış eğilimleri birbirine oldukça benzemektedir. Bu nedenle, ölçülen kasket tipi kabarcık deformasyonu değerlerinden bir eşilişki elde edilmiştir.

Deneysel sonuçlar, alan eşdeğeri kabarcık çapının (λ_{ae}) kanal genişliğine oranının 0.6 dan küçük olduğu durumlar için aynı yönlü su akış koşullarında kabarcığın göreceli hızının durgun su koşullarına göre daha az olduğunu göstermektedir. Kabarcık şeklinin karma tipe dönüşmesinden sonra, ($\lambda_{ae} \geq 0.6$) göreceli kabarcık hızları durgun sudaki kabarcık sınır hızlarını geçmektedir. Eğer su hızı daha fazla artırılırsa, kabarcığın göreceli hızı karma tipli kabarcık bölgesinde daha fazla artmaktadır. Karma tipli kabarcıkların yükselme hızları deneylerden elde edilen veriler kullanılarak analiz edilmiş ve akan su içindeki kabarcık hareketi için yeni bir eşilişki önerilmiştir.

Anahtar Kelimeler: Kabarcık Hareketi, Kabarcık Yükselme Hızı, Dar Dikdörtgen Kanal, Kabarcık Şekli, Kabarcık Yolu

To My Family

ACKNOWLEDGMENTS

I express my gratitude to Prof. Dr. Orhan Yeşin for his guidance, encouragement and insight throughout the research.

I would like to thank to Prof. Dr. Kahraman Albayrak and Prof. Dr. Nafiz Alemdaroğlu, members of my Ph.D. Progress Committee, for their invaluable suggestions and comments.

I would also like to thank to Prof. Dr. Kaichiro Mishima from Kyoto University, Japan who provided me important reports and encouraged me with his valuable suggestions.

Furthermore, I would like to express my appreciation to the technical staffs Mr. İbrahim Özdemir and Mr. Mehmet Erilli in Mechanical Engineering Department for their considerable assistance provided during the construction of the experimental facility.

I would like to extend my thanks to the management of Turkish Atomic Energy Authority for their continued support.

Finally, I wish to express my special thanks to my wife and to my children for their patience, understanding and morale support.

TABLE OF CONTENTS

LIST OF TABLES

TABLES

LIST OF FIGURES

FIGURES

LIST OF SYMBOLS

A	Area [m^2]
C	Circularity [-]
D	Channel diameter [m]
D_h	Channel hydraulic diameter ($4A/P$) [m]
E	Minor semi-axis of ellipse/ Major semi-axis of ellipse [-]
$Eö$	Eötvös Number [-]
Fr	Froude Number [-]
$\vec{F}$	Force vector [N]
G	Channel gap [m]
Mo	Morton Number [-]
P	Perimeter [m]
R	Radius [m]
Re	Reynolds Number [-]
S	Surface [m^2]
U	Velocity [m/s]
U_{bvc}	Bubble vertical center of mass velocity [m/s]
U_{blc}	Bubble lateral center of mass velocity [m/s]
U_{btc}	Bubble tangential center of mass velocity [m/s]
U_{bvn}	Bubble vertical nose velocity [m/s]
U_{bln}	Bubble lateral nose velocity [m/s]
U_{btn}	Bubble tangential nose velocity [m/s]
U_l	Mean liquid velocity [m/s]
V	Volume [m^3]
W	Channel width [m]
We	Weber number [-]
$\vec{X}$	X vector [-]
a	Major semi-axis of ellipse [m]
b	Minor semi-axis of ellipse [m]
c	Radius of curvature[m^{-1}]
d	Bubble diameter [m]

g	Gravitational constant [m/s^2]
h	Bubble height [m]
k	sum of the two principal curvatures [m^{-1}]
m	Mass, bubble aspect ratio (h/w) [kg, -]
$\vec{n}$	Unit normal vector [-]
w	Bubble width [m]

Subscripts

B	Buoyancy
D	Drag
G	Gravitational
L	Lift
P	Pressure
T	Terminal
VM	Virtual mass (or added mass)
ae	Area equivalent
b	Bubble
br	Bubble-relative
e	Equivalent
fd	Form drag
g	Quantities of gas
h	Hydraulic
l	Quantities of liquid
pe	Perimeter equivalent
s	Static
st	Surface tension
tot	Total
ve	Volume equivalent
vis	Viscous
z	Vertical direction
∞	Infinite medium

Greek letters

α	Void fraction [-]
δ	Uncertainty
θ	Wake angle [rad]

λ_{ae}	Area equivalent bubble diameter/ channel width [-]
λ_{ve}	Area equivalent bubble diameter/channel diameter [-]
μ	Dynamic viscosity [kg/ms]
v	Kinematic viscosity [m^2/s]
σ	Surface tension [kg/s^2]
ρ	Density [kg/m^3]
τ	Stress tensor [kg/ ms^2]

CHAPTER 1

INTRODUCTION

1.1 Objective of the thesis

An important topic in fluid dynamics is two-phase flows. Two-phase flows can be found in many engineering fields, e.g. nuclear, mechanical, aerospace, biomedical, chemical, electrical, and environmental engineering. There is an enormous variation in applications, e.g. rocket engines, chemical reactors, two-phase mixture transport, ink-jet printing, particle transport in blood, and two-phase cooling.

Adiabatic gas-liquid two-phase flow and vapor-liquid phase-change processes play an important role in a wide variety of technological applications, specifically in nuclear reactor engineering and chemical engineering. In addition, a better understanding of two-phase flow is of critical importance for nuclear power plant design [1].

Fluid flow channels of non-circular cross-section are used to cool the equipment in nuclear technology, power engineering, microelectronics, air and spacecrafts. They cover a wide range of sizes from one micrometer to several millimeters [2].

Sufficient knowledge on the gas bubble motion in a dispersed gas-liquid two-phase flow is indispensable for establishing a reliable mathematical model to describe the flow dynamics [3].

Computational research on bubble motion has become feasible only in the last few decades. Many numerical models are based on some simplifications and assumptions. For instance, bubbles are restricted to simple shapes such as spheres, spherical caps, or spheroids, and the motion of a bubble is often assumed to be steady or quasi-steady [4].

Any improvement in understanding the bubble motion will be used not only to extend the currently available database of empirical correlations, but more importantly, to assist in the development of advanced computational tools. Once developed and validated against experimental results, these tools will be invaluable in aiding designers to develop new, more efficient, engineered systems [5]. The wide range of difference in the velocity magnitude and orientation of bubble must be captured by an experimental or computational tool in order to be able to fully predict the behavior of a single bubble rising in stagnant and flowing water.

Computational Fluid Dynamics (CFD) applications related to bubble motion can be found in recent literature [3, 6-11]. It should be noted that CFD and other numerical methods are still under development in many ways and will continue to be so for the foreseeable future. In addition, experimental and empirical methods are also still being developed further. All of these methods are complementary and beneficial to each other.

It is essential that mathematical models are to be formulated which should clearly be based on the physical understanding of two-phase flow processes and should be supported by experimental data.

Continuing advances in computational methods for prediction of gas-liquid two phase flow characteristics necessitates the development of a comprehensive experimental database to support mechanistic modeling and code qualification. In order to validate the results of CFD simulations, some quantitative experimental data are required [4].

More recently there has been much interest in the development of non-intrusive methods for both local and average property measurements. The non-intrusive methods are implemented by means of imaging techniques, Doppler frequency-shift techniques or tomography techniques. The imaging techniques include high-speed photography (the most commonly used one), ultrasonic imaging and more advanced techniques using particle imaging velocimetry (PIV) [4]. In the last ten years a considerable development in the local two-phase flow measurements, flow visualization techniques and tomography has been recorded.

Bubble motion is highly complex with an unsteady nature, showing wide variations in bubble shape. Although it has been extensively studied in the past; however, certain aspects of bubble motion still remain poorly understood, due to lack of experimental data in narrow rectangular channels under stagnant and flowing water conditions. Two-phase flows in narrow passages are of great importance in nuclear and microelectronic industries [12]. However, very little data on narrow rectangular ducts have been published in the open literature [13].

The models incorporated for the forces acting on bubbles are usually based on spherical bubbles, while the shape of most bubbles in a channel is non-spherical [14]. As will be seen from the review of literature, very few studies have explored the underlying mechanisms of bubble dynamics associated with narrow channels.

Detailed literature review of two-phase flow regimes in small channels can be found in Wilmarth and Ishii [12]. Even though some work has been carried out on flow regimes in narrow channels, some conclusions are inconsistent and even confusing. The reason of it may be due to the flow regime definitions and the complicated flow structures [15]. In spite of receiving much attention over recent decades, the present state of knowledge for bubble motion in narrow channels is far from complete [16].

In this study, an experimental work was performed on adiabatic air bubble motion in stagnant water and upward flowing water through a vertical narrow channel based on visual observations by using image processing and analyzing techniques.

The principle objectives of the study described in this thesis can be designated as follows:

1. Classification of bubble shapes in a vertical narrow rectangular channel
2. Describing bubble path in stagnant water through a vertical narrow rectangular channel
3. Describing bubble path in upward flowing water through a vertical narrow rectangular channel

4. Determining rising velocities of the air bubbles in stagnant and flowing water through a vertical narrow rectangular channel
5. Evaluating the channel wall effects on the bubble motion in a vertical narrow rectangular channel
6. Comparison of bubble motion in circular channels and narrow rectangular channels

1.2 Importance of the present study

The major characteristic of the gas-liquid two-phase flow is the existence of the deformable interface and significant evolution of interfacial structures along the flow. In addition to their path-instability the bubbles may undergo large shape deformation and this oscillatory behavior of both path and shape of a bubble is often referred to as it is ‘‘wobbling’’ (see Table 5.3). These phenomena are not yet fully understood. In particular, the motion, the wake and the shape of bubbles are the subjects of active research [10].

Most of the models available for closure of the governing two-phase flow equations need the relative velocity between the liquid and gas to develop new models or refine existing models for relative gas velocity and in general, to understand the effect of bubbles of different size on relative gas velocity. Typically, relative velocity is determined through a drift flux correlation. The relative velocity is also a function of the void fraction and bubble size.

Many studies have been carried out to understand the rise of single Taylor bubbles through stagnant as well as flowing liquid. However, both theoretical analyses and experimental investigations have primarily been carried out for circular channels [17].

In relation to the cooling system of a high performance microelectronic system and of a high power research reactor with plate type fuel, the study of two phase flow in a narrow rectangular channel has been paid considerable attention recently [15]. It is anticipated that the characteristics of two-phase flow in such a narrow channel with a large aspect ratio differ from those in other channel geometries, because of

the significant restriction of the bubble shape, which, consequently, may affect the heat removal by boiling under abnormal operating conditions [15].

In Turkey, Çekmece Nuclear Training and Research Center has TR-2 nuclear research reactor which is a pool type reactor with 5 MW power. Plate type (MTR type) fuel elements and de-mineralized water coolant are used in this reactor. Figure 1.1 shows TR-2 reactor pool and reactor core.

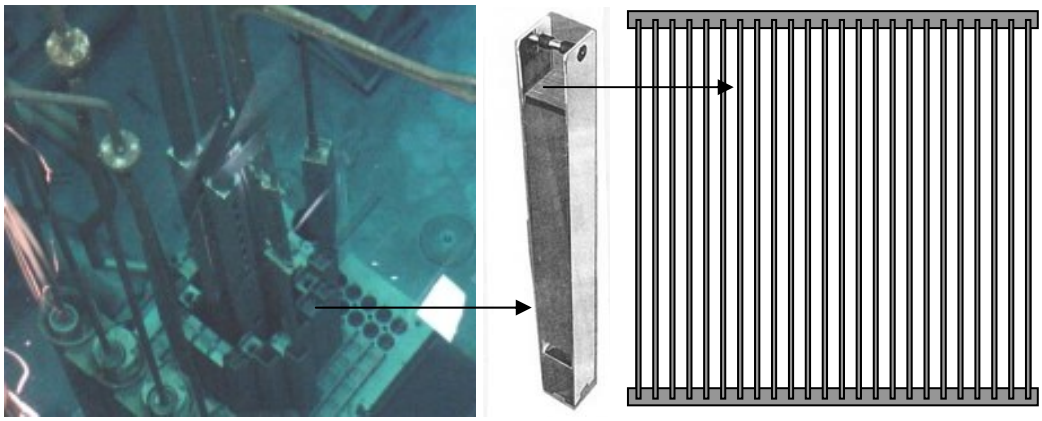

Figure 1.1 TR-2 Nuclear research reactor (upper view of reactor core (left), fuel assembly (middle) and upper view of fuel assembly (right)

The coolant channel of an MTR-type fuel element has a rectangular cross-sectional shape with a very narrow gap and a large aspect ration. It is anticipated that the characteristics of two-phase flow in such narrow slit differ from those in other channel geometries, because of the significant restriction of the bubble shape which, consequently may affect the heat removal by boiling under abnormal operating conditions [17].

The design of a plate type fuel element requires basic thermal-hydraulic information such as: the heat transfer regime at which onset of nucleate boiling (ONB) will occur, the pressure drop and flow rate through the fuel element, the departure from nucleate boiling (DNB), the conditions for flow instability, and the critical velocity beyond which the fuel plates will collapse [18].

As the power supplied to a coolant channel is increased, bubbles will be formed (sub-cooled boiling) first as small bubbles, then of large sizes. The larger bubbles eventually restrict the channel cross section, and force the liquid phase to accelerate in order to maintain to same mass flux down the channel. This acceleration, in turn, leads to an increased pressure drop which restricts flow further, enhancing the flow blockage. These phenomena are divergent and oscillatory under appropriate conditions, and associate bubble size or void fraction with the onset of flow instability [18].

Although there is not net void at the outlet of a MTR type fueled reactor, during some accident situations, boiling occurs throughout the fuel coolant channels. Neither steady-state nor transient behavior can be understood without a knowledge of two-phase flow fundamentals [19].

One of the fundamental aspects of two phase flow is the bubble motion. The importance of the bubble motion in vertical narrow channels in MTR type nuclear research reactors is obvious since such bubbles exist in a variety of two-phase flow situations, especially in accident conditions.

In this study, air bubbles are used to simulate steam bubbles because of simplification of visualization. The results of this study can be used quantitatively for air-water systems such as bubble columns. On the other hand, air-water system may simulate steam-water systems qualitatively, since heat and mass transfer between steam and water are disregarded, such as evaporation and condensation.

1.3 Scope of the thesis

To understand the fundamental mechanisms of two-phase flow in vertical narrow rectangular channels, first of all, an extensive review of the literature related to two-phase flow and bubble motion were conducted. With the information obtained from the design and operating parameters of the TR-2 nuclear research reactor, an experimental facility was designed and constructed. The test section of the experimental facility is one-to-one scale transparent model of a single coolant channel of TR-2 nuclear research reactor. A set of tests on the bubble

motion in stagnant water and in flowing water through a vertical narrow rectangular channel with 2.1X66.5 mm cross section was realized. The investigated bubble size range is 2 to 70 mm in area equivalent bubble diameter, and the water upward flow velocity is 0-25 cm/s.

It is generally accepted that the numerical techniques and models for laminar or turbulent flow implemented in CFD codes are well established and give reasonably good results for single-phase flow systems [20]. Therefore, three dimensional computational fluid dynamics (CFD) simulation of the test section was made and single phase flow liquid velocity profile was obtained in three directions.

In this study, image processing and analyzing techniques were used to study the behavior of air bubble motion. It focuses on the quantitative assessment of some basic parameters of bubbles such as size (perimeter, area, volume, width and height), shape, rising velocity and path. This method appears to be promising for determining the governing mechanisms of the bubble motion. The data collected by the image analysis software can be incorporated into the new models and computer codes currently under development.

Though there is a large variety of experimental data on rise velocity available in the literature for different bubble sizes and pipe diameters, it is difficult to compare the results of one group of authors with those of others because of: (1) differences in the physical properties of the liquids used in various studies, (2) presence of impurities in the liquid, and (3) the fact that each study is often restricted to a narrow bubble size range in a given pipe diameter [21].

In Chapter 2 of the thesis, a review of existing literature pertaining to previous experimental, theoretical, and numerical research on bubble motion is given. In Chapter 3, experimental facility, illumination system, image acquisition system and bubble generation system are explained. Chapter 4 deals with the image processing and analyzing techniques which are used in this study. In Chapter 5, experimental results of air bubble motion in a vertical narrow rectangular channel filled with stagnant water are explained and compared with the results of other works in the literature. The experimental results of air bubble motion in flowing water are

reported in Chapter 6. Finally, Chapter 7 is to summarize the important findings and conclusions of the study and it includes some suggestions for further research on bubble motion in narrow channels.

CHAPTER 2

THEORY AND LITERATURE OVERVIEW

2.1 General overview of the subject

Theory and literature overview on the characteristics of air-water two-phase channel flow including bubble motion and flow patterns in narrow channels are reviewed in this chapter.

First of all, dimensionless numbers related to bubble motion and forces acting on the bubble will be explained briefly. Then, some aspects of bubble motion such as bubble shape and path including bubble rising behavior through an open liquid pool which simulates infinite medium, circular channels and rectangular channels filled with stagnant liquid will be discussed. This will be followed by addressing the bubble motion in liquid stream through channels. The emphasis will be on the phenomena associated with narrow rectangular channels. Finally, wall effect on the bubble motion in channels will be reviewed.

Multidimensional two-phase flow models are based on Lagrangian or Eulerian approaches. In Lagrangian models, the continuity and momentum equations are solved for the continuous phase, and the trajectories of the dispersed phase are computed by solving the governing differential equations. When the concentration of the dispersed phase is high, it will affect the behavior of the continuous phase. Therefore, Lagrangian methods are limited to low concentrations of the dispersed phase [4]. Eulerian models are mainly classified as drift-flux and two-fluid models. In drift-flux models, the two phases are considered as a mixture and conservation equations are solved using the mixture properties. Two-fluid models treat the general case of modeling with each phase or component as a separate fluid with its own set of governing balance equations. In general, each phase has its own velocity,

temperature and pressure. In all these models, bubble velocity is one of the fundamental parameters. To define the bubble motion, some dimensionless numbers were derived from the analytical studies. Thus, before starting to give information about bubble motion, related dimensionless numbers and forces acting on the bubble will be explained in the next two sections.

2.2 Dimensionless numbers

Theoretical studies on the bubble shape and motion extensively benefit from the experimental data that give the bubble shape as a function of some dimensionless numbers.

Determination of bubble shapes as a function of the related dimensionless numbers has been studied experimentally for the last sixty years. However, most of the current available data are based on studies conducted for bubbles rising in stagnant water. Also, most of the data come from the experimental systems using non-purified water that contains surface-active contaminants (surfactants). It is known that the contamination in the liquid is an effective factor on the bubble shape. The other factor that may affect the bubble shape is the wall effect for the narrowly confined experimental systems [22].

Bubble rising behavior in a liquid, depends on the physical properties of the surrounding liquid. These are the density ρ, the dynamic viscosity μ and the surface tension σ. The bubble rises due to the buoyancy force which is related to the gravitational acceleration g and the volume of the bubble V [23]. For the case of gas bubbles rising through liquids the density and viscosity of the gas are generally much less than those of the liquid, such as air-water systems, so that $\Delta\rho/\rho$ may be taken as unity [24].

The (mean) terminal rise velocity of the bubble U_T is a function of 5 variables,

$$U_T = U_T (d_e, g, \rho, \mu, \sigma), \tag{2.1}$$

where d_e is equivalent bubble diameter, g is gravitational acceleration, ρ is density, μ is viscosity and σ is surface tension.

Figure 2.1 shows forces acting on the bubble and these forces will be explained in the next section.

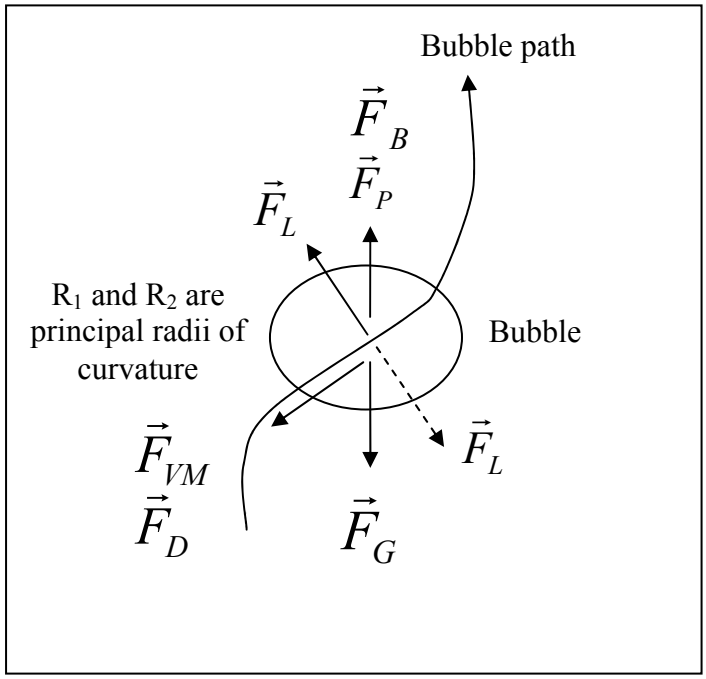

Figure 2.1 Forces acting on the bubble

Following the methodology of Celato *et al.* and starting from a general equation of bubble motion, related dimensionless numbers were obtained [25]:

$$\rho_g V_b \frac{d\vec{U}_b}{dt} = \int_{S_b} \Sigma_l \cdot \vec{n} dS + \rho_g V_b \vec{g} \tag{2.2}$$

where $\vec{U}_b$ is the velocity of the center of mass of the bubble, t time, S_b surface area of the bubble, Σ_l stress tensor acting on the bubble surface, $\vec{n}$ unit outward normal to the bubble surface and $\vec{g}$ is the acceleration of gravity. The dot product of stress tensor and unit normal for a bubble with constant surface tension σ is given by

$$\Sigma_l \cdot \vec{n} = -(P_l + \sigma k)\vec{n} + \tau_l \cdot \vec{n} \tag{2.3}$$

where P_l is the liquid pressure, τ_l viscous stress tensor and k is the sum of the two principal curvatures:

$$\tau_l = \mu_l \left(\Delta \vec{U}_l + \left(\Delta \vec{U}_l \right)^T \right) \tag{2.4}$$

$$k = \frac{1}{R_1} + \frac{1}{R_2} \tag{2.5}$$

where T denotes the transpose, R_1 and R_2 the radius of principal curvature of the bubble surface.

The pressure P_l can be split into two contributions; the static pressure P_s and the surface pressure P_{fd} causing the so-called form drag:

$$P_l = P_s + P_{fd} \tag{2.6}$$

Since the liquid phase is stagnant, the static pressure satisfies

$$0 = \Delta P_s + \rho_l \vec{g} \tag{2.7}$$

Substituting Eqs, 2.3, 2.6 and 2.7 into Eq. 2.2 yields

$$\rho_g V_b \frac{d\vec{U}_b}{dt} = \int_{S_b} \left[- P_{fd} \vec{n} - \sigma k \vec{n} + \tau_l \cdot \vec{n} \right] dS + \left(\rho_l - \rho_g \right) V_b \vec{g} \tag{2.8}$$

Under steady condition, using the order of magnitude method, each term in the above equation can be estimated as follows:

Unsteady force:

$$\rho_g V_b \frac{d\vec{U}_b}{dt} = 0 \tag{2.9}$$

Inertial force (form drag):

$$- \int_{S_b} P_{fd} \vec{n} dS \approx \rho_l U_T^2 d^2 \tag{2.10}$$

Surface tension force:

$$- \int_{S_b} \sigma k \vec{n} dS = - \int_{S_b} \sigma \left(\frac{1}{R_1} + \frac{1}{R_2} \right) \vec{n} dS \approx \frac{\sigma}{d} d^2 = \sigma d \tag{2.11}$$

Viscous force (skin friction):

$$\int_{S_b} \tau_l \cdot \vec{n} dS = \int_{S_b} \mu_l \left(\nabla \vec{U}_l + \left(\nabla \vec{U}_l \right)^T \right) \cdot \vec{n} dS \approx \mu_l \frac{U_T}{d} d^2 = \mu_l U_T d \tag{2.12}$$

Buoyancy force:

$$\left(\rho_l - \rho_g\right) V_b \bar{g} \approx \left(\rho_l - \rho_g\right) g d^3 \tag{2.13}$$

It should be noted that net surface tension force always vanishes:

$$\int_{S_b} \sigma k \vec{n} dS = 0 \tag{2.14}$$

However the local surface tension force does play an important role in making a bubble shape so as to attain the local force balance at each point of bubble surface [25]. As a matter of the fact that, the importance of the surface tension force can be easily understood if some dimensionless groups are deduced from the equation of bubble motion. The inertial, surface tension, viscous and buoyancy forces determine the terminal condition, and thereby only three independent dimensionless groups can be deduced from them;

Reynolds number is a measure of the relative importance of the inertial force compared to the viscous force and it is defined as

$$\mathrm{Re}_b = \frac{\rho_l U_b d_b}{\mu_l} = \frac{inertial \quad force}{viscous \quad force} \tag{2.15}$$

where U_b is the velocity of the bubble, d_b is the bubble diameter, ρ_l is the liquid density and μ_l is the dynamic viscosity of the surrounding fluid.

The Weber number is a measure of the relative importance of the dynamic pressure force compared to the surface tension force. It is given as

$$We = \frac{\rho_l U_T^2 d_b}{\sigma} = \frac{inertial \quad force}{surface \quad tension \quad force} \tag{2.16}$$

When dynamic pressure force is dominant, the appropriate parameter to be considered in a study of bubble deformation is the Weber number.

The Eötvös number is a measure of the importance of the buoyancy force compared to the surface tension force. It is defined as

$$Eö = \frac{g d_b^{\,2} \left(\rho_l - \rho_g\right)}{\sigma} = \frac{buoyancy \quad force}{surface \quad tension \quad force} \tag{2.17}$$

where g is the gravitational acceleration. When buoyancy force is dominant, the appropriate parameter to be considered in a study of bubble deformation is the Eötvös number. The Eötvös number is basically a measure of the bubble size, so that a functional relationship between a parameter and the Eötvös number describes how that parameter changes with the volume of the bubble.

Froude number gives the ratio of inertial forces to buoyancy forces and it is defined as

$$Fr = \frac{U_b}{\sqrt{gd_b\left(\rho_l - \rho_g\right)/\rho_l}} = \sqrt{\frac{inertial \quad force}{buoyancy \quad force}} \tag{2.18}$$

In summary, for a given Reynolds number, two dimensionless numbers of interest for determining the gas bubble shape deformation are Weber number and Eötvös number.

Another parameter that is commonly used and which exclusively characterizes the physical properties of the bubble-liquid system is the Morton number [25]. It is defined as

$$Mo = \frac{We^3}{Fr^2\,\mathrm{Re}^4} = \frac{g\mu_l^4\left(\rho_l - \rho_g\right)}{\rho_l^2\sigma^3} = \frac{\left(viscous \quad force\right)^4\left(buoyancy \quad force\right)}{\left(inertial \quad force\right)^2\left(s.\ \ tension \quad force\right)^3} \tag{2.19}$$

The Morton number contains only the physical properties of the fluid. Fluids are usually described in two groups, those with high Morton number ($Mo > 10^{-2}$) and those with low Morton number ($Mo < 10^{-6}$). Water at atmospheric pressure and 21 ^{o}C temperature has a Morton number of $1.1\text{x}10^{-11}$.

Thus deduction of appropriate dimensionless groups from the equation of bubble motion is possible if and only if contribution of surface tension force is taken into account [25].

A bubble rises through a denser liquid because of its buoyancy. The velocity U_T with which a single bubble rises through stagnant liquid is governed by the interaction between buoyancy and the other forces acting on the bubble as a result of its shape and motion. If the viscosity of the gas or vapor in the bubble is

negligible, the only three forces besides buoyancy, which are important, are liquid inertial, viscous, and surface tension forces.

2.3 Forces acting on the bubble

The fundamental physical laws, governing the motion of bubbles and heat transfer to bubbles in fluids are Newton's second law of motion, the principle of conservation of mass, and the first law of thermodynamics. Application of those laws to an infinitesimal control volume of material leads to the well-known Navier-Stokes, continuity, and energy equations. For a two phase system such as air bubble and water, these equations need to be solved for either phase. Interfacial relationships are then required to be able to solve the problem. In a moving gas bubble, there exists an internal velocity field or internal circulation, and the internal circulation velocity at different locations in the bubble can be different. Additional boundary conditions are required to complete the Navier-Stokes and continuity equations.

Exact analytical solutions to the continuity, momentum, and energy equations have been obtained only under restricted conditions. More usually, it is necessary to solve the equations numerically or to resort to approximate techniques where certain terms are omitted or modified in favour of those which are known to be more important. Boundary conditions must also be specified carefully to solve the equations. In many cases, especially for deformed bubbles moving in a liquid medium, one should rely on the experimental data.

An air bubble adopts a shape where surface tension force, hydrostatic forces and hydrodynamic force are in balance at every point of the bubble surface. The hydrodynamic force due to internal gas motion is usually negligible [22]. Main forces governing the bubble shape are surface tension, buoyancy, viscous and inertial forces. The viscous, buoyancy and inertial forces are trying to distort the shape, while the surface tension force is trying to keep the bubble shape intact. If the system pressure and the temperature are constant or their variations are negligible, those forces which change with the bubble diameter and bubble relative velocity are as follows:

Surface tension force, $F_{st} = \pi d_b \sigma$ (2.20)

Viscous force, $F_{vis} = \mu_l \pi d_b U_b$ (2.21)

where d_b is air bubble diameter, U_b air bubble velocity, μ_l is liquid viscosity and σ is air-liquid surface tension. If the surrounding liquid is not stagnant and there is a co-current upward liquid flow with the known velocity U_l, U_b should be changed with $U_{br}=U_b-U_l$, the relative velocity between the bubble and the liquid.

Consider a spherical air bubble with diameter d rising in a linear path through a stagnant liquid from rest. The forces acting on the bubble and governing the motion would be due to drag (F_D) and buoyancy (F_B).

For deformed bubbles, it is customary to define a volume equivalent bubble diameter, d_{ve}, corresponding to a spherical bubble of the same volume of the observed bubble.

A force balance can be written for a single bubble rising steadily in a stagnant liquid. The total force acting on a bubble rising in a liquid can be decomposed into separate and uncoupled contributions of gravity ($\vec{F}_G$), pressure gradient ($\vec{F}_P$), drag ($\vec{F}_D$), lift ($\vec{F}_L$), virtual or added mass force ($\vec{F}_{VM}$) [14]:

$$\vec{F}_{tot} = m_b \frac{d\vec{U}_b}{dt} = \vec{F}_G + \vec{F}_P + \vec{F}_D + \vec{F}_L + \vec{F}_{VM} \quad (2.22)$$

The force acting on a bubble due to gravity and pressure gradient, which is also called the buoyancy force, results in a net upward force. The equation for the gravity force is given by

$$\vec{F}_G = m_b \vec{g} = \rho_g V_b \vec{g} \quad (2.23)$$

The force acting on a bubble due to the pressure gradient in the liquid phase incorporate contributions from the Archimedes displacement force, inertial forces and viscous strain in the liquid:

$$\vec{F}_P = -V_b \Delta P = -\rho_l \vec{g} V_b \quad (2.24)$$

$$\vec{F}_B = \vec{F}_G + \vec{F}_P = \left(\rho_g - \rho_l\right)\vec{g}V_b \tag{2.25}$$

A bubble, moving in a column with a uniform flow field, experiences a drag force exerted by the liquid on the moving bubble. This drag force consists of a form drag and friction drag. The force is proportional to the relative velocity of bubble and acts in the opposite direction to the path of the bubble [14, 26-28].

It is customary to relate the measured drag to the projected area of the body A, the liquid density ρ_l, and the free stream or relative velocity U_{br} by the expression

$$\vec{F}_D = \pm\frac{1}{2}C_D\rho_l A\vec{U}_{br}^2 \tag{2.26}$$

where $A=\pi d^2/4$ for sphere and C_D is known as the drag coefficient. It is a dimensionless number that depends on the shape of the body and its orientation relative to the fluid stream and gives the ratio of the drag force to the inertial force.

A bubble, rising in a non-uniform liquid flow field, experiences a transverse lift force due to vorticity, rotations of bubbles or shear. The lift force consists of two components: The classical shear-induced lateral lift force and the wake induced lift force. Both forces act simultaneously on the bubble. For small, spherical bubbles the classical shear-induced lateral lift force dominates and for large, deformed bubbles the transverse lift force dominates [14]. In absence of a shear field the lift force is zero and because of the presence of only one bubble there is no hydrodynamic interaction between neighboring bubbles.

The virtual mass force, also called the added mass force, is especially important in case of unsteady rise when a bubble accelerates or decelerates. When the velocity of the bubble changes, the velocity of the liquid around the bubble changes accordingly. This can be seen as a resistance to acceleration, as the 'added mass' of the liquid also has to be accelerated along with the bubble [14]. The contribution of the virtual mass can be neglected, as the virtual mass is only important during the acceleration of the bubble (when a bubble starts to rise in the liquid) or in a turbulent field.

For a single air bubble rising steadily in water, the force balance may be reduced to;

$$\vec{F}_{tot} = \vec{F}_G + \vec{F}_P + \vec{F}_D = \vec{F}_B + \vec{F}_D \tag{2.27}$$

2.4 Two-phase flow regimes

2.4.1 Two-phase flow regimes in vertical circular channels

The typical two-phase flow patterns encountered in co-current upward flow through a large vertical circular channel include bubbly flow, slug flow, churn flow, and annular flow, depending upon gas void fractions or gas velocities. At very low void fractions, the flow is usually found to be in the bubbly flow regime, characterized by discrete bubbles dispersed in a continuous liquid phase. As the void fraction increases, small dispersed bubbles may collide and coalesce into gas slugs that span almost the entire cross section of the channel, resulting in a so-called slug flow pattern. At very large void fractions, the two-phase flow in the tube usually takes an annular flow pattern, characterized by most of the liquid flows along the wall of the tube whereas the gas flows in the central core of the channel. At intermediate void fractions, two possible flow patterns encountered in a vertical circular channels are churn flow, characterized by extremely chaotic and rather irregular gas-liquid interface, and wispy-annular flow, in which heavy "wisps" of entrained liquid flow in the gas core [1].

2.4.2 Two-phase flow regimes in vertical narrow rectangular channels

The two-phase flow patterns in narrow rectangular channels are not much different from those found in traditional channels having a large size gap except that the gas bubbles are two- dimensional in shape [29].

Relatively few investigations on two-phase flow patterns in narrow channels have been reported. Recently, the research has expanded to include also smaller gaps [12, 30-34]. Studies concerning flow regimes transition by Mishima *et al.* [17], Mishima *et al.* [30], Mishima and Nishihara [35], Sadatomi *et al.* [36], and Wilmarth and Ishii [12] concluded that similar flow patterns exist as in 3D gas-liquid columns. But these studies indicated that flow pattern transitions in narrow gap flows differ considerably from those obtained in 3D large channels [37].

Sample digitized images of vertical flow regimes in narrow rectangular channels can bee seen in Figure 2.2.

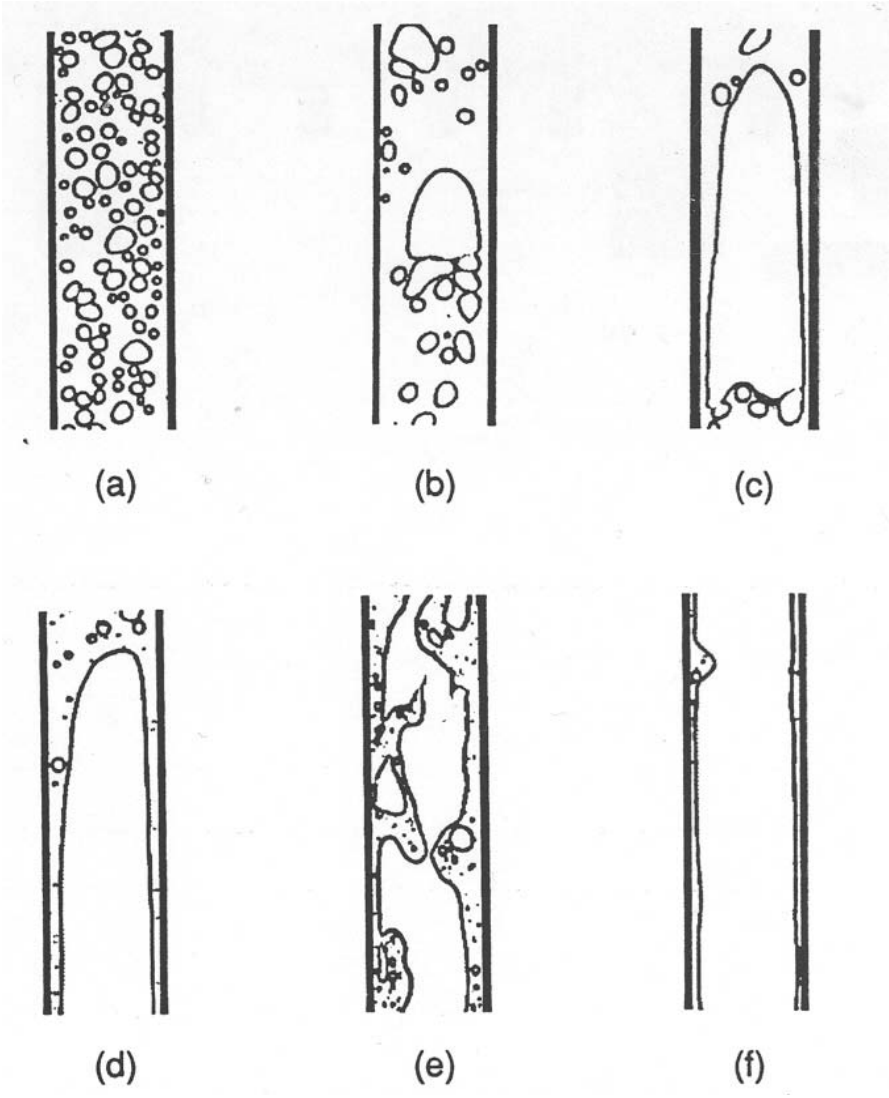

Figure 2.2 Sample digitized images of vertical flow regimes in narrow rectangular channels: (a) bubbly flow, (b) cap-bubbly flow, (c) slug flow, (d) slug-churn transition, (e) churn-turbulent flow and (f) annular flow [39]

Numerous theoretical and experimental investigations on the thermodynamics of two-phase flow in narrow channels have been performed [12, 29, 31-34, 38-41]. Some progress has been obtained concerning the flow pattern of two-phase flow in narrow channels, and some aspects of thermal-hydraulics of boiling in narrow

channels, such as pressure drop and average heat transfer coefficient. Many correlations have been obtained to model these physical phenomena. The behavior of flow regime transition of two-phase flow in narrow channels is much different from that in large channels [9]. So far, little information on flow regime transitions of two-phase flow in narrow channels can be found in the literature [9].

Flow regimes were observed in the vertical rectangular channels with the gaps of 1.0 and 0.6 mm by Xu [39]. Even though considerable differences exist in the definitions of two-phase flow patterns in medium size channels (a few mm to a few cm), general flow regimes consist of bubbly, slug, churn, and annular flow. Photograph observations of flow structures in the vertical rectangular channels with the gaps of 1.0 and 0.6 mm confirm such characteristics, except that the gas bubbles in thin rectangular channels are two-dimensional in shape [39].

The detailed two phase flow structures in vertical narrow channels can be summarized from the above literature as follows:

Typically, there are five different regimes of two-phase flow in a narrow channel under boiling conditions as follows [9]:

Bubbly flow: In bubbly flow, the liquid flows in the channels as the continuous phase, and the gas is distributed in liquid phase as discrete small bubbles [39]. In thin rectangular channels, the small bubbles are circular in shape, while in medium size circular channels, bubbles are spherical in shape.

Cap-bubbly flow: Bubbly flow is suppressed and the small isolated bubbles are combined with each other. Such an effect causes the coalescence of small bubbles forming the cap-bubbly flow [39]. Cap-bubbly flow can occur steadily in the channel at high liquid flow rate and at low gas flow rate [39]. The shape of the cap-bubbles is two-dimensional with nearly flat bottom and half circle at the top. Willmarth and Ishi [12] classified this type of flow as a cap-bubbly transition which is often characterized by coalescence of the bubbles into larger caps with a width up to 60% of the channel width.

Slug flow: Slug flow has larger two-dimensional “Taylor bubble” which contains a half circle cap head and a flat rectangular body [39]. The diameters of such Taylor

bubbles approach the channel width. The gas is separated from the side walls by slowly descending liquid films. The liquid flow is contained in liquid slugs which separate the successive gas bubbles and often carry small bubbles. The width of the gas slugs spanned more than 75% of the test section width [12]. Slug-Churn Transition-as the individual slug bubbles began to interact with one another, the preceding wake deformed the smooth interface of the following slugs [12].

Churn flow: Churn flow is formed by the breakdown of the large bubbles in slug flow as in circular channels. The gas flows in a more chaotic manner through the liquid which is mainly displaced to the channel wall. The flow has an oscillatory or time dependent character [39]. This type of flow is named as churn-turbulent flow by Willmarth and Ishii [12] because this type of flow is more chaotic and disordered.

Annular flow: This flow comprises a solid gaseous core, continuous in the axial direction, with a liquid film surrounding the core [12]. Large amplitude coherent waves are usually present on the surface of the film and the continuous breakup of these waves forms a source for small droplet entrainment which occurs in varying amounts in the central gas core [39].

2.5 Air bubble motion in infinite stagnant water medium

Before proceeding with air bubble behavior in a channel, air bubble motion in an infinite medium will be described. The dynamics of free rising single bubbles in stagnant liquids in infinite medium have been investigated by numerous authors. Most of the studies up to 1978 were summarized by Clift *et al.* [22].

Most of the theoretical studies discussed regarding the bubbles so far have been subjected to the assumption that the bubbles remain perfectly spherical. On the other hand, air bubbles deform when they are subjected to non-uniform or non-symmetric forces such as those due to motion and pressure that may overcome the stabilizing influence of surface tension [22].

2.5.1 Bubble shapes

At the interface between a gas bubble and surrounding liquid, a balance between the normal force, the shear force, buoyancy, and the surface tension force must be maintained for gas bubble stability. This balance governs the shape of the fluid particle.

If there is a relative motion of a gas bubble that exists in the surrounding liquid, the shape is naturally influenced by the forces in this surrounding liquid. Bubble has a shape so that the normal and shear forces are balanced at the interface between the bubble and surrounding liquid.

The surface tension force, when it has a constant value over the surface, acts to minimize the surface energy and therefore tends to keep a pure fluid particle spherical in shape [22]. Gas bubble will deform only when it is subject to non-uniform or non-symmetric forces such as those due to motion; pressure, or temperature variations that may overcome the stabilizing influence of surface tension. A small gas bubble tends to be spherical due to the large surface to volume ratio [22].

When the shape of the bubble is deformed significantly, theoretical approaches have limited success to predict the exact bubble shape. The predictions become less realistic with increasing bubble size and deformation because of increasing error in the assumed or calculated bubble surface dynamic pressure distribution.

One of the important studies performed on the determination of shape of the bubble is Grace's study [20, 42]. Clift *et. al*.[22] have discussed the various shape regimes and parameters for fluid particles (gas bubbles or liquid drops) rising or falling freely in infinite media. They classified bubbles using three dimensionless numbers, which are related to each other, i.e. the Reynolds number, the Eötvös number and the Morton number, in an experimentally determined diagram (See Figure 2.3). The Graces's diagram shows the effect of fluid properties and the bubble diameter on the shape and the terminal rise velocity of a single bubble [14]. The boundaries are somewhat arbitrary. Nevertheless, the diagram is a useful tool for demonstrating the wide range of bubble and drop behavior.

The Grace's diagram contains three main regimes in which the bubbles have different shapes: The spherical, ellipsoidal and spherical-cap regime. The boundaries between the spherical-cap regime and the other two regimes are relatively well defined. The spherical-cap regime consists of three sub-regimes: Spherical-cap, skirted and dimpled. The ellipsoidal regime consists of two sub-regimes: Wobbling and ellipsoidal.

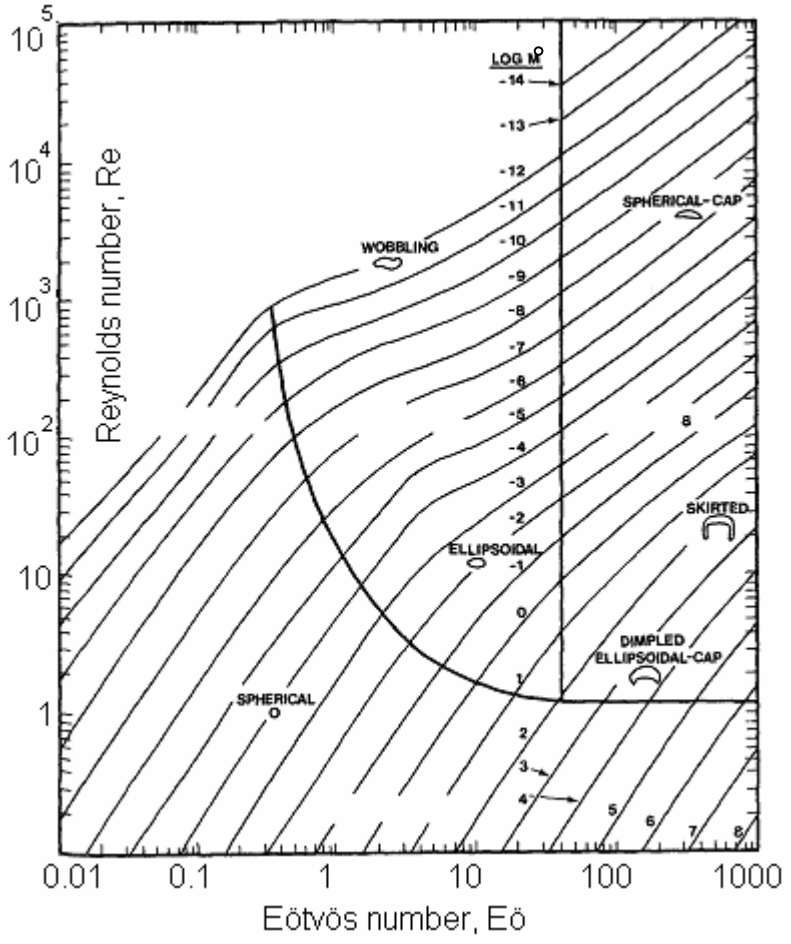

Figure 2.3 Shape regimes for gas bubbles and liquid drops in unhindered gravitational motion through liquids [22]

Several experimental studies [20, 24, 25] conducted for bubbles moving in stagnant water showed that bubbles having d_{ve}<0.8 mm (We≈0.62) have a spherical shape,

d_{ve} <2 mm (We≈3.3) have a ellipsoid shape (oblate spheroid), d_{ve} <4.2 mm (We≈5.3) have a ellipsoid shape with surface oscillations (unstable oblate spheroid) and bubbles having d_{ve} >4.2 mm have a distorted bubble shape (transition from oblate spheroid to spherical caps) where d_{ve} is volume equivalent air bubble diameter. Above a certain volume, bubbles rising in clean (contaminant free) water perform unsteady irregular motions.

Table 2.1 shows the results of the study of Tapucu [24, 25] for bubble motion in stagnant tap water. Aspect ratio (E) is defined as the minor axis of the ellipsoid (b) to the major axis of ellipsoid (a).

Table 2.1 Shape of air bubbles rising in stagnant water [27]

Volume equivalent bubble diameter (mm)	**Weber number**	***E* (*b/a*)**	**Shape of the bubble**
0-0.83	0-0.62	1	Spherical
0.83-2.00	0.62-3.7	1-0.5	Ellipsoidal
2.00-4.20	3.7-5.5	0.5-0.25	Ellipsoidal with surface oscillation
>4.20	>5.5	-	Distorted bubble with a spherical cap

Depending upon the relative magnitudes of the dominant forces acting on a bubble, such as surface tension and inertial forces, bubbles in motion are generally classified as spherical, oblate ellipsoidal and spherical-cap bubbles [43]. Bubbles in free rise in an infinite medium under the influence of buoyancy are generally classified under the following three groups [22]:

(a) Spherical: Generally speaking, bubbles are closely approximated by spheres if interfacial (surface) tension and/or viscous forces are much more important than dynamic pressure forces. Bubbles are usually termed "spherical" if the minor to major axis ratio lies within 10% of unity [22].

For $Re<1$, the fluid particle will remain essentially spherical independent of the magnitude of *Re*, level of contamination, and value of surface tension. With regard to the effect of the physical properties of the system, at $Re\leq1$, unless $Mo\geq1$, the particle remains nearly spherical [44].

Gas bubbles remain nearly spherical at moderate Reynolds numbers (e.g., at $Re=500$) if surface tension forces are sufficiently strong [22].

(b) Ellipsoidal: The boundary between the spherical and ellipsoidal regimes is less definite and its location may be dependent on the amount of surfactant present in the system. With low *Mo* systems such as air-water systems, an ellipsoidal particle undergoes random wobbling motions [44].

The term "ellipsoidal" is generally used to refer to bubbles which are oblate with a concave interface (viewed from inside) around the entire surface. It must be noted that actual shapes may differ considerably from true ellipsoids and that fore-and-aft symmetry must not be assumed. Moreover, ellipsoidal bubbles commonly undergo periodic dilations or random wobbling motions that make characterization of the shape particularly difficult [22].

In most systems, bubbles in the intermediate size range (typically between 1 mm < d_{ve} < 15 mm) lie in ellipsoidal regime [22]. Ellipsoidal fluid particles can often be approximated as oblate spheroids with vertical axes of symmetry, but this approximation is not always reliable. Bubbles in this regime often lack fore-and-aft symmetry and show shape oscillations [22].

Attempts to obtain theoretical solutions for deformed gas bubbles are very limited in the literature. A simplifying assumption that the bubble is perfectly ellipsoidal was mostly adopted in these solutions [22].

The aspect ratio, *b/a,* of the ellipsoidal bubble is denoted by *E*. It is an important parameter especially for the definition of the shape and the type of ellipsoidal bubbles (the axial dimension of the particle is *2b* while the maximum dimension normal to the axis of symmetry is *2a*).

At higher values of Reynolds and Eötvös numbers (large sized particle) the particle becomes an oblate spheroid of revolution (ellipsoidal regime) and eventually becomes a part of the spherical-cap regime [44].

(c) Spherical-cap: Large bubbles tend to adopt flat or indented bases and to lack any semblance of fore-and-aft symmetry. Such bubbles may look very similar to segments cut from spheres or from oblate spheroids of low eccentricity; in these cases the terms "spherical-cap" and "ellipsoidal-cap" are used. The leading edge of the cap is spherical and the trailing edge is flat. For $Eö > 40$ and $Re > 1.2$, the particle is in the spherical-cap regime [20, 44].

Effect of surface contaminants on the bubble shape: As it was explained Clift *et al.*'s book [22], traces of surface-active contaminants (surfactants) may have a profound effect on the behaviour of gas bubbles. Even though the amount of impurity may be so small that there is no measurable change in the bulk fluid properties, a surfactant can eliminate internal circulation, thereby significantly increasing the drag. Surface-active contaminants play a particularly important role in high σ systems (e.g., air/water) since surface tension reductions are largest for these systems [22].

2.6 Literature overview

An extensive literature survey has shown that there are adequate numbers of experimental studies investigating the air bubble motion in stagnant water conditions in infinite medium. Experimental studies conducted for stagnant water conditions are mostly related to the investigation of bubble velocities, bubble travel paths and wall effect on the bubble velocities. Literature overview will be explained in the order of bubble motion in infinite medium, in circular channels and in rectangular channels, followed by flow regime studies and computational studies.

Recently, Ellingsen and Risso measured the motion of a bubble with an equivalent diameter of 2 - 5 mm rising in water using two high speed video cameras. They observed that the bubble dynamics involves two modes. A primary mode develops

first, leading to a zigzag trajectory. A secondary mode then grows, causing the trajectory to progressively change into a circular helix [6].

Rippin and Davidson [45] investigated the rising velocity of a gas bubble in an inviscid liquid of negligible surface tension. The results were relevant to the behavior of a large gas bubble in a liquid like water, for which surface tension and viscous forces are small, the rising velocity being governed by a balance between buoyancy and inertial forces.

Tapucu [26] conducted an experimental study on bubbles having volume equivalent diameters 0.83 to 7.11 mm for the stagnant water conditions in tap water. He determined the air bubble rise velocity and drag coefficient, bubble path and shape change as a function of the investigated bubble diameter range. He also investigated the wall effect phenomenon and the effect of the water temperature on the bubble rise velocity. He performed his tests with a square crystal glass wall tank with dimensions of 17x17x100 cm to simulate infinite medium (i.e. bubble motion without wall effect).

The hydrodynamic interactions between gas bubbles in liquid and the effects on the main rise velocity for pairwise interacting bubbles were studied by Van Wijngaarden, Duineveldand, and Kok. They performed tests on single bubbles and bubble pairs in pure water and water contaminated with a well-defined amount of surfactants [23].

Zun and Groselj [16] investigated the air bubble rise velocity, the bubble mean lateral displacement and the mean frequency as functions of bubble diameter in the range of 0.4-6.5 mm for pure and contaminated water, in free rise and agitated-rise conditions. They performed their tests with a 16x16x145 cm glass column filled with water.

Lio and Zhao [46] expressed that theoretical investigations of rising Taylor bubbles in mini noncircular channels filled with a stagnant liquid were rather scarce. Thus, they reported a theoretical investigation of the drift velocity of an elongated bubble moving upwards in vertical mini equilateral triangular channels and square channels under the effect of buoyancy.

S. Polonsky, D. Barnea, and L. Shemer measured hydrodynamic parameters of the Taylor bubble, such as bubble shape, velocities of bubble nose and bottom, as well as bubble elongation due to hydrostatic pressure gradient. They found that the bottom of the Taylor bubble undergoes quasi- periodic oscillations. The frequency spectra of these oscillations are measured for different flow conditions. [47]

Das *et al.* carried out research work related to Taylor bubble in concentric annulus [48].

Collins derived two dimensional equations for the rising velocity of an elliptical-cap bubble, in which the circular-cap and parabolic-cap are taken as limiting cases [42]. These expressions were then compared with measured rising velocities obtained by injecting air bubbles into a "two-dimensional" column of water. Finally similar equations were derived in three dimensions, i.e. for the ovary ellipsoidal bubble, and the limiting cases of the spherical-cap and the paraboloidal-cap. A large isolated bubble in two dimensions has a circular-cap shape, but in contact with a surface it takes up an elliptical shape, and also its rising velocity increases.

A photographic study was realized related to two dimensional bubbles by Walters and Davidson [49]. This study deals with the upward motion of a two-dimensional bubble which starts from rest with a circular shape and then is free to rise under gravity forces. The subsequent distortions when such a bubble is suddenly formed in water were examined photographically, and the results compared with theory for a bubble in an inviscid liquid of zero surface tension.

Troniewski and Ulbrich studied 10 different rectangular channels. The aspect ratios covered the range from 12 to 0.1 for the vertical channels, and from 0.1 to 10 for the horizontal channels [39]. Air/water mixture was used as the working fluid in most of the tests.

Various transfer mechanisms exist between two-phase mixture and the wall, as well as between two phases, which depend on the flow regimes. This leads to the use of regime dependent correlations together with two-phase flow-regime criteria. From this point of view, many works on the flow regime have been undertaken in

channels. Recent studies on flow regime in narrow rectangular channels can be also summarized as follows:

Hibiki and Mishima [15] performed measurements of flow regime, void fraction, slug bubble velocity, and pressure loss for rectangular channels with the gaps of 1.0, 2.4, and 5.0 mm. They discussed the effect of the channel gap on the flow characteristics extensively.

Wilmarth and Ishii [12] extensively reviewed the studies, which were performed on two-phase flow in rectangular channels with gap width smaller than 7 mm. This review indicated that some work has been carried out in this area, however, quite inconsistent results and conclusions have been made by various researchers. Some confusion may stem from the variety of distinctions used in defining the flow regime transitions or the flow patterns themselves [12].

Wilmarth and Ishii [12] studied the adiabatic co-current and horizontal two-phase flow of air and water in the narrow rectangular channels with the gaps of 1 and 2 mm. They compared their data with predictions by models Mishima and Ishii, and concluded that a new distribution parameter was needed for the transition from bubbly to slug flow. Wilmarth and Ishii [12] also measured flow regime, void fraction and interfacial area concentration of adiabatic concurrent vertical and horizontal air–water flow in narrow rectangular channels with the gaps of 1 and 2 mm. They compared their flow regime maps with the existing ones as well as the models of flow regime transition criteria basically developed for a round pipe.

Xu [39] conducted experimental investigations for adiabatic air–water two-phase flow in vertical rectangular channels with the gaps of 0.3, 0.6 and 1.0 mm. They reported the observed flow regimes (bubbly, slug, churn, and annular flow) in channels with the gaps of 0.6 and 1.0 mm were similar to those found in the previous studies and that observed flow regimes (cap-bubbly, slug-droplet, churn and annular-droplet flow) in the channel with the gap of 0.3 mm were different from the previous studies.

Kureta *et al.* [41] used the neutron radiography technique to study the flow in narrow rectangular channels. They measured flow regimes, void fractions, bubble

velocity and two-phase pressure drop. They did not find churn flow with the gap of 1.0 mm.

Although some studies have been performed on the observation of flow regimes in a narrow rectangular channel, a few of them deals with the modeling of flow regime transition criteria for two-phase flow in a narrow rectangular channel. Recently, Xu *et al.* [29] proposed a preliminary model for flow regime transition criteria of two-phase flow in a rectangular channel and used the model for predicting flow regime transition boundaries of adiabatic air–water flow in narrow rectangular channels. However, it turned out that the model could not predict the flow regime transition boundaries in narrow rectangular channels satisfactorily and they concluded that a new model is needed to be developed.

Literature survey has shown that there are only a few experimental studies investigating the air bubble motion for co-current water flow conditions in that the direction of the moving bubble and the water flow are upwards [38, 50-55].

The first experimental study on the air bubble motion for co-current water flow conditions was performed by Baker and Chao [51]. They investigated the motion of individual air bubbles having diameters in the range of 0.38 to 7.0 mm in tap water flowing turbulently in a 10x10x120 cm conduit by photographic technique. They determined the bubble velocity and drag coefficient as function of the investigated range of the bubble diameter.

Another important experimental study for co-current water flow conditions was conducted by Yavuz [50]. He investigated the effect of co-current water flow on the bubble velocities, drag coefficients and paths for individual bubbles having diameters in the range of 0.97 to 2.72 mm in distilled water. He also investigated the effect of the water temperature on the bubble velocities. He performed his tests with a 65 cm long cylindrical plexiglas tube having inner radius of 4.75 cm. A photographic technique was used to determine the bubble's diameter and path.

Both experimental studies [50, 51] have indicated that the bubble average velocity for a certain range of bubble diameters is higher under co-current flow conditions than that under stagnant water condition and drag coefficient value for a certain

range of bubble diameters is lower under co-current flow conditions than that under stagnant water condition.

Recent computational studies on bubble motion can be summarized as follows:

Tomiyama *et al.* [3] made numerical analysis of bubble motion with the Volume-of-Fluid (VOF) method. Authors examined the applicability of the VOF method to the analyses of single rising bubble in an infinite stagnant liquid.

Image processing and analyzing techniques have been used in bubble motion investigation in recent years. Sadr-Kazemi and Cilliers [56] used an image processing algorithm for measurement of bubble size and shape distributions. Donevski *et al.* [57] developed an image processing technique for the study of bubble dynamics in subcooled flow boiling. Uchimura *et al.* [58] used image processing techniques to investigate two-phase interfaces.

Daripa [8] made a computational study of rising plane Taylor bubbles. The complicated nature of singularities associated with topological transition in the plane, Taylor bubble problem was briefly discussed in the context of estimating the speed of the fastest smooth Taylor bubble in the absence of surface tension by Daripa [59].

Kandlikar *et al.* [60] made high speed photographic observation of flow boiling of water in parallel mini channels.

Lioumbas, *et al.* [20] studied local velocities inside the gas phase during counter-current two-phase flow in a narrow vertical channel. The experimental data obtained were also compared with the results from a computational fluid dynamics (CFD) simulation with the intention to check the code's ability to predict the flow behavior in such geometry during countercurrent two-phase flow.

Bezdegumeli [28] made an experimental study to investigate air bubble motion in counter-current water flow conditions in a vertical pipe by using photographing technique. Bubble behavior was investigated at six different counter-current water flow velocities (6.5 cm/s, 7.9 cm/s, 10.5 cm/s, 12.9 cm/s, 15.4 cm/s, and 18.2 cm/s) in addition to stagnant water condition which is taken as the reference case. The

direction of the bubble motion is upwards and the direction of the water flow is downwards (i.e. counter-current).

According to the author's knowledge there is not any experimental study conducted for bubble motion in upward flowing water in a vertical narrow vertical channel in the open literature.

CHAPTER 3

EXPERIMENTAL FACILITY

3.1 Overview

An experimental facility was designed and constructed to make investigation on bubble motion in water through a vertical narrow rectangular channel with dimensions simulating a single cooling channel of TR-2 nuclear research reactor. Design of the experimental facility was mainly made with AutoCAD. The test section of the facility was modeled as one to one scale of the single cooling channel of TR-2 nuclear research reactor. The designed test section was manufactured from plexiglas of 1 cm thickness to obtain full optical access in the wide side and in the narrow side of the channel. The test section, therefore allows the visualization of the air bubble motion in stagnant water and in flowing water by using image processing techniques. Dimensions of the test section and coordinate system used in this study are shown in Figure 3.1.

A schematic diagram of the experimental facility is shown in Figure 3.2. This set-up allows good control of flow conditions in the test section. Two-phase (air-water) flow is developed in a 607 mm high (H) and 66.5 mm wide (W) rectangular channel (Figure 3.1). The gap (G) between the two parallel plates is 2.1 mm. Filtered de-mineralized water enters from the bottom and exits from the top. Air bubbles are introduced at a point, horizontally at the center of a plate and vertically 200 mm from the bottom. At this specified point, a bubble injector is located to generate air bubbles. The bubble injector is designed to be changeable at different inner diameters to produce different size of bubbles. Cross sectional view of the injector is shown in Figure 3.4. A set of bubble injectors which is made from brass with the inner diameter ranges from 1 mm to 3 mm was used in the tests.

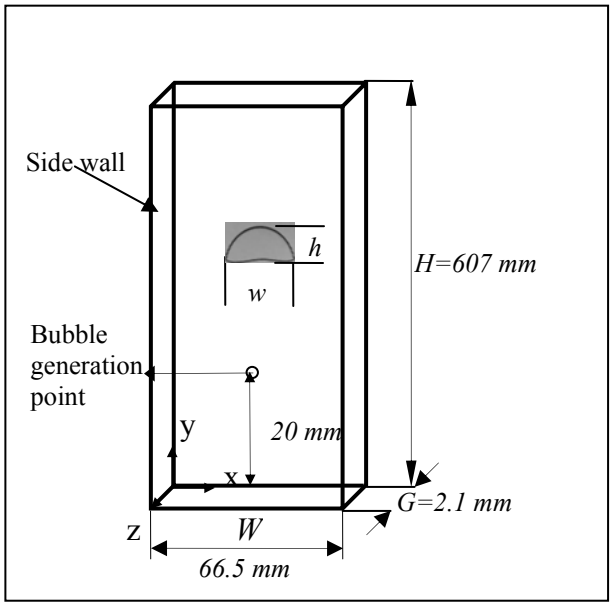

Figure 3.1 Coordinate system and dimensions of the test section

Distilled water collected in a storage Tank-1 is pumped to Tank-2 with constant flow rate by adjusting Valve-1 and the bypass Valve-2. Water level in Tank-2 is kept at fixed position by using bypass line and Valve-3 to maintain constant and steady water flow rate at the test section. To maintain a constant pressure head at the exit of the test section and to simulate the actual exit flow conditions in the reactor pool, an exit box of dimensions 400x400x400 mm, made of plexiglas, was connected to the test section. Water flow rate is measured by weighing the out-flowing water for a period of time. The weighing process is carried out by using an electronic balance. Water flow velocity is varied between 0-25 cm/s to resemble the natural circulation conditions of the TR-2 cooling channel.

Air is compressed and stored in air tanks. The stored air can be supplied to the system with a regulator valve that arranges the pressure in the air line by changing the flow rate. There are pressure gages and temperature gages to measure temperature and pressure of air, respectively. The volumetric flow rate in the air line is measured by rotameters. Air is supplied to the test section by the automatic bubble generation system. This system will be explained in the next section.

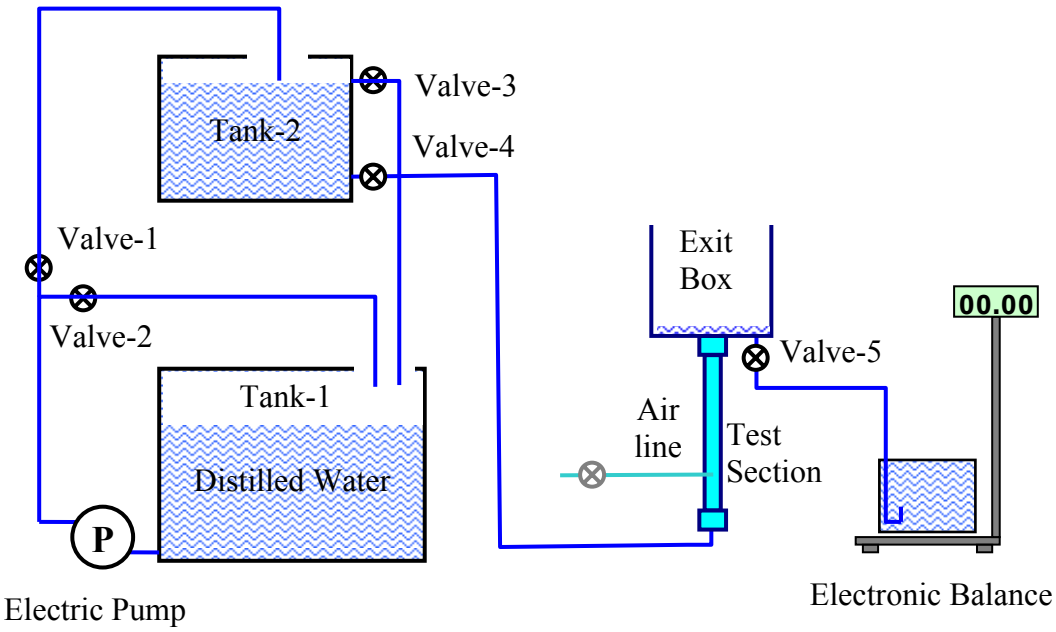

Figure 3.2 Water flow loop and weighing system

Figure 3.3 Photograph of the test section

3.2 Bubble generation system

An important aspect of the present study is to generate air bubbles of desired size and shape during tests. Thus, in the light of the studies about bubble dynamics, it is found that size and shape of the injected bubbles depend on air flow rate, bubble injector diameter, orifice constant, submergence, air bubble and water densities, water viscosity, surface tension, gravitational acceleration and drag force.

For the study of bubble motion it is desirable to eliminate as many sources of disturbance as possible. Possible sources of disturbance are volume and shape oscillations triggered at the production and release of the bubble. The bubble generation system used in the experimental setup was developed for accurate and reproducible bubble sizes.

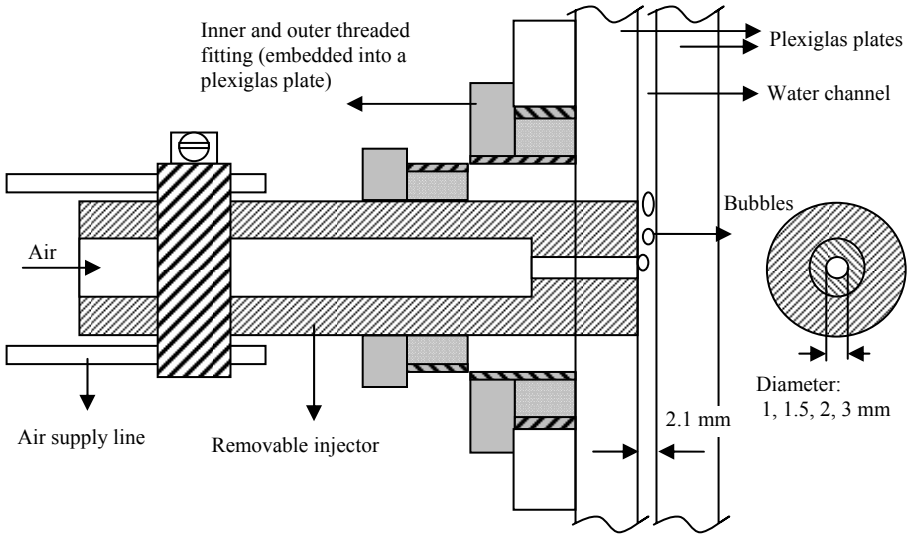

Figure 3.4 Bubble injector design

Bubble injector diameter plays an important role at low air flow rates, where surface tension provides the major restraining force. The volume of the bubbles in the tests were changed, mainly, by changing the injector diameter and/or air flow rate by using needle valve and pneumatic valve which is controlled by the computer.

For this purpose a computer controlled automatic bubble generation system was designed, constructed, and used in the experimental runs. This system is shown in Figure 3.5. In this system, a pneumatic solenoid valve and needle valve are used to control the bubble size. Control of the pneumatic valve is provided by a computer and related software. The valve is connected to the computer by a simple electronic circuit which was designed and manufactured by the author. This circuit is used to connect the valve to the computer, to start/stop the valve in a time span, and to supply the required power for the valve. Computer control of the valve is provided by GENIE software. By using this program, injection of bubble can be controlled by opening and closing time of the solenoid valve with an accuracy of 1/10 second. Bubbles with the same shape and same volume can be obtained by using this system and it satisfies the repeatability requirement of the tests.

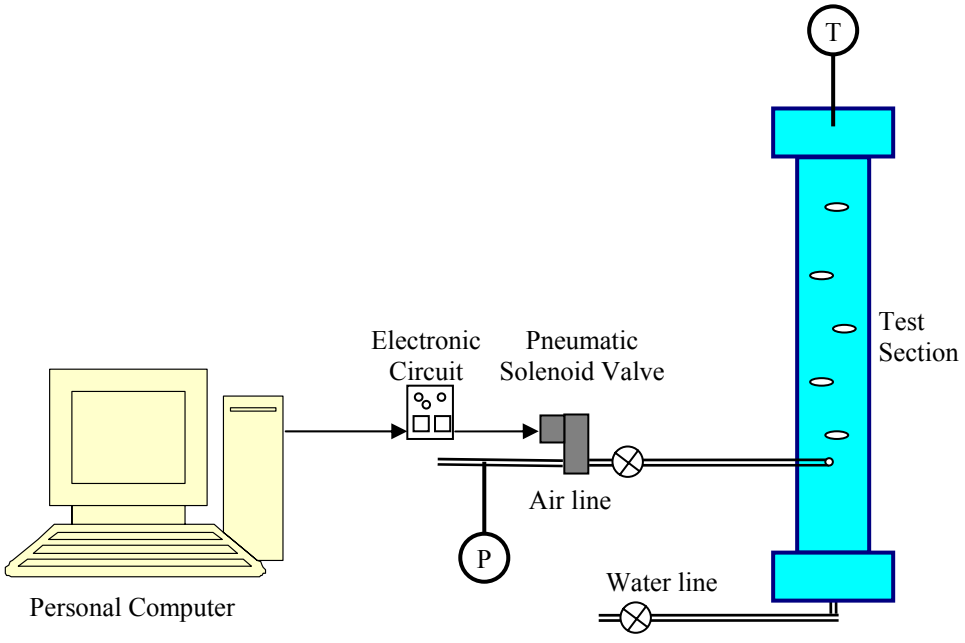

Figure 3.5 Schematic view of computer controlled automatic bubble generation system

3.3 Illumination system

The design of an image acquisition system is still more art than science. This requires that the designer properly consider the task requirements, isolate the object features of interest, and select source and sensor characteristics to emphasize and record these features [61].

The specification of the image acquisition system entails the proper design and/or selection of lighting sources, sensors, and supporting optics, and their positioning with respect to the objects being imaged. If it is done correctly, the result should be an image with maximum information utility. The goal of the imaging system is to acquire an image with high contrast between background (noise) information and any object features (signal) required to perform the task [61].

Only the images with sufficient contrast between the gas and the liquid can be analyzed. The images in the case, where the test section is illuminated from behind, have a light background with the bubbles appearing as dark objects in the field of view. It is important for the analysis that the edges of the bubbles are dark and distinct from the background. However, light areas in the centre of the bubble images will not affect the analysis. For image analysis, the illumination of the image background should be as uniform as possible.

When an object is placed between the light source and the camera to yield a silhouette or outline image of the object, this is called backlighting. The use of backlighting effectively produces a black and white (binary) image directly. This technique is ideal for applications in which silhouettes of objects are sufficient for recognition or other measurements. Backlighting using a diffuse source is practical when a high-contrast silhouette is required but edge definition is less critical than overall object shape. This provides a uniform background to silhouette an object and yields a high contrast image [61]. In the light of this information, an illumination system was planned and constructed.

Because of the fast shutter speed of the camera, enough light should be provided to capture the images with sufficient contrast. The illumination of the background should be as uniform as possible. On both sides of the test section, two halogen

bulbs of 500 W each are used, which illuminates the test section via indirect lighting on a white projector screen behind the test section.

The imaging system consist of a CCD digital camcorder positioned in front of the test section, two halogen lamps, a light diffuser and a dark room, as shown in Figure 3.6. The dark room was obtained by covering the environment of the test set-up with thick black curtains so that it was shielded from the ambient light. The light, reflected from diffuser situated about 30 cm behind the test section, produced well-dispersed and uniform background illumination.

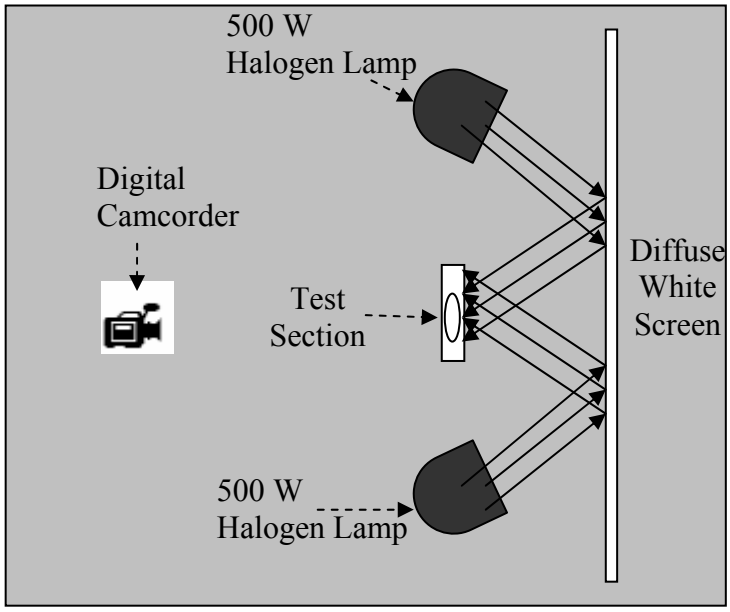

Figure 3.6 Illumination system

3.4 Image acquisition system

A Sony DCR-TRV461E Digital8 camcorder (Brief technical specifications are given in Table 3.1) was used for image acquisition purposes. Digital images of the front side of the test section are recorded with a digital camcorder at a rate of 25 frames per second. The camera resolution is 720H x 576V pixels. The video images are stored in the Digital8 video cassette during the tests. The images are processed

and analyzed off line with the software packages which will be explained in the next chapter.

The camcorder connection with the computer is achieved through the DV-OUT port supporting the IEEE 1394 protocol. The effective part of the 1/6″ CCD provides 350K actual pixels. Adobe Premiere 6.5 was used in order to transfer captured digital video records in DV-AVI format from the camcorder to the personal computer.

The distance between the camcorder and the test section was also adjusted to cover a certain field of view on the camcorder. The shutter speed is also adjustable with the minimum value of 1/4000 s. One of the limitations of the water flow velocity range of 0-25 cm/s in the tests is due to the camcorder shutter speed. Generally higher liquid flow velocity in the channel requires higher shutter speed and stronger brightness.

Table 3.1 Sony DCR TRV 461E Digital8 camcorder specifications

Technical Specifications	**SONY DCR TRV 460E**
Video Signal	PAL Color , CCIR Standard
Imaging Device	3.0mm (1/6″ Type) CCD Gross : 540000 pixels Effective Still and Movie : 350000 pixels approx
Filter Diameter	37mm Filter diameter
Optical Zoom	20x optical zoom (f/1.6 ~ 2.4) 35mm Conversion: 42-840mm
Color Temp / White Bal.	Auto/Manual or Auto
SteadyShot	Steady Shot (380k)
Input / Output Options	DV Input and Output (I-Link 1394)
Focus	Manual Focus
Video Format	Digital8

CHAPTER 4

IMAGE PROCESSING AND ANALYZING TECHNIQUES

Bubble information such as its position, perimeter, area, volume, velocity and motion path are obtained by image processing and image analyzing techniques. The procedure consists of detecting the edges of the bubbles, identifying them as individual objects and measuring and/or calculating their position, perimeter, area, volume, velocity and path. From the acquired images, a displacement field in pixel values is obtained and then velocity is obtained by calibrating the pixels to spatial values, knowing the time difference between consecutive frames. Various techniques involved in image processing were applied to obtain accurate measurement results in this study.

Before starting the tests, all measuring devices should be calibrated. Main parts of the measurement system of these tests are imaging, image processing and image analysis. To obtain these measurements accurately, "Camera Calibration" is required. The camera calibration procedures and implementation are explained in Appendix A and they are summarized below.

4.1 Camera calibration

Calibration is an important step in any computer graphics application that uses lenses/cameras [62]. Lenses project a real world scene onto a flat image. This projection is different for each lens and it depends on many intrinsic values for the lens. Calibration is the process of finding these intrinsic values. Once these values are found, one could figure out how the pixels in the image correspond to the points in the real world.

Once the distortion pattern of a lens is known, one can use any image taken with that lens, undistort it, and then has an image in which straight lines in the world will project to straight lines in the image [63]. As a result, more accurate measurements can be done with the calibrated images.

Radial distortion model of the camera/lens pair as a result of the camera calibration is plotted in Figure 4.1.

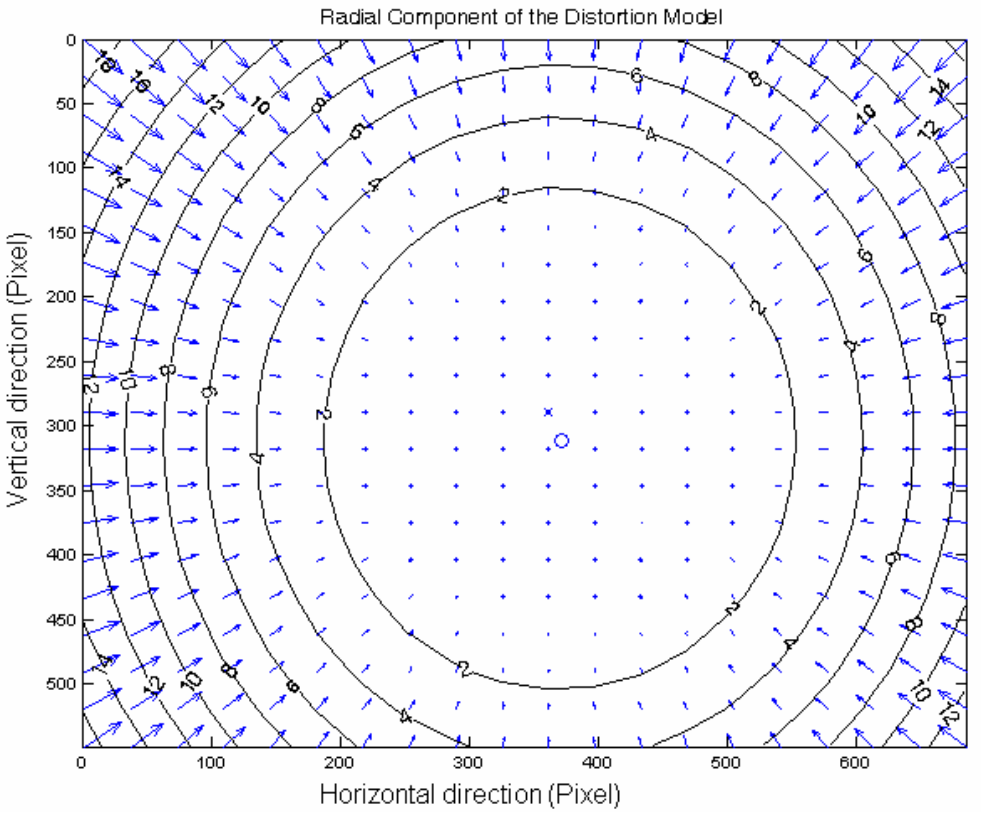

Figure 4.1 Radial distortion model

Figure 4.1 shows the impact of the radial distortion model on each pixel of the image. Each arrow represents the effective displacement of a pixel induced by the lens distortion. It can be seen from the figure that points at the corners of the image are displaced by as much as 25 pixels. This figure implies that if the measurements are taken from the central part of the video images, raw images can be used directly

for measurements. In this part, the displacement of a pixel induced by lens distortion is less than 5 pixels.

4.2 Image processing system

4.2.1 Image acquisition and preparation for analysis

Digital video records taken from the tests are transferred to the computer by Firewire-1394 interface. These interlaced PAL system digital video records are processed by Virtualdub freeware video processing software [64].

4.2.2 De-interlacing and doubling the frame rate of the video records

In PAL video records, an odd field is a frame containing only the odd lines. An even field is a frame containing only the even lines. If a single field is drawn on a screen, then the gaps between the lines are clearly visible. However, if a sequence of alternating odd and even fields is played back, the brain is not able to sense these gaps, and the playback appears to consist of whole frames.

De-interlacing is a process in which either the odd or the even lines are picked up by the software and are thrown away. It then simply duplicates the existing lines to fill the blanks. If the odd fields and even fields are duplicated respectively and combined sequentially it is possible to obtain 50 frames/s video records [64]. This process is shown in Figure 4.2.

First of all, video records are divided into odd and even fields and then, these fields are duplicated by using Virtualdub software (with de-interlace filter and field bob filter with smooth both fields option). These are separated to odd and even video records, then, saved as image sequences respectively. Obtained image sequences are combined one by one using a batch file sequentially. As a result, 50 frames/s video records are obtained.

4.3 Image analyzing system

Recognition of the bubbles in image sequences by computer is a very complicated process and it needs some image manipulation operations to increase the accuracy,

such as brightness/contrast adjustment, smoothing, sharpening, and some binary operations. After image enhancement process, edge detection, particle labeling and measurement techniques should be used to obtain required information in the image sequences. For this purpose ImageJ software is used as image analysis software. ImageJ is a public domain Java image processing program inspired by NIH Image [65].

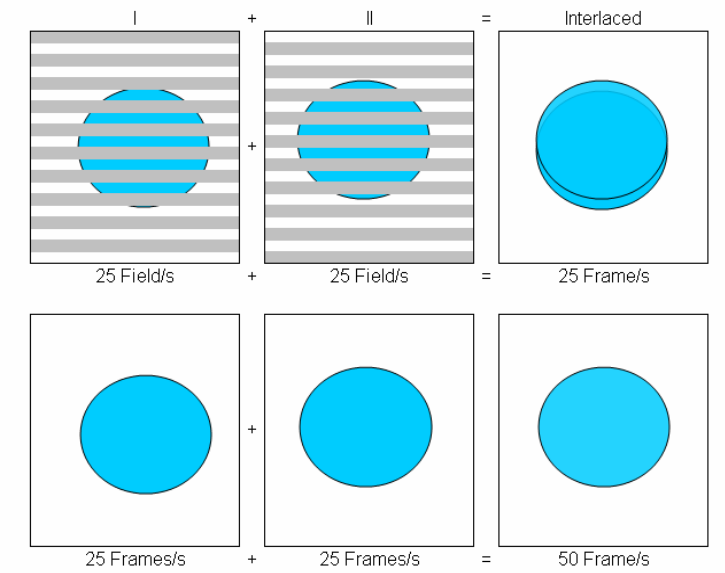

Figure 4.2 Duplication of frame rate in PAL systems

ImageJ can calculate the area and the pixel value statistics to measure the distances and angles. It supports standard image processing functions such as contrast manipulation, sharpening, smoothing, edge detection and median filtering etc. Spatial calibration is available to provide real world dimensional measurements in units such as millimeters.

ImageJ converts 16-bit and 32-bit images to 8-bits by linearly scaling from minimum to 0 and maximum to 255. With stacks, all the slices are scaled to 8-bits using the min and max of the currently displayed slice. RGB (Red-Green-Blue color system) images are converted to grayscale using the formula *gray=(red+green+blue)/3*.

"Brightness/Contrast" can be altered interactively. With 8-bit images, brightness and contrast are changed by updating the image's look-up table, so pixel values are unchanged.

Smooth filter blurs the active image or selection. This filter replaces each pixel with the average of its 3x3 neighborhood. Sharpen filter increases contrast and accentuates detail in the image or selection, but may also accentuate noise.

Subtract Background function removes smooth continuous backgrounds from bubbles and other images. It uses a rolling ball algorithm inspired by Stanley Sternberg's article [66].

Threshold operation converts grayscale images to black and white. The threshold level is determined by analyzing the histogram of the current selection, or of the entire image if there is no selection. The images are thresholded in order to distinguish between the bubbles and the illumination background. The threshold level is the grey level above which pixels in the image can be assumed to be in the background. It is very important to have always the same value for the threshold for the accuracy of the calculation of the bubble diameter.

Analyze Particles function counts and measures objects in binary or thresholded images. It works by scanning the image or selection until it finds the edge of an object. To find the edges, a Sobel edge detector is used to highlight sharp changes in intensity in the active image or selection [65]. It then outlines the object and measures it using the measurement algorithms.

4.4 Measured parameters in the tests by using ImageJ software

Area in 2D (A): Area of the bubble in cm^2

Center of Mass (X_m,Y_m): Center of mass coordinates of the bubble in cm

Perimeter (P): The length of the outside boundary of the bubble in cm

Upper corner of Bounding Rectangle (X_b,Y_b): Upper left corner of the smallest rectangle enclosing the bubble (cm x, cm y)

Bubble width (w): Bubble width in cm

Bubble height (*h*): Bubble height in cm

Fit Ellipse (*a,b*): The primary and secondary axis of the best fitting ellipse to the bubble

Circularity (*C*): A value of 1.0 indicates a perfect circle. As the value approaches 0.0, it indicates an increasingly elongated polygon.

Assuming that the bubble is a circle the area is given by:

$$d_{ae} = \sqrt{\frac{4A}{\pi}} \tag{4.1}$$

For perfect circle,

$$d_{pe} = \frac{P}{\pi} \tag{4.2}$$

where P is the perimeter of bubble and d_{pe} is the perimeter equivalent diameter.

If the bubble is a perfect circle then $d_{ae}=d_{pe}$ such that $d_{ae}/d_{pe}=1$. The ratio d_{ae}/d_{pe} is a measure of the sphericity (in 2D circularity) of the bubble and is computed as a shape factor.

Therefore using the Equations 4.1 and 4.2 the circularity is defined as:

$$Circularity = \left(\frac{d_{ae}}{d_{pe}}\right)^2 = \frac{4\pi A}{P^2} \tag{4.3}$$

Image processing steps are summarized in a flow chart (Figure 4.3). As an example, application of these steps to a single cap bubble is shown in Figure 4.4. Also, the fundamental steps of the image processing technique; original image sequences, background subtracted and masked image sequences, outlined image sequences and measured and graphed bubble paths are given in Figure 4.5. After obtaining these measurements from the experimental runs, rise velocities of bubbles can be calculated easily. Bubble motion in stagnant water is discussed in Chapter 5 and bubble motion in flowing water is discussed in Chapter 6 by using the data obtained from the image processing measurements.

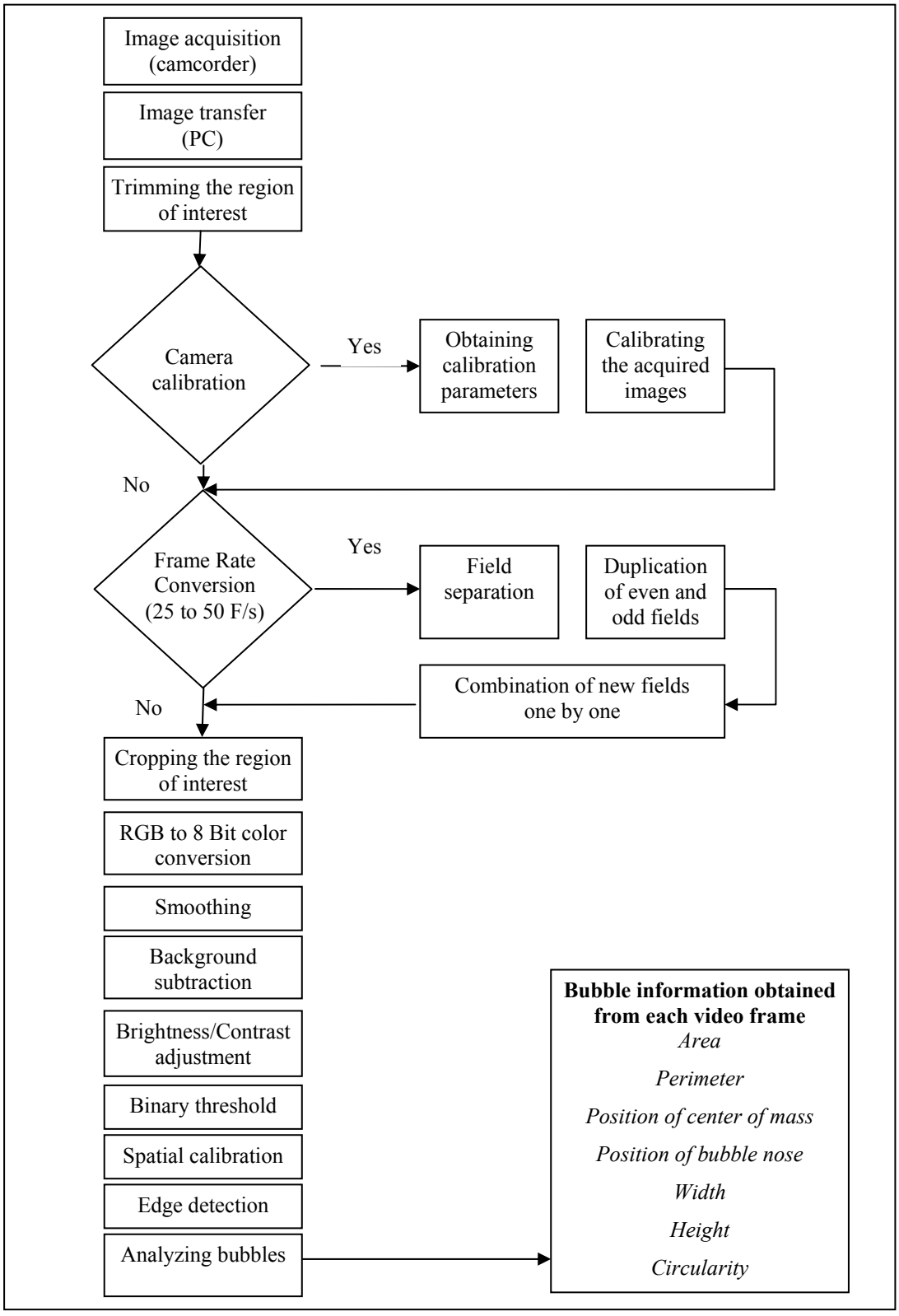

Figure 4.3 Flow chart of image processing steps

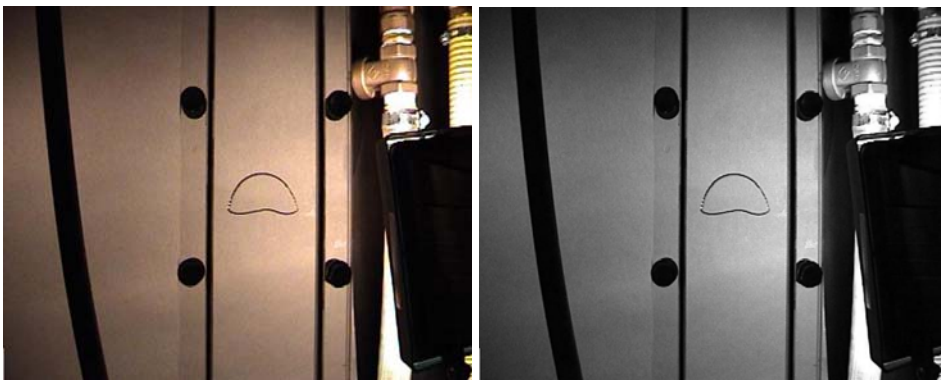

Raw image 8 Bit gray scale image

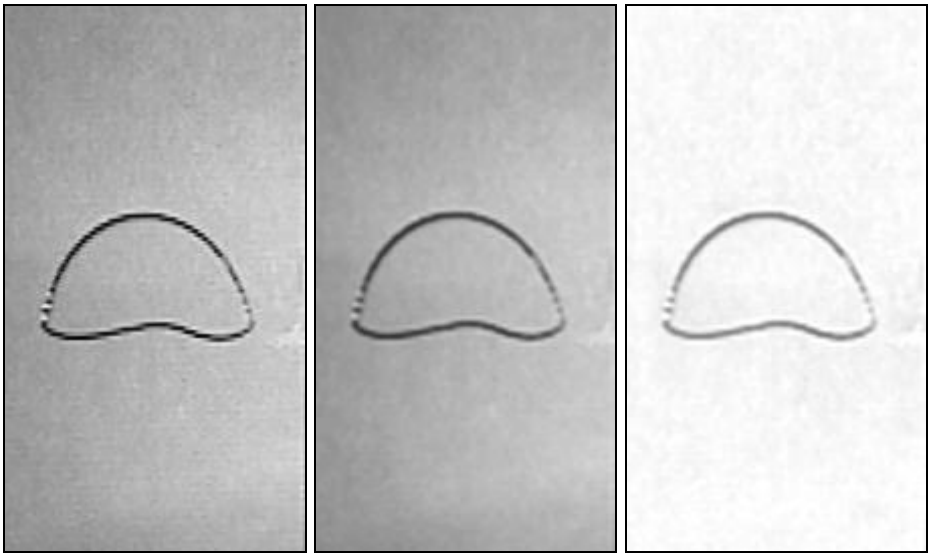

Cropped smoothed Background subtracted

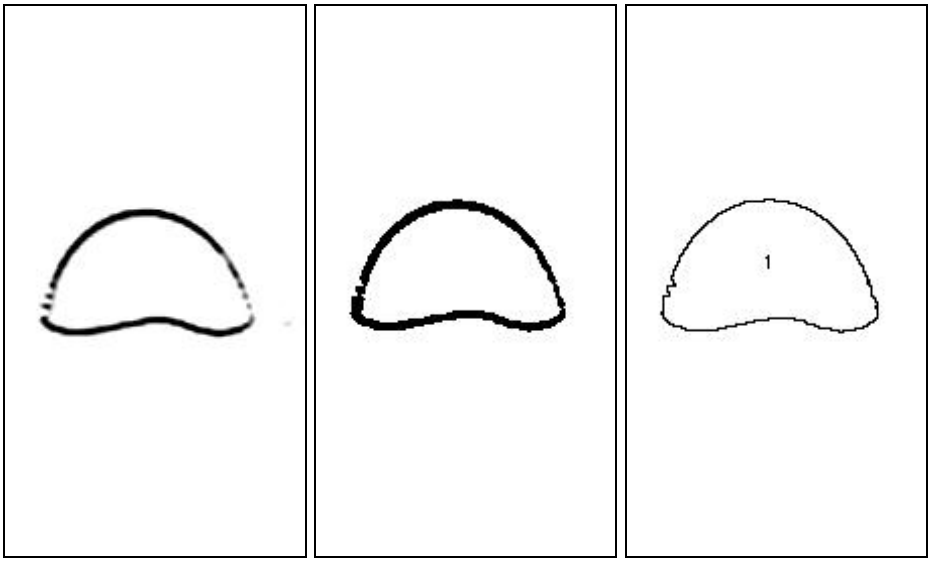

Brightness/Contrast adj. Binary threshold Edge detected and labeled

Figure 4.4 Fundamental image processing steps shown for a single bubble

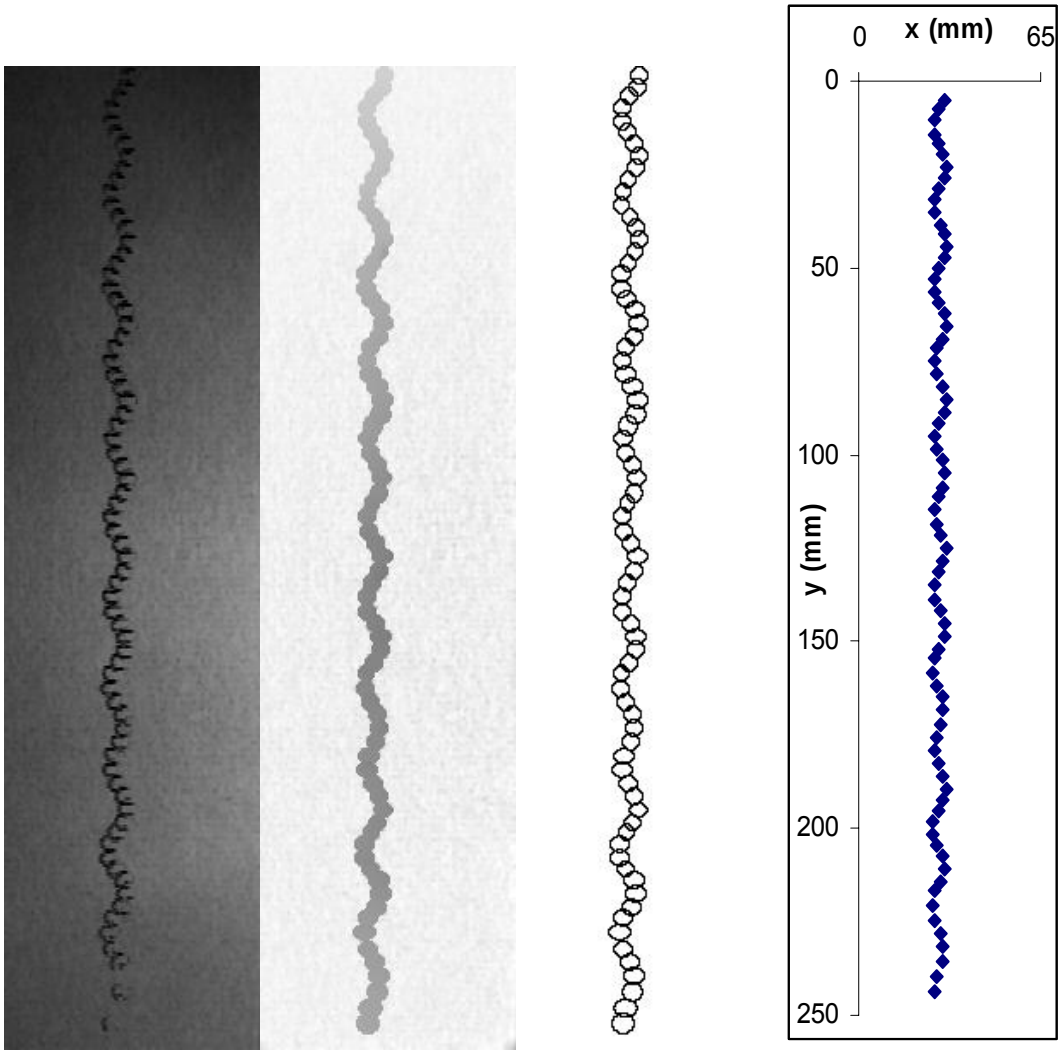

(a) (b) (c) (d)

Figure 4.5 Ellipse bubble path (a) original image sequences, (b) background subtracted and masked image sequences, (c) outlined image sequences, (d) measured and graphed bubble path

CHAPTER 5

RISING OF AIR BUBBLES IN STAGNANT WATER THROUGH A VERTICAL NARROW RECTANGULAR CHANNEL

5.1 Introduction

This chapter deals with the experimental study of bubble motion under stagnant water condition in a vertical narrow rectangular channel. The focus is on a single bubble behavior in pure water. The specific goals are to determine: bubble trajectory, bubble shape parameters, such as its perimeter, area, volume, circularity etc. and bubble rise velocity.

As explained in the previous chapter, the required parameters were obtained from the image analysis. In the mean time, to assess the bubble motion, additional information such as bubble velocities, related dimensionless numbers, bubble volume etc. is needed. Before starting the post-processing of the image analysis results, following variables were calculated;

- Vertical velocity component of air bubble measured from the center of mass, U_{bvc}
- Lateral velocity component of air bubble measured from the center of mass, U_{blc}
- Tangential velocity of air bubble measured from the center of mass, U_{btc}
- Vertical velocity component of air bubble measured from the nose, U_{bvn}
- Lateral velocity component of air bubble measured from the nose, U_{bln}
- Tangential velocity of air bubble measured from the nose, U_{btn}
- Bubble volume, V
- Volume equivalent bubble diameter, d_{ve}

- Area equivalent bubble diameter, d_{ae}
- Perimeter equivalent bubble diameter, d_{pe}
- Bubble Reynolds Number (based on U_{bvc} and d_{ve}), Re_{bve}
- Bubble Reynolds Number (based on U_{bvc} and d_{ae}) Re_{bae}
- Eötvös Number (based on d_{ve}), $Eö_{ve}$
- Eötvös Number (based on d_{ae}), $Eö_{ae}$
- Weber Number (based on d_{ve}), We_{ve}
- Weber Number (based on d_{ae}), We_{ae}
- Volume equivalent bubble diameter / Hydraulic diameter of the channel, λ_{ve}
- Area equivalent bubble diameter /Width of the channel, λ_{ae}

Vertical, lateral and tangential velocities of a bubble are calculated from the displacement of the bubble between two consecutive frames which is obtained from the image analysis. Vertical and lateral velocities are calculated to be able to assess their effects on the tangential bubble velocity.

Bubble velocity calculation is based on two different reference points. These are the bubble nose and the center of mass of bubble. Comparison of these two different calculations showed that the velocities obtained from the displacement of the center of mass of bubble are more accurate than from the displacement of bubble nose. In literature, most of the bubble velocity calculations are obtained from the displacement of bubble nose, because the center of mass of bubbles with random shapes are much more difficult to obtain when compared to the bubble nose. However, this information can be obtained easily by using the image processing and analyzing techniques. As it can be seen from Figure 5.10-f and Figure 5.11-f, center of mass velocities of bubbles are more stable than velocities of the bubble nose, because the bubbles undergo shape oscillations and the bubble nose is more affected from these oscillations than the center of mass of bubble.

5.2 Calculation of bubble volume

Volume of the bubble is calculated from the area of bubble, perimeter of the bubble and the channel gap size by the following procedure (Figure 5.1). As it can be seen

from the Figure 5.2, for profile of peripherals of ellipse and cap bubbles may be taken as half-circle and thickness of the bubble can be assumed as same as the channel gap size. Same assumptions are also valid for circular bubbles. Volume of the bubble can be calculated from the following formula;

$$V = AG - P\left(\frac{G^2}{2} - \frac{\pi G^2}{8}\right) \tag{5.1}$$

where V bubble volume, A bubble area, P bubble perimeter and G channel gap size.

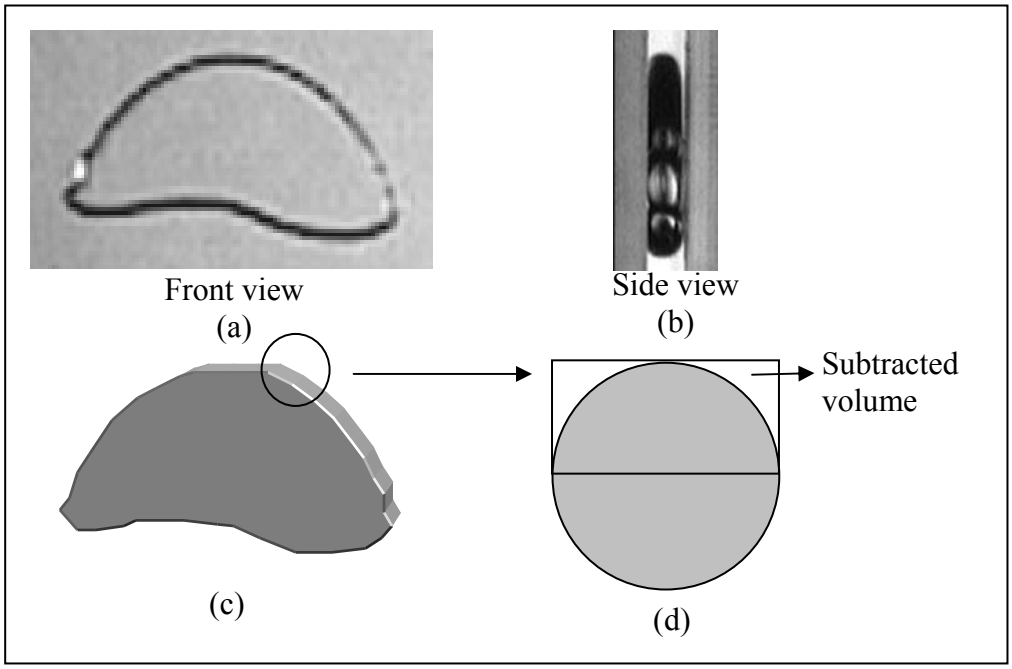

Figure 5.1 Calculation of bubble volume from the bubble area (a-front view, b-side view, c-first estimation (bubble area x channel gap), d-subtracted volume from the first estimation (Perimeter of bubble x subtracted volume)

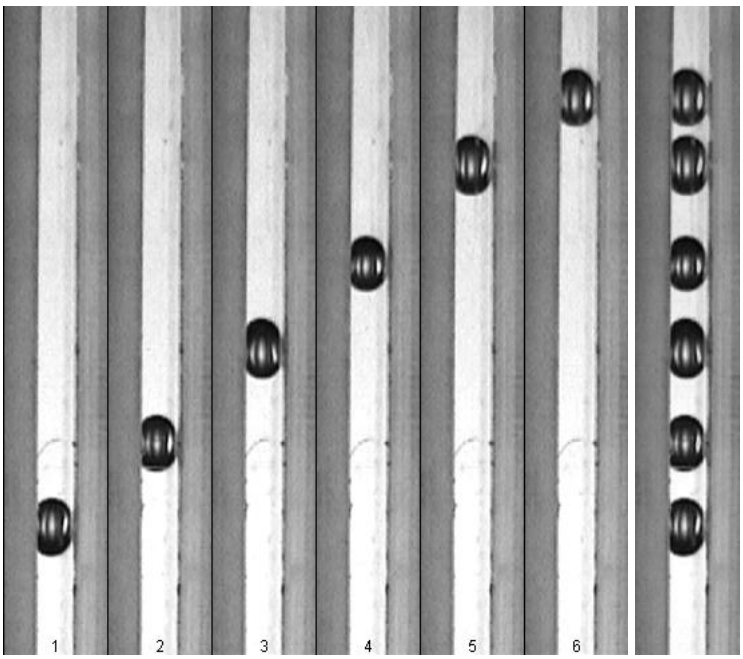

(a)

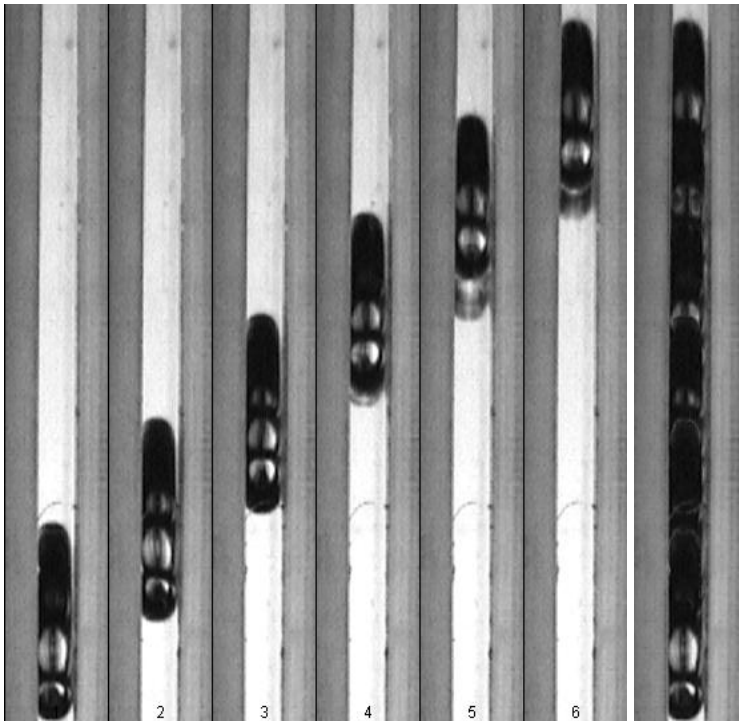

(b)

Figure 5.2 Narrow side view of ellipse (a) and cap (b) bubbles rising in stagnant water

5.3 Characteristic dimensions

Before starting the discussions of results, the parameters that will be used in the calculations and correlations should be determined. A suitable characteristic length of the channel (hydraulic diameter of the channel, channel width or perimeter equivalent channel width) and a characteristic length of the bubble (perimeter equivalent bubble diameter, area equivalent bubble diameter, volume equivalent bubble diameter, or bubble width) should be defined.

Tsuchiya and Fan [43] used the bubble width as a characteristic length based on the following discussion. The wake size is not controlled by the equivalent circular bubble diameter but by the distance between the separation points at both sides of the bubble. At higher Reynolds numbers, bubbles are of oblate shape such as elliptical and circular-cap. The separation points are rather fixed at both edges- the portions of the bubble surface with the sharpest curvature. Thus, the characteristic length governing the wake phenomena should be the actual distance from edge to edge, i.e. the bubble width [43]. In the light of above explanations, Tsuchiya and Fan [43] decided to use bubble width as a characteristic bubble dimension instead of area or volume equivalent bubble diameter.

In order to compare the two-dimensional data obtained in Tsuchiya and Fan's [43] work with the existing three dimensional results from the literature, the bubble width was related to the area equivalent bubble diameter, which was conventionally used as a characteristic length in the literature. Tsuchiya and Fan [43] suggested the following relation for bubble width.

$$w = 1.72 d_{ae}^{\,1.23} \quad 3.5 < d_{ae} < 20 \text{ mm} \tag{5.2}$$

Figure 5.3 compares Eq. 5.2 with experimental data of the present work. The geometry of Tsuchiya and Fan's [43] test section is a narrow rectangular channel with 5 mm gap size. Because of the larger gap size in the channel, 3D effects are more governing when compared with the results of present study. The reason of the shift of the curves to the right in Figure 5.3 may be due to differences in the channel dimensions.

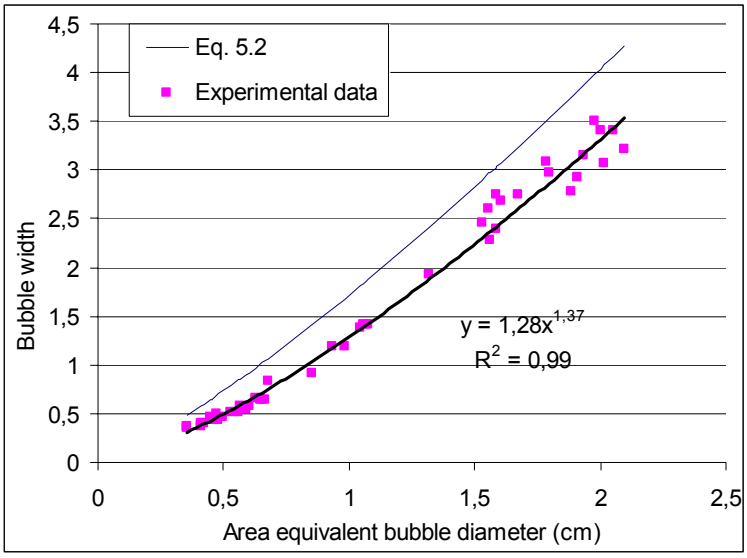

Figure 5.3 Bubble width versus area equivalent bubble diameter

In this dissertation, area equivalent bubble diameter is preferred to be used as the bubble characteristic dimension, because it represents the bubble behavior more precisely. For comparison with the literature, Figure 5.4 and curve fitting equations are given.

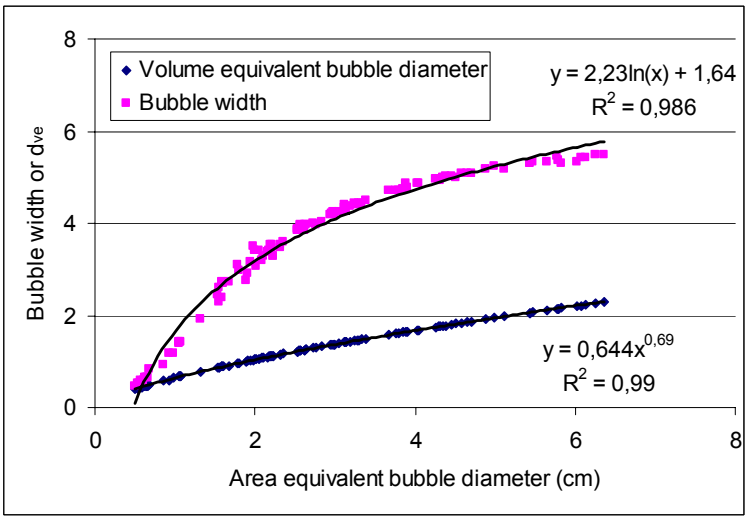

Figure 5.4 Area equivalent bubble diameter versus volume equivalent bubble diameter and bubble width in the tests

5.4 Reliability and repeatability of tests

To check the bubble generation system and the results of image analysis process, a set of tests were realized. Purpose of these tests was to show the repeatability and reliability of the experimental results. In this set of tests, eight different bubbles with the same size were generated with a time delay between each generation to eliminate the effect of bubbles to one another. The recorded video images were processed and analyzed with the techniques explained in the previous chapter.

These analyzed bubbles are shown in Figure 5.5 as combined sequences of images in series. Paths of the bubbles are almost identical. As it can be seen from the images, it is possible to generate bubbles of the same shape and size. If the results of eight different tests are compared with each other, it is seen that the results of tests are satisfactory from the repeatability of experimental runs and reliability of image processing measurement points of view (See the results in Figure 5.6).

Uncertainties in experimental measurements and calculations are summarized below and given in detail in Appendix B.

Uncertainty in area equivalent bubble diameter measurements and bubble volume calculations for 0.3 cm < d_{ae} < 7 cm, are 0.4% < δ_d/d_{ae} < 9.7% and 1% < $\delta V/V$ < 20.8%, respectively. The reason for 20.8% error in bubble volume calculations is due to the 3D effect for very small bubbles such as 0.3 cm.

Maximum error might occur in bubble velocity (U_b) calculations due to the uncertainty in the distance traveled by the bubble between two consecutive frames for 15 cm/s < U_b < 24 cm/s is 3.34 < $\delta U_b/U_b$ < 5.34%. Uncertainty of mean water velocity measurements is maximum 6%.

Uncertainties in Reynolds and Weber number calculations for 0.3 cm < d_{ae} < 7 cm, and 15 cm/s < U_b < 24 cm/s are 3.34% < δ_{Re}/Re< 11% and 0.04% < δ_{We}/We< 3.2%, respectively. Uncertainties in Eötvös number calculations for 0.3 cm < d_{ae} < 7 cm is 0.83% < $\delta_{Eö}/Eö$< 19.34%. The reason for 19.34% error in Eötvös number calculations is due to the Uncertainty in area equivalent bubble diameter measurements for very small bubbles.

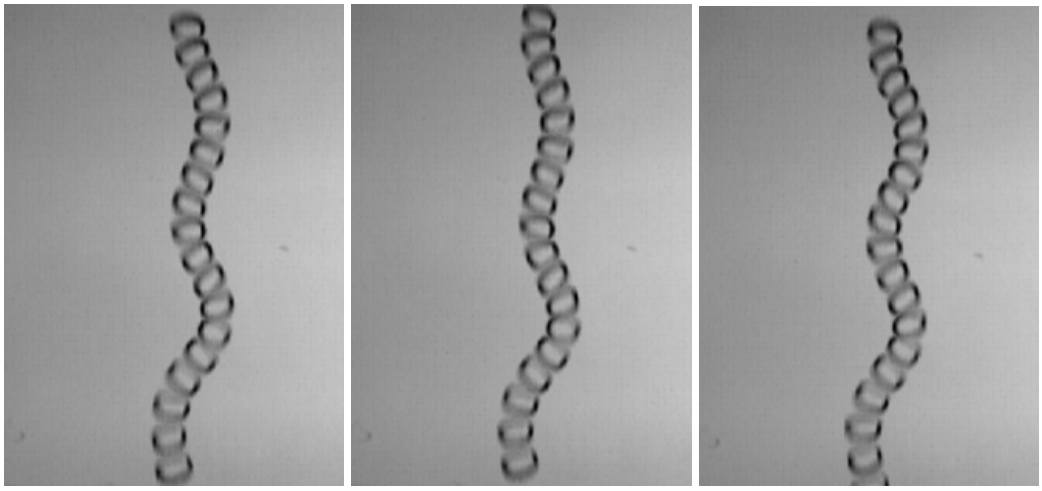

(a) (b) (c)

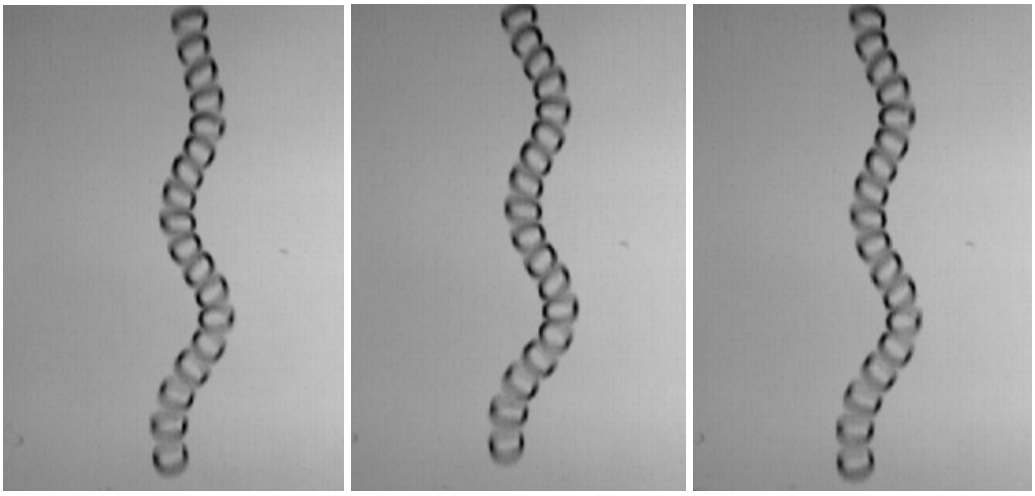

(d) (e) (f)

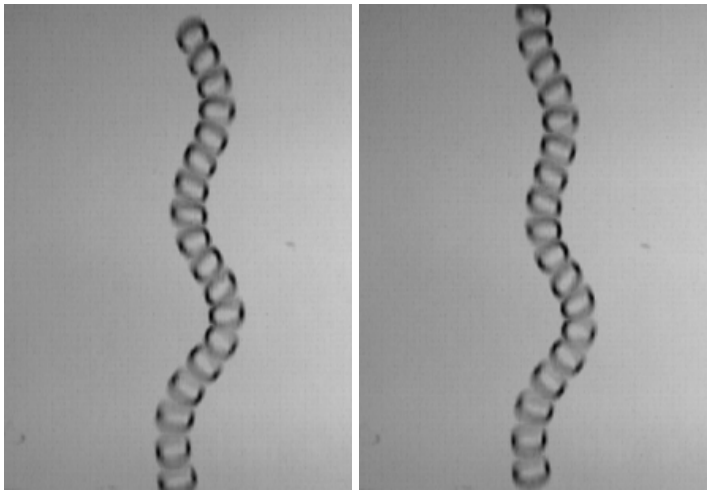

(g) (h)

Figure 5.5 Paths of eight different bubbles with same size under similar conditions

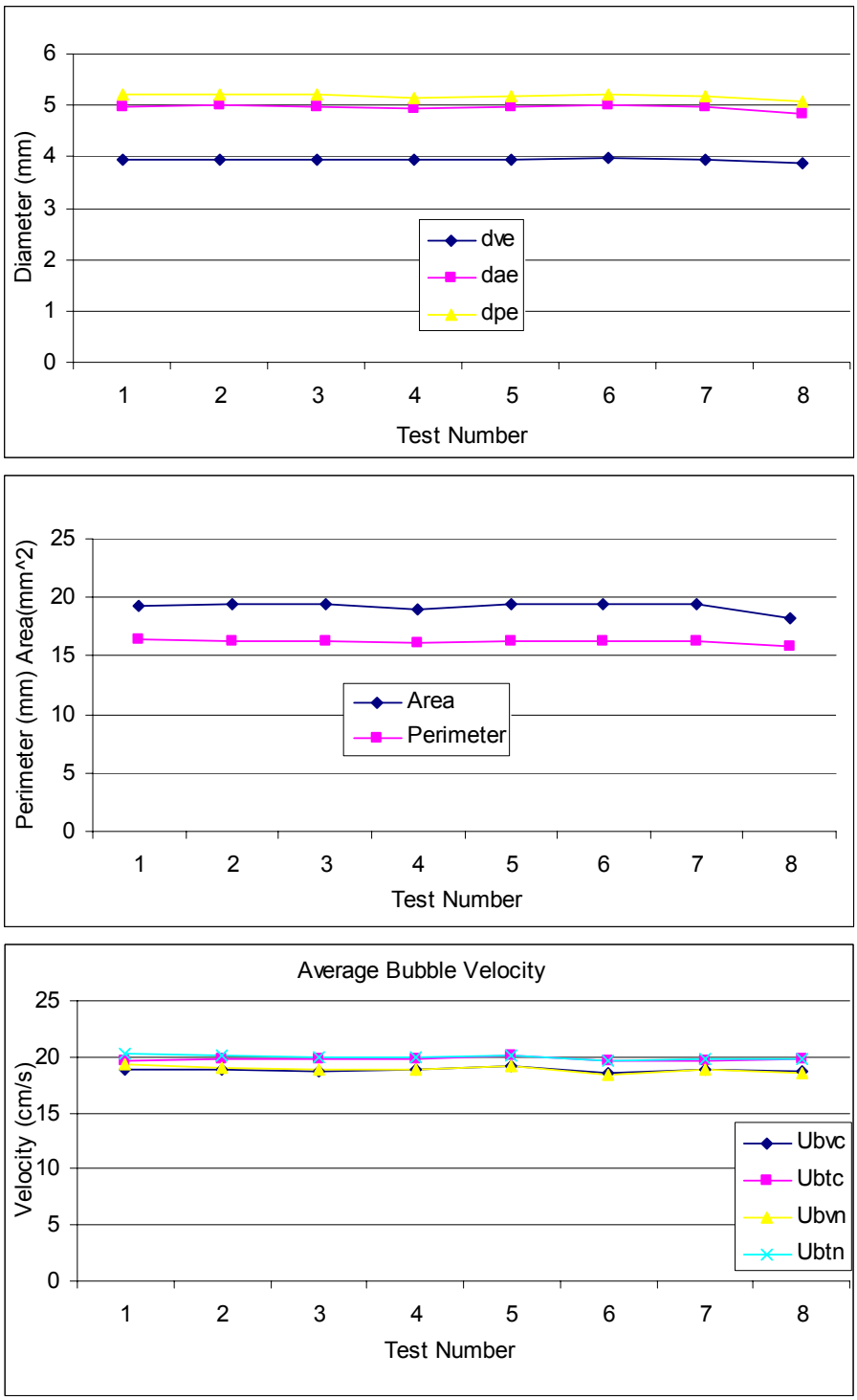

Figure 5.6 The results of eight different tests with same bubble size under similar conditions

5.4.1 Bubble shapes and trajectories

The behavior of a single gas bubble rising in a vertical narrow rectangular channel depends on the size of the bubble. When the bubble is small it has circular shape in 2D and rises along a vertical rectilinear path (See Table 5.1 for bubble shapes). Larger bubbles become ellipse and tend to rise along sinusoidal paths. Increase in bubble size transforms its shape into irregular deformed ellipse which is named as wobbling ellipse and it moves in a sinusoidal path. Further increase in the bubble size causes the bubble to be of a cap shape and again to rise along a rectilinear path. With still further increase in size, the bubble is constrained by the channel walls and the bubble shape changes into a bullet shaped cap type.

Description of the shape and motion of the air bubble in stagnant water as a function of bubble size and Reynolds number based on d_{ve} in an infinite medium (3D case) are given in Table 5.1 [67].

Table 5.1 Shape and motion of air bubbles as a function of d_{ve} and $Re(d_{ve})$ in stagnant water in infinite medium [67]

Diameter Range	***Re*** **(d_{ve})Range**	**Behavior**
$d_{ve} < 0.8$ mm	$Re < 70$	Spherical bubbles traveling in rectilinear paths
$0.8 < d_{ve} < 1.24$ mm	$70 < Re < 400$	Spherical bubbles traveling in rectilinear paths
$1.24 < d_{ve} < 1.54$ mm	$400 < Re < 500$	Oblate spheroid rectilinear motion
$1.54 < d_{ve} < 4.8$ mm	$500 < Re < 1100$	Oblate spheroid helical motion
$4.8 < d_{ve} < 7$ mm	$1100 < Re < 1600$	Irregular oblate spheroid, almost rectilinear motion
$7 < d_{ve} < 17.6$ mm	$1600 < Re < 5000$	Transition from oblate spheroid to spherical caps, almost rectilinear motion
$d_{ve} > 17.6$ mm	$Re > 5000$	Spherical caps, rectilinear motion

Gerardes de Viras [23] summarized the path and transition criteria of rising air bubbles in stagnant water infinite medium (3D case) from previous studies in a table. This summary is given below in Table 5.2 [23].

Table 5.2 Summary of previous results for the onset of path instability and the regimes of the observations [23]

	Summary of observed path and transition criteria		
	straight	spiral	zigzag
Haberman& Morton (1954)	$Re(d_{ve}) < 300$	$300 < Re(d_{ve}) < 3000$	$Re(d_{ve}) > 3000$
Hartunian& Sears (1957)	$We(d_{ve}) < 3.17$	$We(d_{ve}) > 3.17$	$We(d_{ve}) > 3.17$
Saffman (1956)	$d_{ve} < 1.4$ mm	$d_{ve} > 1.0$ mm	$d_{ve} > 1.4$
	$Re(d_{ve}) < 400$	-	$Re(d_{ve}) > 400$
Aybers& Tapucu (1969)	$d_{ve} < 1.34$ mm	$1.34 < d_{ve} < 2.0$ mm	$d_{ve} = 2.00$ mm
	$Re(d_{ve}) < 565$	$565 < Re(d_{ve}) < 880$	$880 < Re(d_{ve}) < 1350$
Duineveld (1994,1995)	$d_{ve} < 1.82$	-	$d_{ve} > 1.82$
	$We(d_{ve}) < 3.3$	-	$We(d_{ve}) > 3.3$
	$Re(d_{ve}) < 662$	-	$Re(d_{ve}) > 662$

A set of tests were prepared and realized to obtain bubble shapes, paths and rise velocities at 21^{o}C stagnant water conditions in the test section. In this set of tests, bubbles with area equivalent bubble diameters between 2 mm and 70 mm were generated and tracked along the channel and recorded by the camcorder. In this range (2 mm $< d_{ae} <$ 70 mm, or 2 mm $< d_{ve} <$ 23.6 mm) more than five hundred bubbles were recorded, analyzed and measured in stagnant water condition.

Bubble types, area and volume equivalent bubble diameter ranges, Reynolds, Eötvös and Weber Numbers with respect to area and volume equivalent bubble diameters, and bubble paths are given in Table 5.3. Dimensionless numbers with respect to the area and volume equivalent bubble diameters are given to be able to compare with the existing literature and to see two dimensional (2D) effects when compared with the three dimensional (3D) case.

Shape and measured rise velocity (U_{bvc}) of bubbles with an area equivalent diameter of 3 mm to 66.6 mm are plotted in Figure 5.8.

There was a temperature rise of almost 1°C from the beginning of the tests to the end because of illumination with two halogen lamps, 500 W each. To check the significance of the temperature rise effect on the bubble motion, the set of tests were repeated for 27°C water. Bubble rise velocities of these two sets of tests are shown in Figure 5.7. 6°C temperature rise of water temperature decreases the bubble rise velocities almost 5%. Thus, it can be concluded that 1 °C temperature increase during the tests seems to be insignificant.

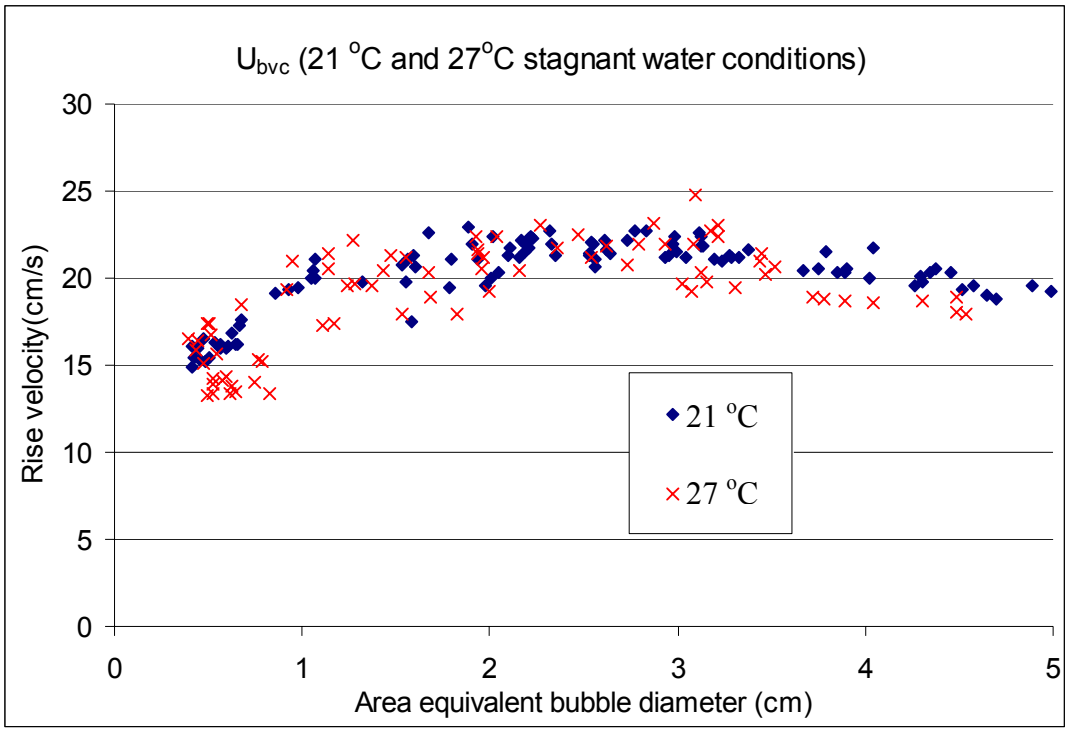

Figure 5.7 Rise velocities in stagnant water at 21°C and 27°C

Table 5.3 Air bubble shapes and related dimensionless number ranges in a vertical narrow rectangular channel under stagnant water condition at 21°C.

Bubble Shape	**Image**	***Re***		***Eö***		***We***		***Diameter***		d_{ae}/W	**Path**
		d_{ae}	d_{ve}	d_{ae}	d_{ve}	d_{ae}	d_{ve}	d_{ae} (mm)	d_{ve}(mm)		
Circle		$Re < 579$	$Re < 527$	$Eö < 1.02$	$Eö < 0.85$	$We < 1.70$	$We < 1.55$	$d_{ae} < 2.7$	$d_{ve} < 2.6$	<0.04	Rectilinear
Ellipse		$579 < Re < 1624$	$527 < Re < 1103$	$1.02 < Eö < 9.88$	$0.85 < Eö < 4.55$	$1.70 < We < 4.30$	$1.55 < We < 2.92$	$2.7 < d_{ae} < 8.5$	$2.6 < d_{ve} < 5.8$	$0.04 < d_{ae}/W < 0.13$	Sine-curve
Ellipse-wobbling		$1624 < Re < 3170$	$1103 < Re < 1798$	$9.88 < Eö < 31.70$	$4.55 < Eö < 10.19$	$4.30 < We < 9.16$	$2.92 < We < 5.19$	$8.5 < d_{ae} < 15.3$	$5.8 < d_{ve} < 8.7$	$0.13 < d_{ae}/W < 0.24$	Sine-curve
Hat-wobbling		$3170 < Re < 4454$	$1798 < Re < 2290$	$31.70 < Eö < 59.51$	$10.19 < Eö < 15.73$	$9.16 < We < 13.19$	$5.19 < We < 6.78$	$15.3 < d_{ae} < 20.9$	$8.7 < d_{ve} < 10.8$	$0.24 < d_{ae}/W < 0.32$	Sine-curve or Rectilinear
Hat-Cap	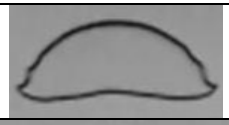	$4454 < Re < 6223$	$2290 < Re < 2874$	$59.51 < Eö < 117.16$	$15.73 < Eö < 25$	$13.19 < We < 18.35$	$6.78 < We < 8.48$	$20.9 < d_{ae} < 29.4$	$10.8 < d_{ve} < 13.6$	$0.32 < d_{ae}/W < 0.45$	Rectilinear
Cap	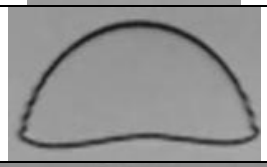	$6223 < Re < 8042$	$2874 < Re < 3357$	$117.16 < Eö < 219.90$	$25 < Eö < 38.31$	$18.35 < We < 22.37$	$8.48 < We < 9.34$	$29.4 < d_{ae} < 40.2$	$13.6 < d_{ve} < 16.8$	$0.45 < d_{ae}/W < 0.62$	Rectilinear
Cap-bullet	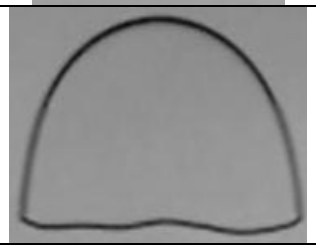	$Re > 8042$	$Re > 3357$	$Eö > 219.90$	$Eö > 38.31$	$We > 22.37$	$We > 9.34$	$d_{ae} > 40.2$	$d_{ve} > 16.8$	$d_{ae}/W > 0.62$	Rectilinear

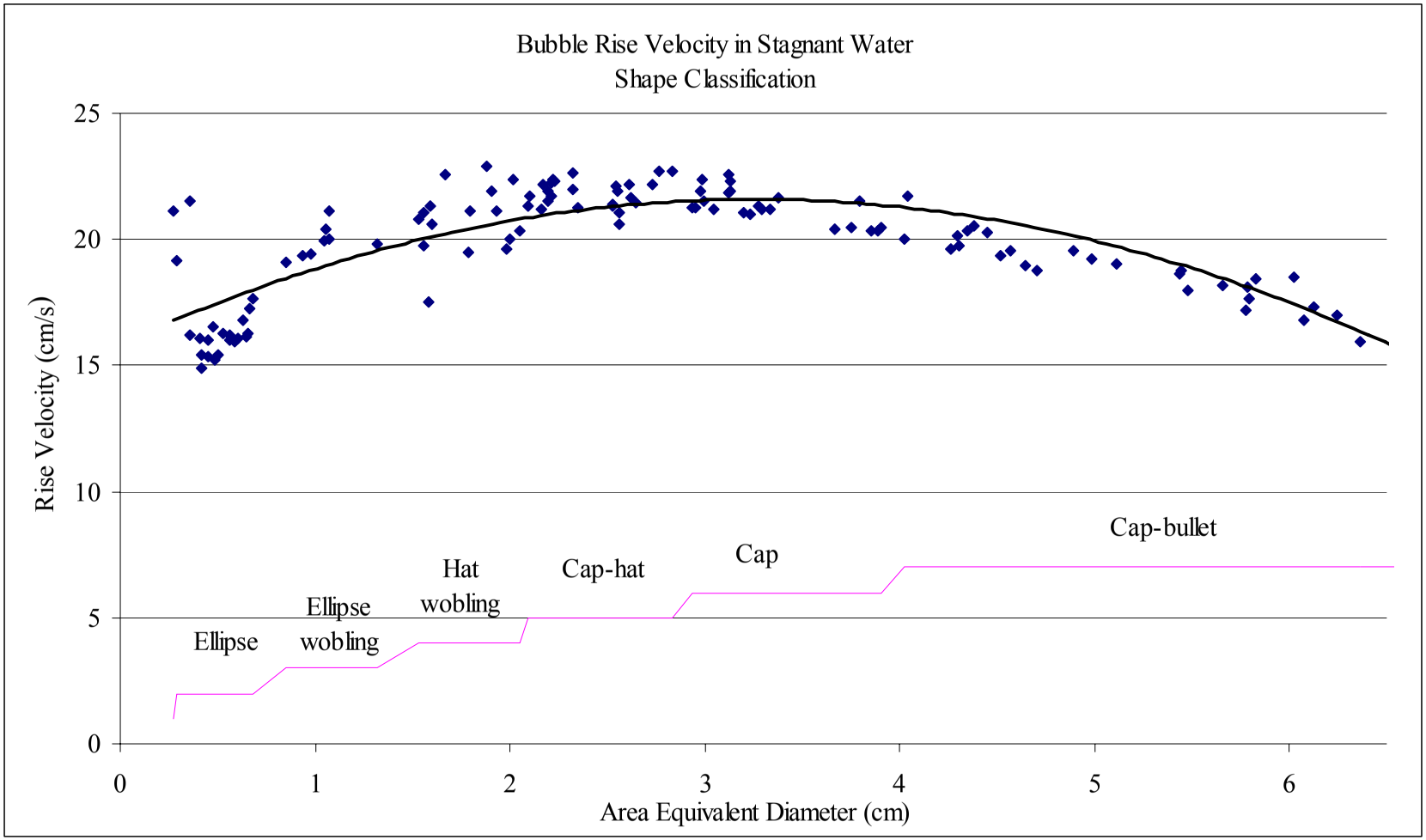

Figure 5.8 Bubble rise velocity and bubble shapes in stagnant water at 21 ^{o}C.

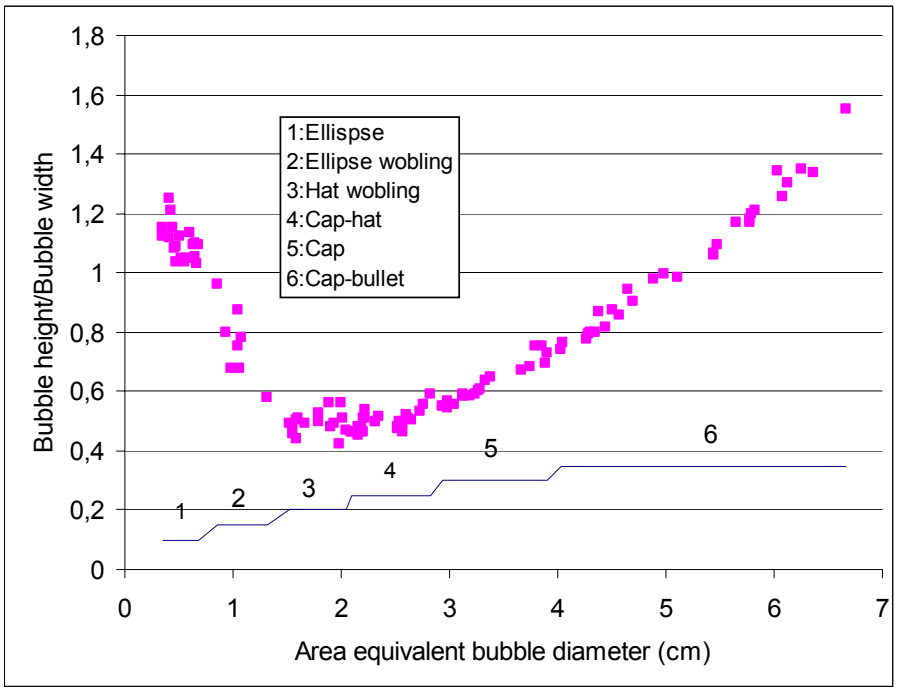

Figure 5.9 Bubble shape deformation with area equivalent bubble diameter

Bubble deformation due to channel side wall effect is observed in Figure 5.9 as bubble height to bubble width ratio versus area equivalent bubble diameter. This figure shows that bubble height to bubble width ratio decreases due to bubble deformation because of volume increase and wake effects up to d_{ae}≈15 mm. If bubble diameter is increased, the bubble height to bubble width ratio increases due to bubble type change and channel side wall effect.

The paths of the bubbles can be categorized as follows:

a) Bubbles having d_{ae}<2.7 mm move with a rectilinear motion if the *Re* number based on U_{bvc} and d_{ae} is less than 579, the bubble continues to move on a rectilinear path. In this range Reynolds number corresponding to U_{bvc} and d_{ve} is less than 527 and bubble shapes are circular in 2D. For 3D case d_{ve} < 1.3 mm is generally acceptable condition for spherical bubbles [22].

b) If the Reynolds number based on U_{bvc} and d_{ae} is greater than 579 and less than 3170 the bubbles are ellipse in shape and move on a sinusoidal path.

c) For 15.3 mm < d_{ae}< 20.9 mm, bubbles move on an unstable sinusoidal, or rectilinear irregular path with ellipse wobbling or hat wobbling shape. In this range, Reynolds number based on U_{bvc} and d_{ae} is greater than 3170 and less than 4454.

d) Bubbles rise in rectilinear motion when d_{ae} > 20.9 mm. In this range bubble shapes are in cap type. For 3D case, transition value from ellipse to cap bubbles is accepted as d_{ve} = 17 mm [22].

As it can be seen from the Table 5.3 and Figure 5.8, bubble shapes consist of circular, ellipse, ellipse wobbling or hat wobbling (irregular), cap-hat, cap and cap-bullet types. Ellipse wobbling or cap-hat wobbling type bubble regions are transition from ellipse to cap region. Rise velocities in this region are scattered. Cap-hat type bubbles were obtained in all tests. In the literature, however, to the best of author's knowledge, such type of bubbles was not observed previously or possibly cap-hat type bubbles were considered in the group of cap type bubbles. However, bubble width of cap-hat type bubbles is larger than the same area equivalent diameter size cap bubbles so, the behavior of hat type bubbles deviates from that of the cap bubbles.

Two main types of bubble shapes, ellipse bubbles and cap bubbles were tracked and circularity, area equivalent bubble diameter, perimeter, area, volume and rise velocities of nose and center of mass of bubbles were drawn in Figure 5.10 and Figure 5.11.

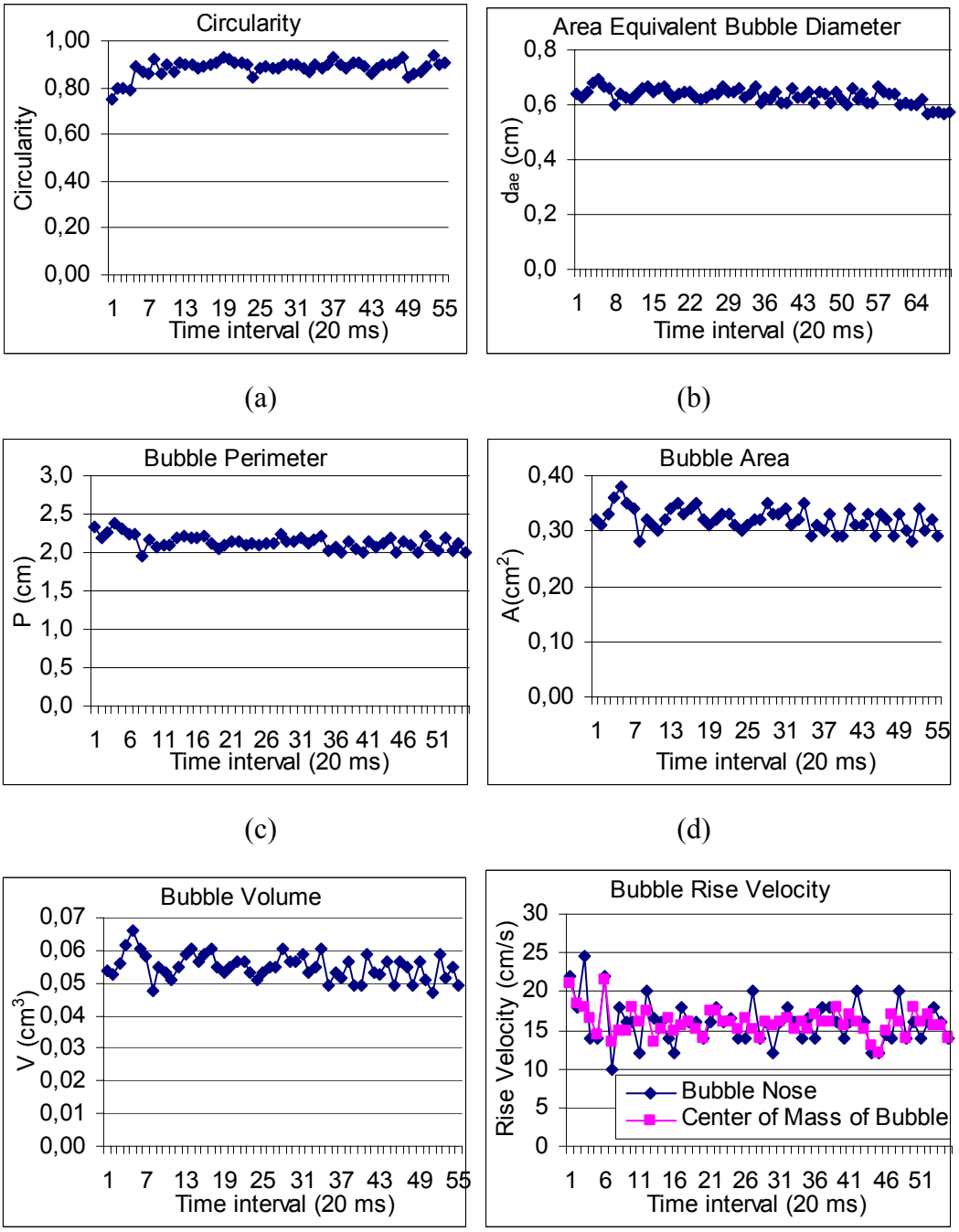

Figure 5.10 Movement of ellipse bubble (Circularity, area equivalent diameter, perimeter, area, volume and rise velocity change of ellipse bubble – Time interval between two successive points is 20 ms)

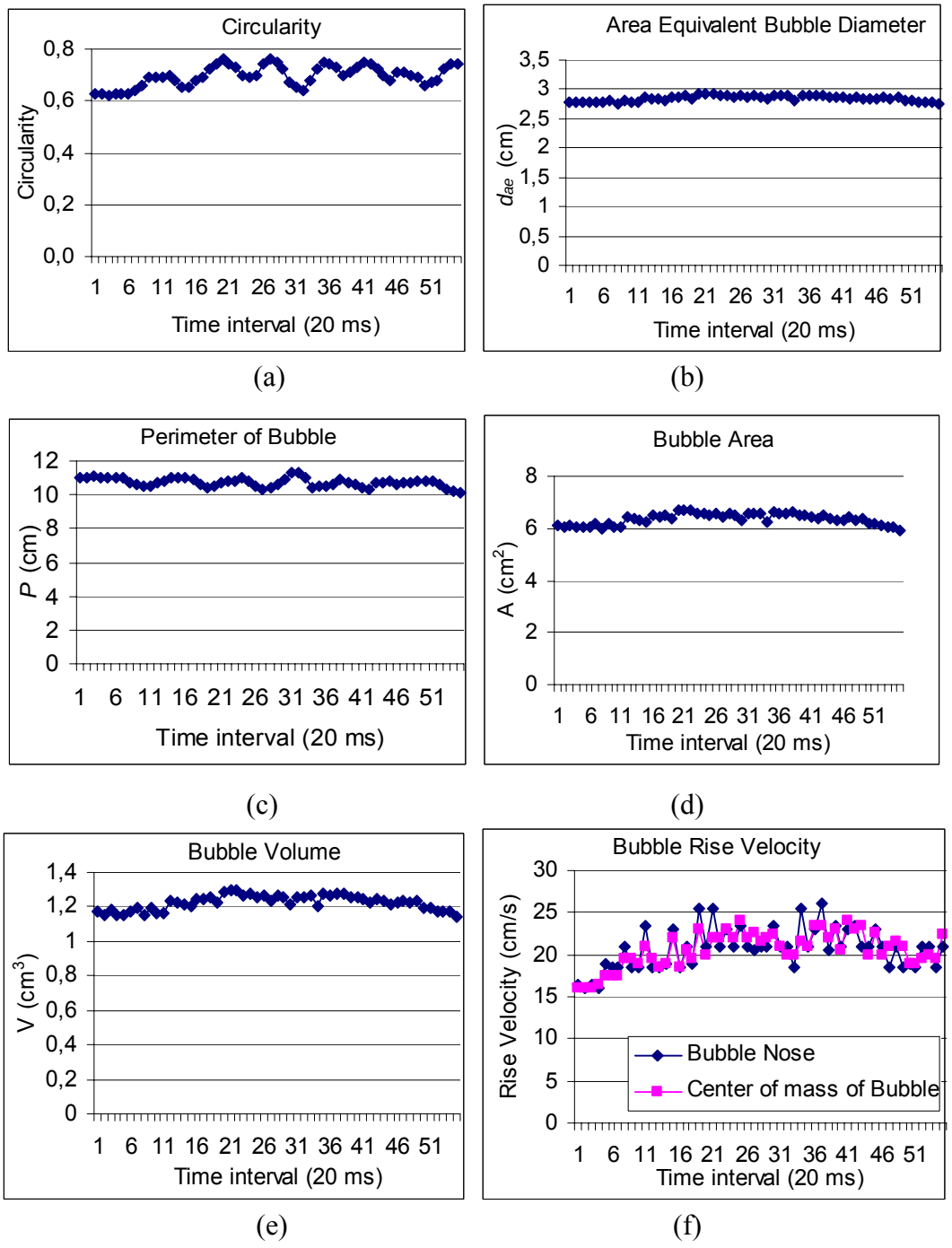

Figure 5.11 Movement of cap bubble (Circularity, area equivalent diameter, perimeter, area, volume and rise velocity change of cap bubble – Time interval between two successive points is 20 ms)

Circular, ellipse and cap bubbles were tracked and bubble paths were obtained.

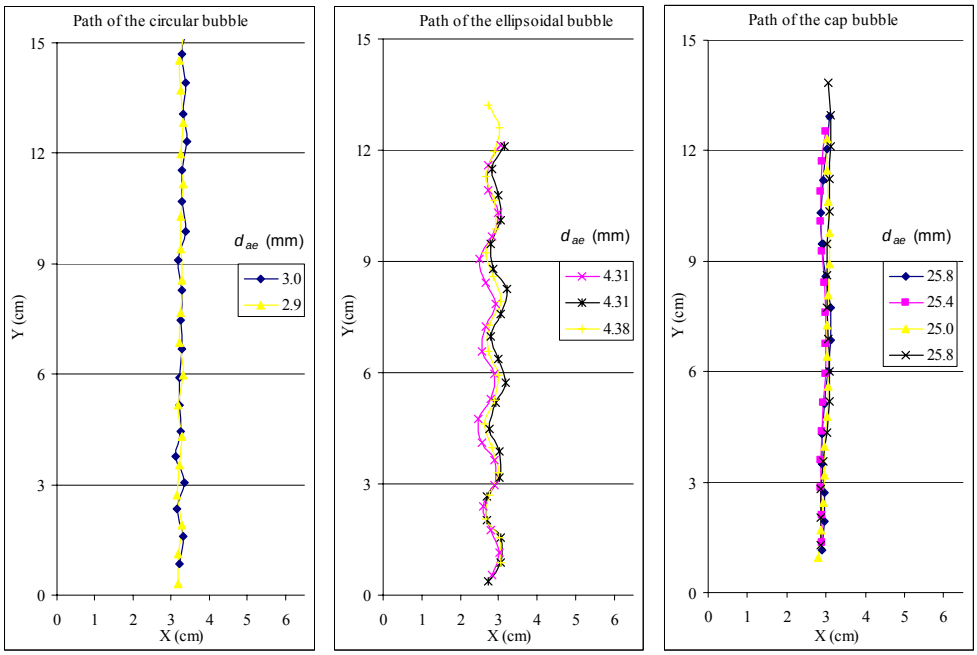

Figure 5.12 Almost circular (circularity ≈ 1) bubble path (left), ellipse bubble path (middle) and cap bubble path (right)

The bubble trajectories inside the channel were tracked. Figure 5.12 shows some of the bubble paths, where X is in lateral direction, and Y is in vertical direction, and the starting point is at almost 20 cm above the bubble injection point. One can see that the bubbles do not follow the same path. Figure 5.12 shows that circular bubbles move in almost a rectilinear path. Increasing the bubble volume changes the circular shape to ellipse shape and the bubble path changes to sinusoidal character. As an example to the sinusoidal path, a simple curve-fit to the bubble path was obtained and given in Figure 5.13. Increasing the bubble volume, therefore the bubble area, amplitude and period of the sinusoidal path increase respectively. Same size ellipse bubbles follow sinusoidal paths with the same amplitude and the same period as shown in Figure 5.12.

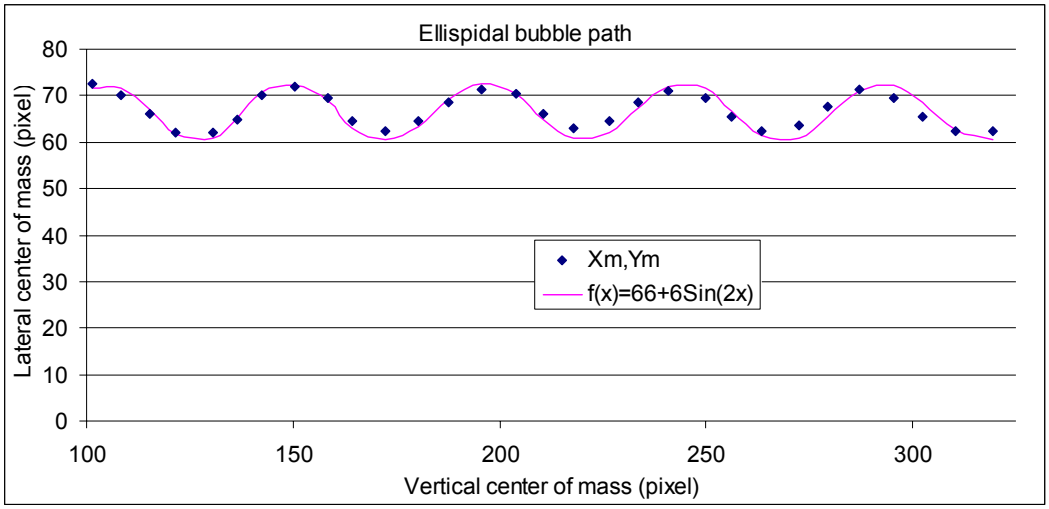

Figure 5.13 Ellipse bubble path with fitted sinusoidal curve

5.5 Rising velocities of air bubbles

After a bubble leaves the orifice of the injector, it rises up through the liquid and eventually it reaches a constant speed, which is referred to as the terminal velocity [22]. The terminal velocity is achieved within a distance of *2d* from the release [22]. Velocity measurements were done from the video records after the bubble reached to the constant speed i.e. terminal velocity.

The rising velocity of the bubble can be calculated from the relative positions of the bubble at a time interval.

To be able to compare the terminal velocities of air bubbles which were obtained from the image analyses in the channel, experimental terminal velocities for air bubbles rising in infinite water medium were investigated from the literature extensively. Rise velocities of air bubbles in infinite water medium were studied by many researchers. Results of these studies are presented in Figure 5.14 for the ellipsoidal regime and adjacent parts of the spherical and spherical-cap regimes [22]. Some of the spread in the data results from experimental scatter, but the greatest cause might be the surface contamination [22]. According to these researches, bubbles are generally classified as; spherical, ellipsoidal and cap types.

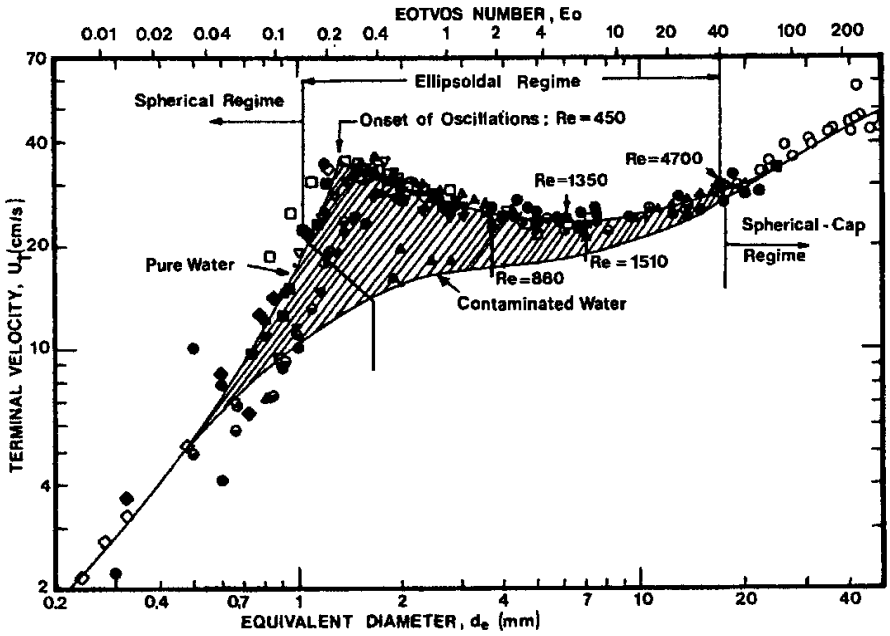

Figure 5.14 The rise velocity of air bubbles in stagnant water at 20 ^{o}C [22]

In the next section, spherical, ellipsoidal and cap type bubbles will be explained briefly and correlations related to the bubble rise velocities will be given. Then, these correlations will be compared with the experimental results which were obtained in the present study.

5.5.1 Spherical (3D) / circular (2D) bubbles

One of the most important analytic solutions in the study of bubbles was obtained independently by Hadamard and Rybczynski [20, 24, 25, 28, 68]. A fluid sphere is considered, with its interface assumed to be completely free from surface-active contaminants, so that the interfacial (surface) tension is constant. Their solution for terminal velocity gives the following result;

$$U_T = \frac{g\, d_{ve}{}^2 \Delta\rho}{6\mu_l}\left(\frac{1+\kappa}{2+3\kappa}\right) \tag{5.3}$$

where κ is the dynamic viscosity ratio of the bubble and the surrounding fluid (μ_b/μ_l). For an air bubble ($\kappa \approx 0$), the terminal velocity is

$$U_T = \frac{g\, d_{ve}{}^2 \Delta\rho}{12\mu_l} \tag{5.4}$$

In the present study, the circular bubbles were obtained when d_{ae}<2.7 mm. In this region bubbles are almost three dimensional in geometry, because channel gap size is 2.1 mm. Thus, this type of bubbles was not studied in two dimensional geometry with this test section because three dimensional effects are significant.

5.5.2 Ellipsoidal (3D) / ellipse (2D) bubbles

The two curves in Figure 5.14 are based on those given by Gaudin for distilled water and for water with surface-active contaminant added [22]. Surface-active contaminants affect the rise velocity most strongly in the ellipsoidal range. For d_{ve} > 1.3 mm, (d_{ve} > 1.5 mm [23]) the uppermost (pure system) curve in Figure 5.14 is approximated closely by

$$U_T = \left[2.14 \frac{\sigma}{\rho d_{ve}} + 0.505 g d_{ve} \right]^{1/2} \tag{5.5}$$

which is of the form suggested by a wave analogy [20, 21]. Eq. 5.5 is used to calculate rise velocities of ellipsoidal bubbles in infinite medium when *Eö* <40. Viscous forces can be ignored for ellipsoidal bubbles (See Figure 5.15).

In this section, ellipse bubbles rising in the narrow rectangular channel under stagnant water conditions are analyzed. The range of analyzed ellipse bubbles is 2.7<d_{ae}<8.5 mm without wobbling and 8.5<d_{ae}<15.3 mm with wobbling. To the best of author's knowledge, ellipse bubbles in 2D were not investigated before. The results of the ellipse bubble tests and the correlation of rise velocity of ellipsoidal bubbles in 3D infinite medium are compared (Figure 5.16). While area equivalent bubble diameter was less than 11.6 mm, side walls did not affect the bubble rise velocity significantly, so, it was assumed that ellipse bubbles rise in infinite 2D medium. As it is shown in the Figure 5.16, trend of ellipse bubble rise velocity in 2D is similar to the ellipsoidal bubbles in 3D infinite medium. The following empirical correlation for 2D ellipse bubble was obtained from the experimental data of the present study (See Figure 5.17);

$$U_b = \left[0.5\frac{\sigma}{\rho d_{ae}} + 2.76 g d_{ae} \right]^{1/2} \tag{5.6}$$

This equation can be used for ellipse air bubbles rising in vertical narrow channels with ≈ 2 mm channel gap under stagnant water conditions at ambient temperatures when narrow side walls effects are insignificant.

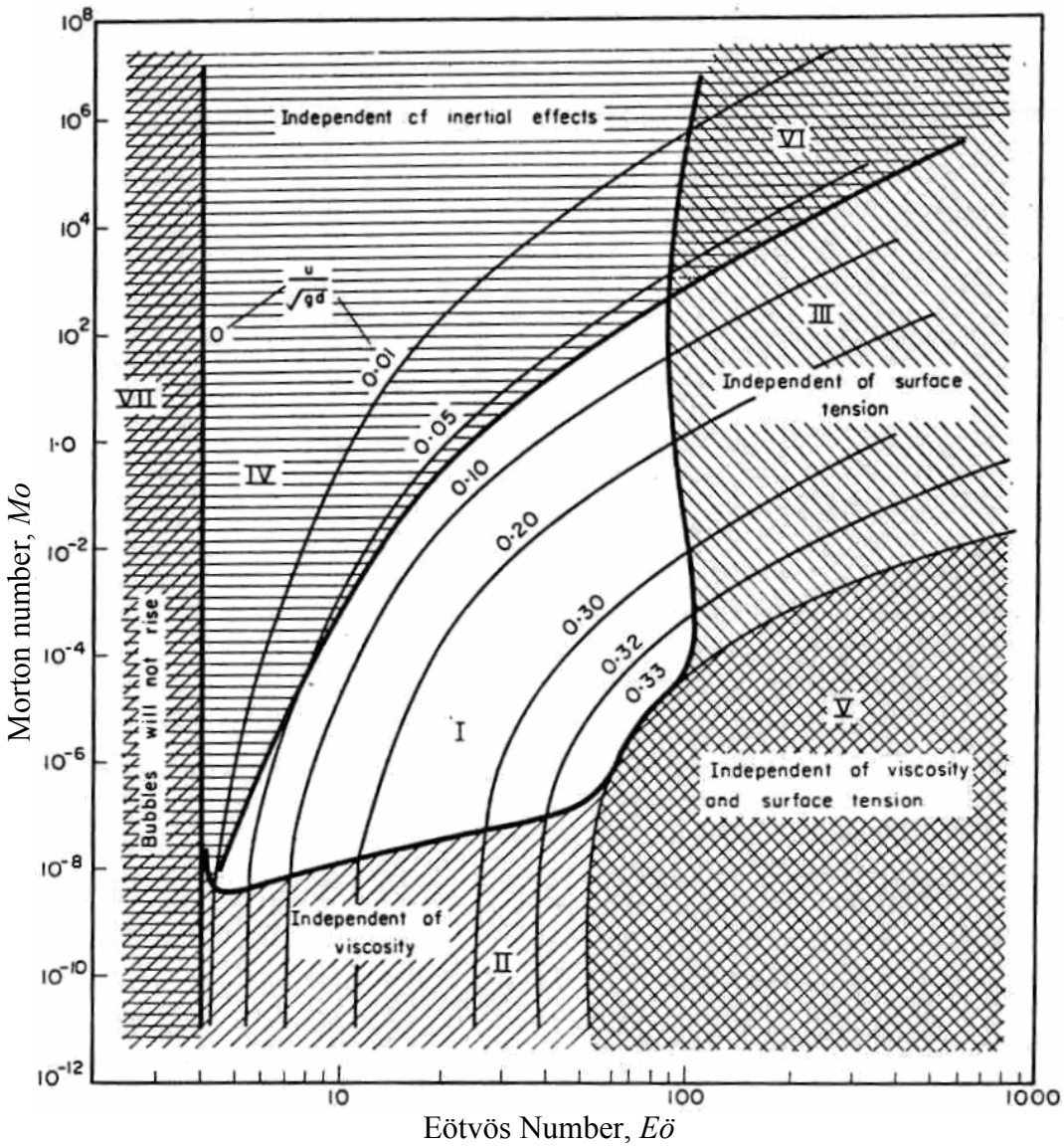

Figure 5.15 Cross-plot of data showing regions in which the effect of some forces becomes unimportant [24]

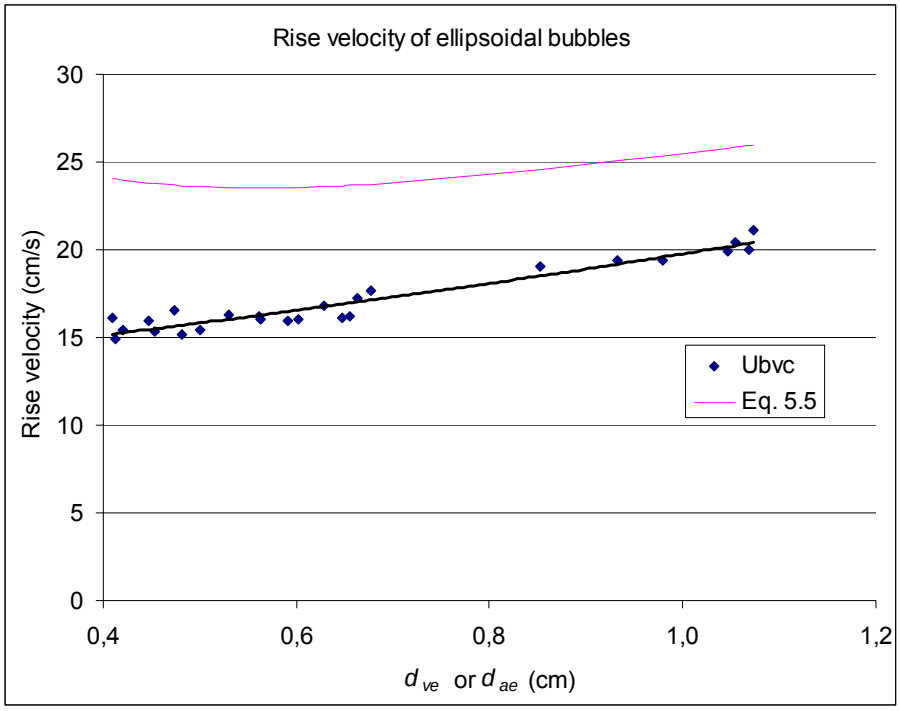

Figure 5.16 Rise velocities of ellipse bubbles in 2D and 3D

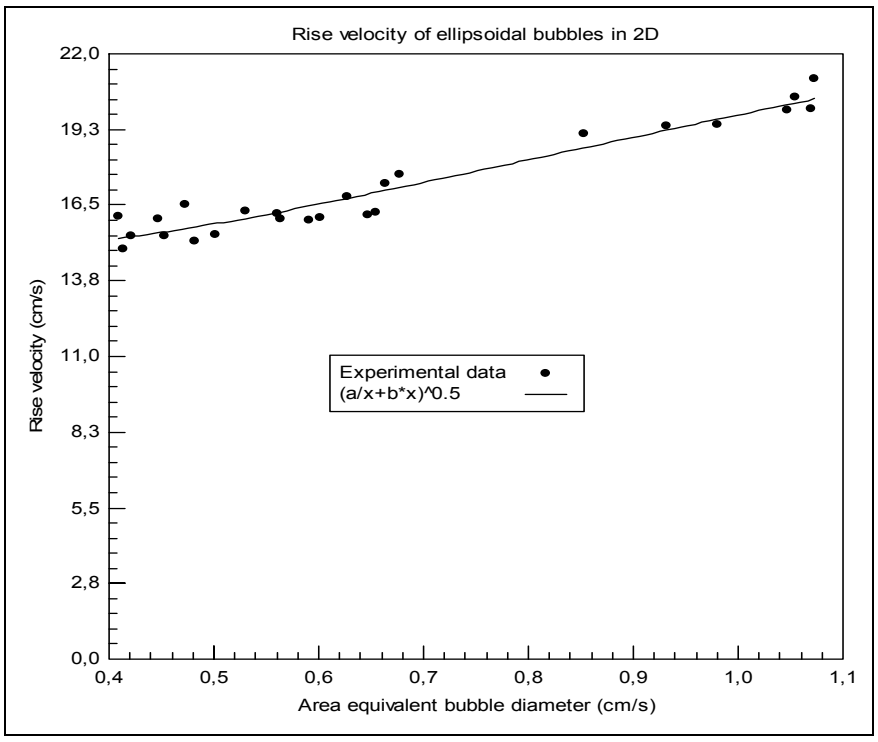

Figure 5.17 Rise velocity of ellipse bubbles in the narrow rectangular channel and curve-fit to the experimental data

5.5.3 Spherical-cap (3D)/ circular-cap (2D) bubbles

In infinite medium, bubbles with $Eö > 40$ and $Re > 1.2$ are in spherical-cap shape. These inequalities are generally satisfied by bubbles with volumes greater than about 3 cm^3 (i.e., $d_{ve} > 18$ mm) [22]. In this range, the shape of bubbles can be closely approximated as a segment of a sphere [22].

Interfacial tension forces can be ignored for spherical-cap bubbles (See Figure 5.15). Flow is considered only in the neighborhood of the bubble nose, where the external fluid is assumed to flow as an inviscid fluid over a complete sphere or spheroid of which the fluid particle forms the cap. Terminal velocity of spherical-cap bubbles is as follows:

$$U_T = \frac{2}{3}\sqrt{gc\frac{\Delta\rho}{\rho_l}} \tag{5.7}$$

which is the Davies and Taylor equation, where c is the radius of curvature of bubble [22].

Spherical-cap bubbles are geometrically similar with a wake angle θ_W of approximately 50^o once Re is greater than about 150. The radius of curvature may then be related directly to d_e yielding

$$U_T = 0.711\sqrt{gd_{ve}\frac{\Delta\rho}{\rho}} \qquad (Re > 150,\ Eö \geq 40) \tag{5.8}$$

Collins [69] investigated 2D bubbles by making bubble tests in narrow vertical channels with 6.35 mm gap and generated an approximate solution for the two-dimensional problem using the method of Davies & Taylor. With the assumptions that viscous and surface-tension forces are insignificant in comparison with inertial forces (See Figure 5.15), and that the gas pressure is constant within the bubble, several theoretical results are known [69]. The corresponding result for the 2D bubble was derived as;

$$U_\infty = 0.5(gc)^{\frac{1}{2}} \tag{5.9}$$

Collins [69] obtained the velocity of cap bubbles in 2D as;

$$U_b = U_\infty \frac{W}{\pi c}\sqrt{\left[3+\left(\frac{3W}{2\pi c}\right)^2\right]-6\left(\frac{W}{2\pi c}\right)^2} \tag{5.10}$$

The result of Collins' study is shown in Figure 5.18. The two-dimensional slug appears to assume a limiting value of $2c/W$=0.62. Birkhoff and Carter quote a value of ~0.7 for the rectangular channel of aspect ratio 4 [69]. In the present study, the limiting value of $2c/W$ equals 0.64 as shown in Figure 5.19 with the channel aspect ratio (W/G) of 31.7.

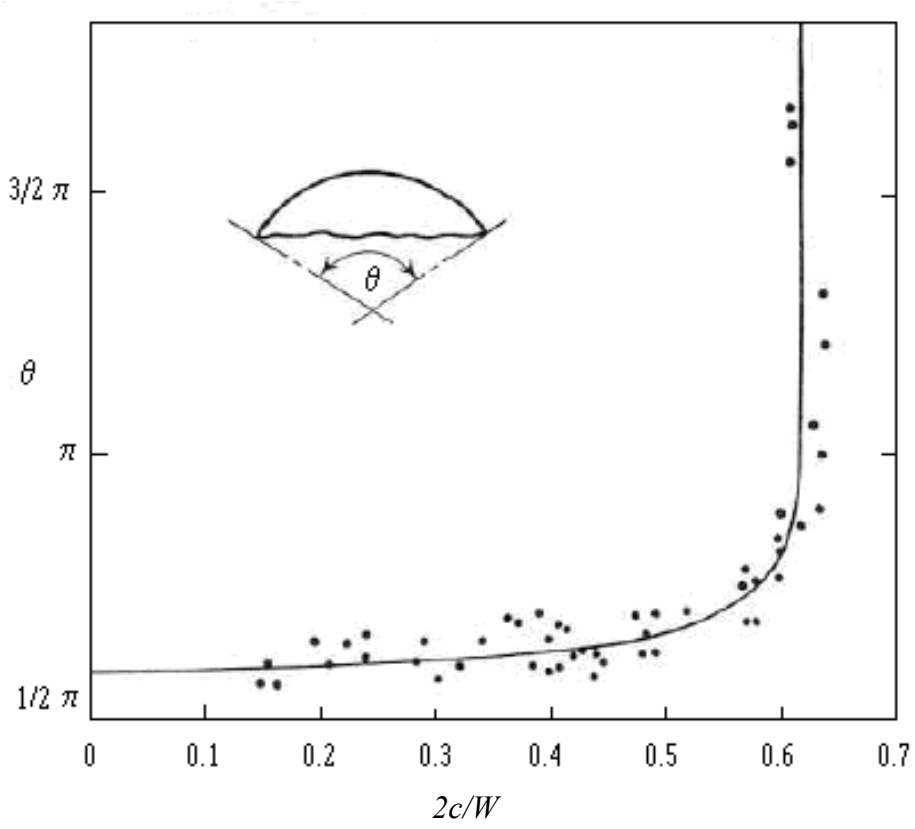

Figure 5.18 Variation of measured wake angle with the radius of curvature to half width of the channel [29]

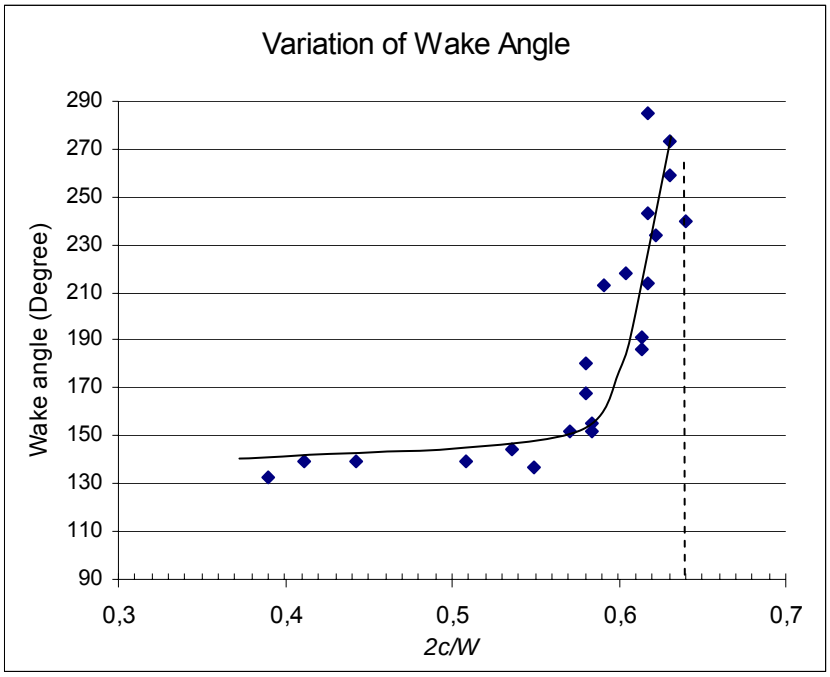

Figure 5.19 Wake angle variation with radius of curvature to the half width of the channel

Grace and Harrison [42] obtained bubble rising velocities for large isolated two-dimensional bubbles in water. They assumed that the angle subtended at the apparent centre of curvature is generally about 105°, the rising velocity of an isolated two-dimensional bubble in water is

$$U_b = 0.615(g)^{\frac{1}{2}}(A)^{\frac{1}{4}} \tag{5.11}$$

The upper limit to the rising velocity of a two-dimensional bubble of area A and the bubble deformation (height of bubble/width of bubble) m is

$$U_b = 0.391m^{-\frac{3}{4}}(g)^{\frac{1}{2}}(A)^{\frac{1}{4}} \tag{5.12}$$

Collins [70] suggested a correlation for cycloidal-cap bubble in 2D as follows;

$$U_b = 0.57\left(gA^{\frac{1}{2}}\right)^{\frac{1}{2}} \tag{5.13}$$

Similar to three-dimensional bubbles, Pyle found that two-dimensional bubbles have the approximate shape of a cylinder section and that their velocity of rise is related to the area of the transverse cross-section by [71]:

$$U_b = 0.58\left(gA^{\frac{1}{2}} \right)^{\frac{1}{2}} \tag{5.14}$$

Tsuchiya and Fan [43] give a correlation for rise velocity of air bubbles in stagnant water through a vertical narrow rectangular channel in terms of d_{ae} by

$$U_b = 0.58\sqrt{gd_{ae}} \tag{5.15}$$

Collins [69] measured the rise velocities of air bubbles in water contained between two vertical parallel plates spaced 10 mm, and obtained the rise velocity for "two-dimensional" spherical-cap bubbles as;

$$U_b = 0.58\left(gA^{\frac{1}{2}} \right)^{\frac{1}{2}} \tag{5.16}$$

The summary of correlations about cap bubble rise velocities for air-water systems in 2D geometry is given in Table 5.4.

Before starting to analyze the cap bubble motion in a vertical narrow channel, an appropriate 2D infinite medium correlation should be decided. For this purpose, Equations 5.9, 5.11, 5.13, 5.14, 5.15 and 5.16 were compared with the experimental data of present work (Figure 5.20). According to the comparison results, Eq. 5.16 is chosen for 2D infinite medium correlation to investigate the wall effect on cap bubbles.

5.6 Wall Effects

There are two ways to obtain cap bubble rise velocity correlations in a vertical narrow channel. First, insertion of bubble deformation information into the equation implicitly, like Eq. 5.10 which contains the radius of curvature information to define bubble deformation and Eq. 5.12 which contains bubble deformation (bubble height / bubble width) information to define bubble deformation, the next step, is to

introduce the side wall effect multiplier ($f(\lambda)=U_b/U_\infty$) to the 2D infinite medium correlation.

Table 5.4 The summary of correlations about bubble rise velocities for air-water systems in 2D geometries

Rise Velocity Correlation	**Remarks**	**Eq. Number**
$U_\infty = 0.5(gc)^{\frac{1}{2}}$	Cap bubbles with radius of curvature c in 2D infinite medium [69]	5.9
$U_b = U_\infty \frac{W}{\pi c}\sqrt{\left[3+\left(\frac{3W}{2\pi c}\right)^2\right]-6\left(\frac{W}{2\pi c}\right)^2}$	Cap bubbles with radius of curvature a[69]	5.10
$U_b = 0.615(g)^{\frac{1}{2}}(A)^{\frac{1}{4}}$	Isolated cap bubbles with area A in 2D[42]	5.11
$U_b = 0.391m^{-\frac{3}{4}}(g)^{\frac{1}{2}}(A)^{\frac{1}{4}}$	Parabolic cap bubbles with area A in 2D and bubble height over width (m) [42]	5.12
$U_b = 0.57\left(gA^{\frac{1}{2}}\right)^{\frac{1}{2}}$	Cap bubbles with area A in 2D [70]	5.13
$U_b = 0.58\left(gA^{\frac{1}{2}}\right)^{\frac{1}{2}}$	Cap bubbles with area A in 2D [69, 71]	5.14 5.16
$U_b = 0.58\sqrt{gd_{ae}}$	Cap bubbles with area equivalent bubble diameter d_{ae} [43]	5.15

First of all, the experimental data of present work were compared with Eq. 5.10 and Eq. 5.12 (Figure 5.21). As shown in Figure 5.21, Eq. 5.10 deviates from the experimental data significantly. On the other hand, the trend of Eq. 5.12 is rather similar to that of the experimental data. Thus, experimental data were correlated in a similar format to Eq. 5.12. For cap bubble rise velocities in a vertical narrow channel, the curve-fitting graphs are shown Figure 5.22 and Figure 5.23. The obtained empirical correlations for cap bubbles are given in Eq. 17 and Eq. 18.

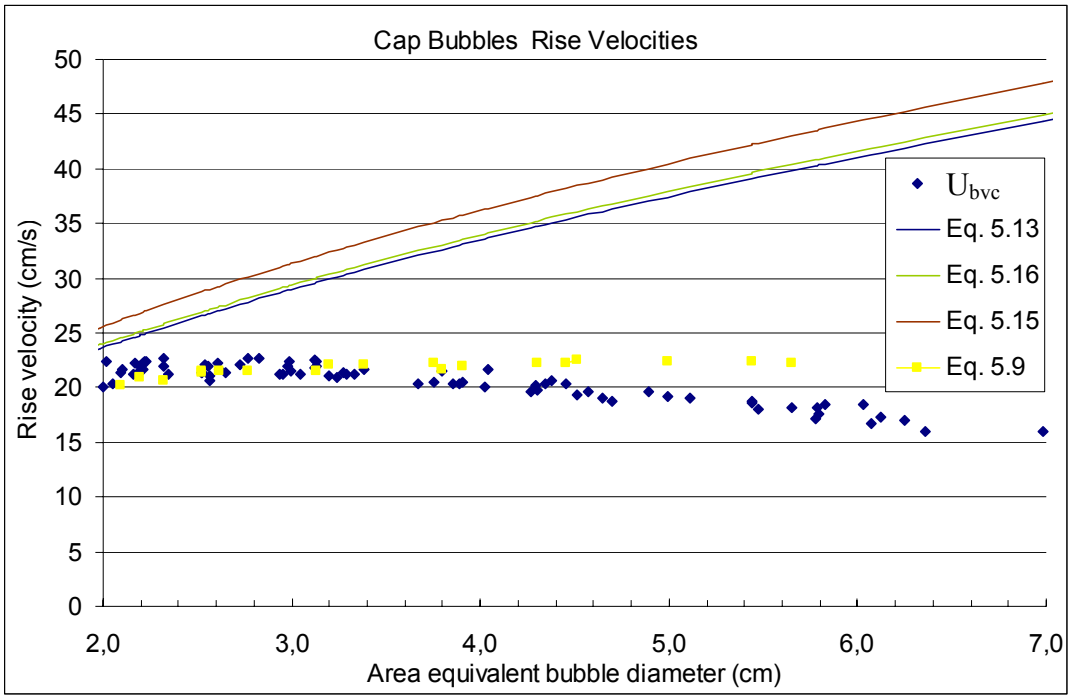

Figure 5.20 Rise velocities of cap bubbles in 2D geometry

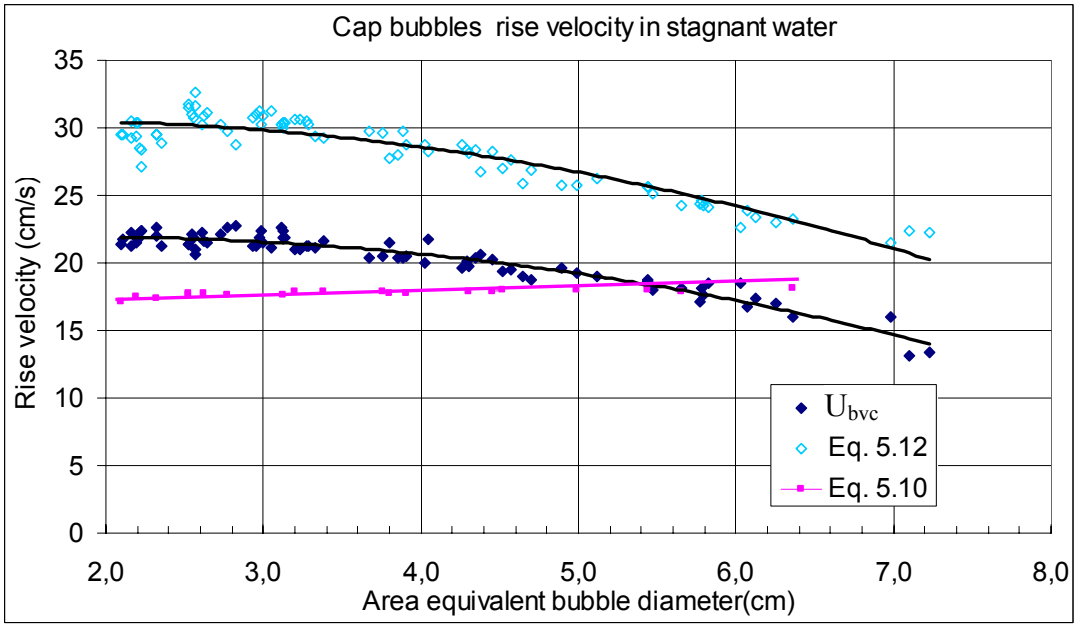

Figure 5.21 Comparison of the experimental results with Eq. 5.10 and Eq. 5.12

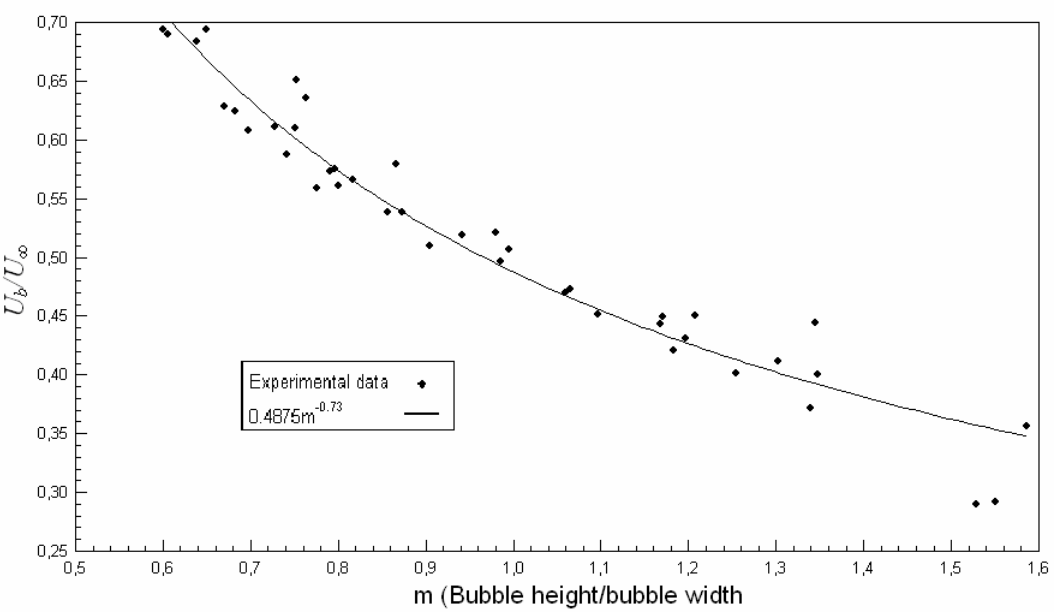

Figure 5.22 Change of U_b/U_∞ with bubble deformation

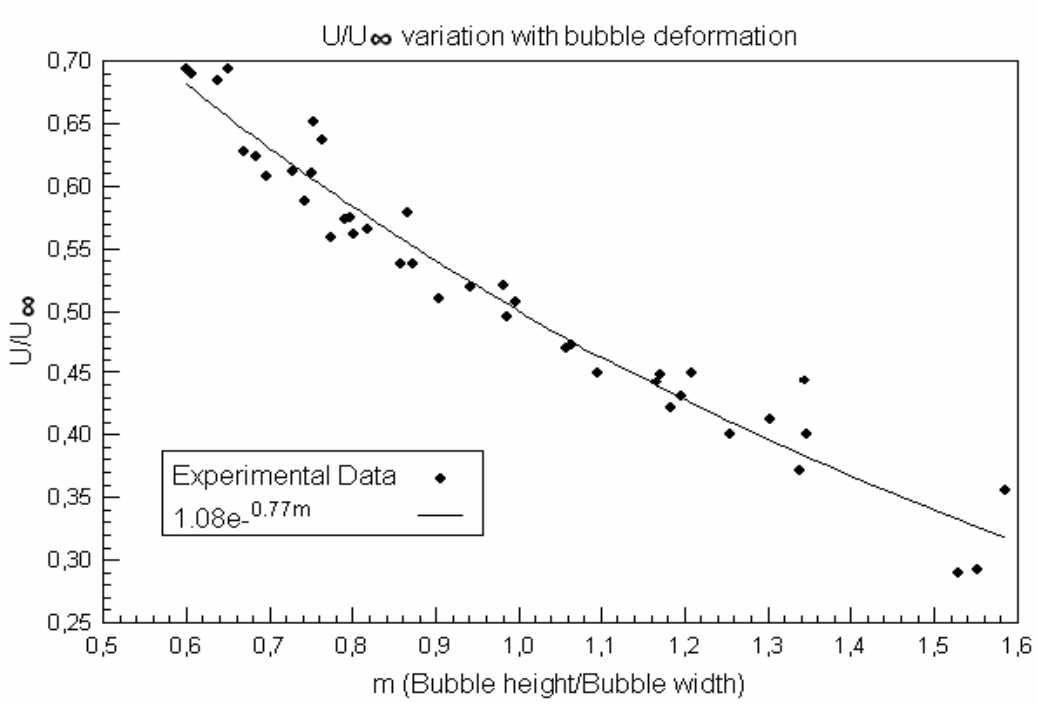

Figure 5.23 Change of U_b/U_∞ with bubble deformation in exponential form

$$U_b = 0.28m^{-0.73}(g)^{\frac{1}{2}}(A)^{\frac{1}{4}} \tag{5.17}$$

$$U_b = 0.624e^{-0.77m}(g)^{\frac{1}{2}}A^{1/4} \tag{5.18}$$

This section presents the experimental investigation of side wall effects on the bubble motion in stagnant water through a vertical narrow rectangular channel. Before starting to discuss narrow rectangular channel case, wall effects on the bubble motion in cylindrical channels will be explained briefly.

The case of a slug gas bubble rising in a vertical tube containing an ideal fluid (i.e. one without viscosity or surface tension) has been treated theoretically by Dumitrescu and Davies-Taylor [24]. Both of them derived that the dimensionless group $U_b/\sqrt{gD}$ (Froude Number) has a constant value, where U_b denotes the terminal rise velocity of the bubble in a vertical tube of diameter D. Dumitrescu theoretically determined the Froude number as 0.351, and a series of careful tests with slug bubbles rising in water in tubes of large diameter resulted in a value of 0.346. In the literature, it is generally agreed that the following simple equation can be used to predict the slug bubble velocity for water in a large round tube [2, 20, 72]:

$$U_b = 0.35\sqrt{gD} \tag{5.19}$$

White and Beardmore [24] presented the results for air bubbles in water and dilute aqueous solutions as shown in Figure 5.24. The criterion for zero bubble velocity has been taken as $Eö \leq 4$, compared with a value of 3.36 given by Hattori, 3.37 by Bretherton, and a value of 0.58 given by Barr [24]. Present experimental data for the narrow vertical channel with 2.1 mm gap size showed that the bubble rise velocity is not zero even though the Eötvös number is much smaller than 3.37.

Mishima *et al.* [30] observed that the width of a slug bubble w was in the range between $0.6W$ and $0.7W$ in their tests. The slug bubble width is in the range between $0.6W$ and $0.85W$. Upper limit of the slug bubble width to the channel with ratio is 0.85.

Owing to the side wall effect, as a gas bubble rises upwards in a narrow channel filled with a stagnant liquid, the rising velocity is generally lower than that in

infinite medium. The ratio of the bubble velocity in the channel to the velocity in an infinite medium U_b/U_∞ can be expressed as a function of the ratio of bubble diameter to the tube diameter $\lambda_{ve}=d_{ve}/D$ [2, 20].

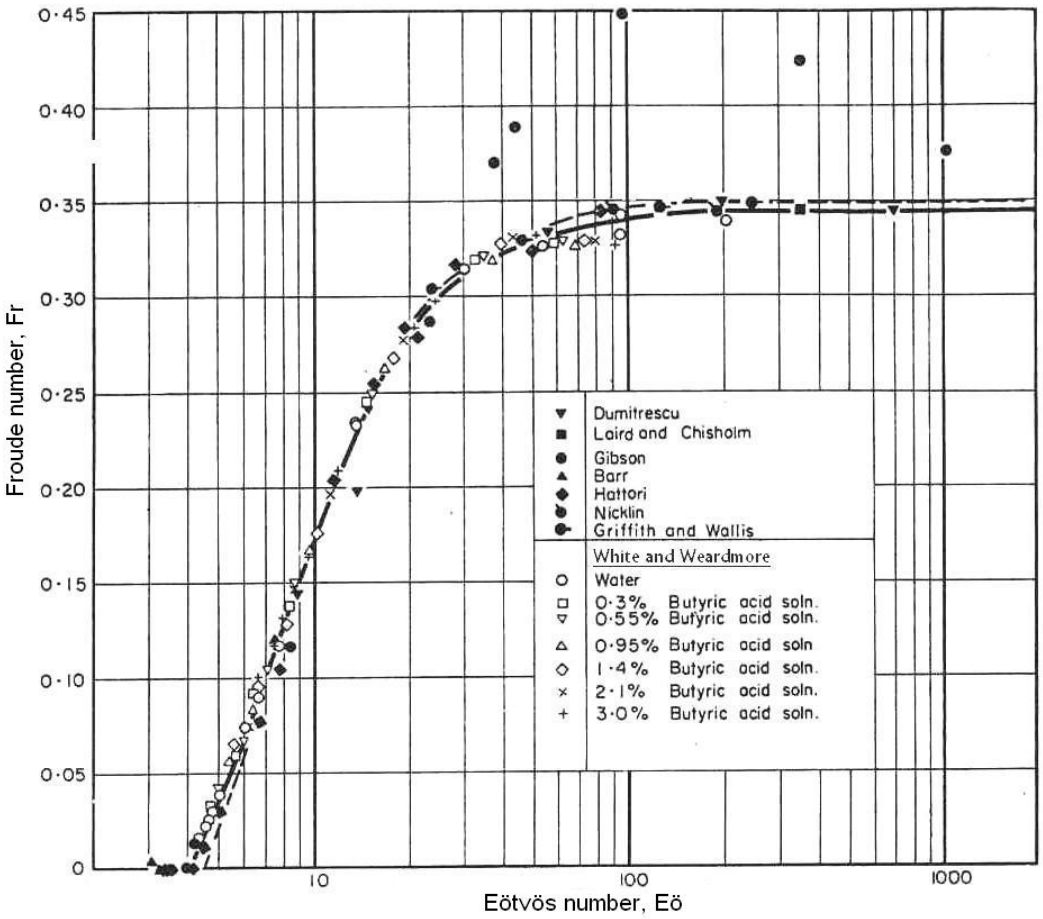

Figure 5.24 Results of cylindrical air bubbles rising in water and dilute aqueous solutions contained in vertical channels [24]

Clift *et al.* [22] recommend the following empirical correlation for the terminal rising velocity U_T of a single bubble in stagnant water through a vertical pipe:

$$\frac{U_b}{U_\infty} = \left(1-\lambda_{ve}^2\right)^{3/2} \quad \text{for } \lambda_{ve} < 0.6 \tag{5.20}$$

where U_∞ denotes the terminal velocity of a single bubble in an infinite stagnant liquid, λ_{ve} is the diameter ratio d_{ve}/D; d_{ve} is the volume equivalent diameter of a bubble and D the pipe diameter. Eq. 5.22 is recommended for $Eö < 40$, $Re > 200$ and $\lambda_{ve} \leq 0.6$. This range corresponds to ellipsoidal bubbles in air-water systems.

Experimental results show that wall effects are negligible for λ up to about 0.125 for spherical-caps in air-water systems [22]. Collins [69, 73] carried out a thorough study of the influence of containing walls on the velocity of spherical-cap bubbles. A simpler equation proposed by Wallis [72] which agrees well with the results of Collins is

$$\frac{U_b}{U_\infty} = 1.13e^{-\lambda_{ve}} \qquad \text{for } 0.125 \leq \lambda_{ve} \leq 0.6 \tag{5.21}$$

For a single gas bubble of equivalent diameter d_{ve} rising in a liquid inside a cylindrical column of diameter D, Collins [73] gives the following expression for the rise velocity (see also Clift *et al.* [22], Tsuchiya and Fan [43], Walters and Davidson [49], and Wallis [72]) wherein a scale factor SF is introduced into the classical Davies–Taylor relation:

$$U_b = 0.71\sqrt{gd_{ve}}SF \tag{5.22}$$

$$SF = 1 \qquad \text{for } \lambda_{ve} < 0.125$$

$$SF = 1.13e^{-\lambda} \qquad \text{for } 0.125 < \lambda_{ve} < 0.6$$

$$SF = 0.496\sqrt{\frac{D}{d_{ve}}} \qquad \text{for } \lambda_{ve} > 0.6$$

The scale factor, *SF,* corrects the Davies-Taylor relation for the influence of the wall on the single bubble rise velocity [74].

It should be noted, however, that the above conclusions concerning the bubble velocity are drawn based on the tests in circular channels.

A corresponding set of relations for cap bubbles, rising in 2D columns was not available in the literature until the study of Krishna *et al.* [74]. Pyle and Harrison made an experimental study for 2D gas bubbles in rectangular channels and correlated their experimental data with the following expression

$$U_b = 0.48\sqrt{gd_{ae}} \tag{5.23}$$

where d_{ae} is the diameter of air bubble having the same area as the 2D bubble [74]. The experimental data of Pyle and Harrison, however, shows considerable scatter and their developed relation in Eq. 5.25 is not very convincing [74].

Krishna *et al.* [74] made an experimental study on 2D bubbles in narrow vertical channels and modeled their test section in the CFD code CFX 4.1c. The test section dimensions are 0.5 X 300 X 4000 mm. The bubble sizes used in the air–water tests are in the range of 17–100 mm.

Furthermore, Krishna *et al.* [74] had suggested that the volume-of-fluid (VOF) method is able to provide an accurate description of the bubble rise velocity. The rise velocity data from VOF simulations were combined with his experimental data and the following correlation for 2D cap bubbles in finite width channels was obtained:

$$U_b = 0.62\sqrt{gd_{ae}}SF \tag{5.24}$$

$$SF = 1 \qquad \text{for } \lambda_{ae} < 0.07$$

$$SF = 1.1e^{(-1.55\lambda_{ae})} \qquad \text{for } 0.07 < \lambda_{ae} < 0.4$$

$$SF = 0.38\lambda_{ae}^{-1/2} \qquad \text{for } \lambda_{ae} > 0.4$$

The rise velocity of single gas bubbles in the size range d_{ae}=0.015–0.12 m were found to decrease significantly with increasing ratio of bubble diameter to channel width, d_{ae}/W. The rise velocity of a 2D cap bubble is 10–30% lower when compared with a 3D spherical cap bubble having the same equivalent diameter. It was also noted from Eq. 5.24 that for narrow channels the value of the Fr Number is 0.236 which matches closely with the value derived theoretically by Collins (who gives 0.23) and Garabedian (who gives 0.238) [21].

The stable bubble range in Krishna *et al.*'s tests is 17 - 100 mm [74]. The channel width is 300 mm. Reliable experimental data range is just one third of the channel width. Cap bubble rise velocity correlation given by Krishna *et al.* mostly depends on VOF simulations. To obtain reasonable empirical correlations more reliable and

wide range of experimental data are needed to investigate the wall effects in narrow rectangular channels.

For rectangular channels with a cross section *(W X G)* the terminal velocities of slug bubbles were given as

$$U_T = \left[0.23 + 0.13\frac{G}{W}\right]\sqrt{gW\frac{\Delta\rho}{\rho}} \tag{5.25}$$

where $G<W$ by Griffith and Wallis [72]. Clift [22] emphasizes that this correlation is not validated experimentally for narrow rectangular channels. However, this correlation was used by some researchers [13, 17, 35] in two-phase flow regime studies for vertical narrow channels.

The summary of wall effect correlations for rise velocity of cap bubbles in vertical narrow rectangular channels is given in Table 5.5.

Table 5.5 The summary of correlations about wall effect on the bubble rise velocities for air-water systems in 2D geometries

Rise velocity correlations	**Remarks**	**Dim.**	**Eq. Num.**
$U_b = 0.48\sqrt{gd_{ae}}$	Cap bubbles in narrow channels [74]	2D	5.23
$U_b = 0.62\sqrt{gd_{ae}}SF$ $SF = 1$ for $\lambda_{ae} < 0.07$ $SF = 1.1e^{(-1.55\lambda_{ae})}$ for $0.07 < \lambda_{ae} < 0.4$ $SF = 0.38\lambda_{ae}^{-1/2}$ for $\lambda_{ae} > 0.4$	Cap bubbles in narrow channels [74] SF: Shape factor	2D	5.24
$U_T = \left[0.23 + 0.13\frac{G}{W}\right]\sqrt{gW\frac{\Delta\rho}{\rho}}$	Slug bubbles in rectangular channels with cross section *W*x*G* [20, 72]	2D	5.25

The cap bubble rise velocities tested in this study are presented in Figure 5.25. For comparison, the bubble velocities predicted by Eqs. 5.23 through 5.25 are also plotted in Figure 5.25. It is seen that the prediction of Eqs. 5.23 through 5.25 deviates substantially from the experimental data for the vertical narrow rectangular channel. Therefore, a new empirical correlation for cap bubble rise velocity is needed. For this purpose, experimental data was used to obtain a bubble rise velocity correlation. The results are shown in Figure 5.26. The obtained cap bubble rise velocity correlation is as follows;

$$\frac{U_b}{U_\infty} = 1.336e^{-1.31\lambda_{ae}} \tag{5.30}$$

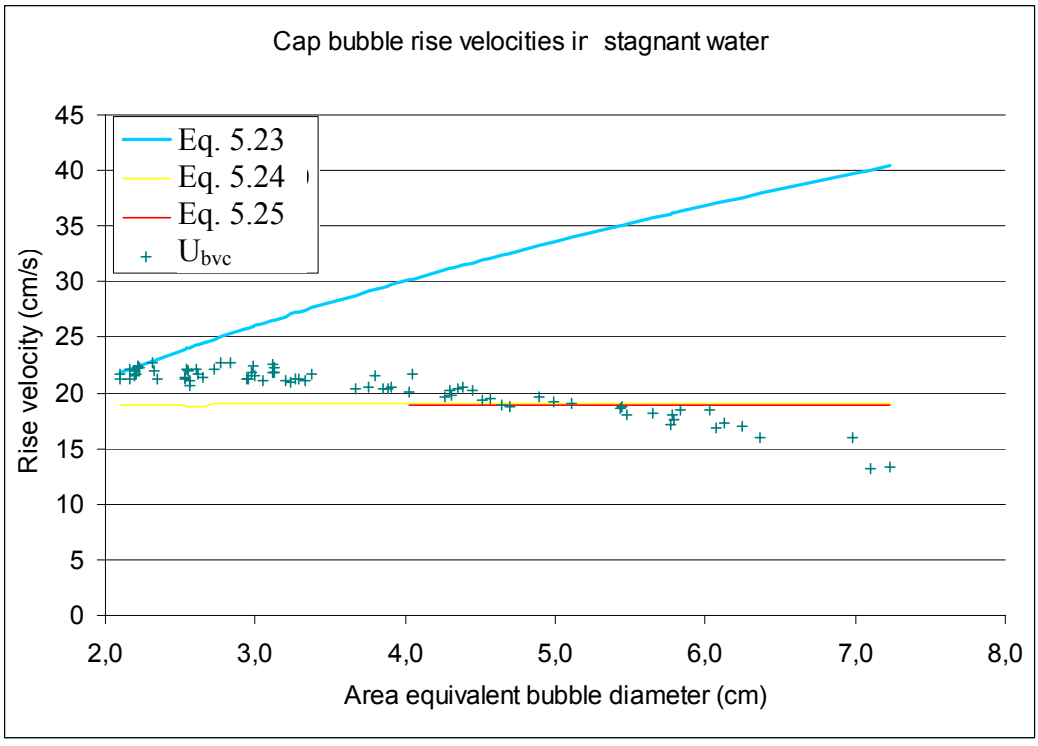

Figure 5.25 Rise velocities of cap bubbles in stagnant water (2D)

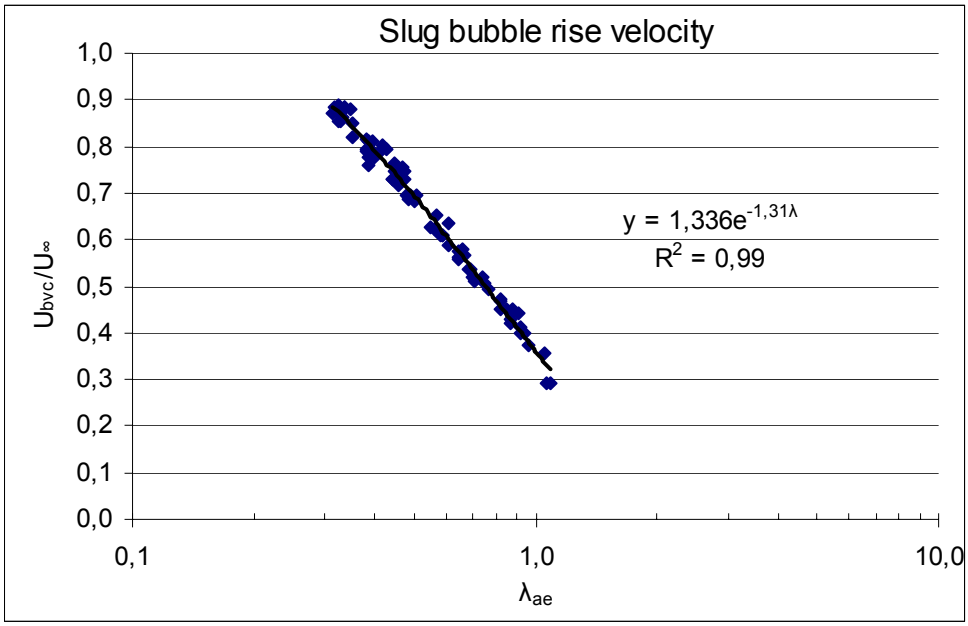

Figure 5.26 Rise velocities of slug bubbles in vertical narrow channels

CHAPTER 6

RISING OF AIR BUBBLES IN FLOWING WATER THROUGH A VERTICAL NARROW RECTANGULAR CHANNEL

6.1 Introduction

In this chapter, air bubble motion in upward co-current water with a velocity range of 0 cm/s < U_l < 25 cm/s through a vertical narrow rectangular channel will be discussed.

The water velocity range is determined due to natural circulation conditions in TR-2 nuclear research reactor in an accident scenario. In this situation, water flow is in upward direction with a velocity range of 0 cm/s < U_l < 25 cm/s. Another reason is that it is not possible to obtain accurate and reliable measurements for higher velocities with ordinary digital camcorders of 25 frames/s speed. A high speed and/or high resolution digital video camera is required to obtain reasonable results from image analyses for higher liquid velocities.

Velocity profile of the liquid phase is an important parameter which can affect the bubble motion in liquid stream. In present study, monitoring the velocity profile was not possible because of lack of necessary measuring equipment. However, 3-D model of the test section was generated in CFD code-Fluent 6.1 and velocity profiles in the tests were obtained with appropriate initial and boundary conditions using the CFD code. CFD codes are reliable on such analysis, especially on single phase flow [20].

Figure 6.1.a shows the lateral velocity profile of water along the channel width at y=50 cm and z=0.105 cm. Figure 6.1.b shows the velocity profile along the channel

gap at y=50 cm, and x=3.325 cm. The velocity profile seems to be uniform in lateral direction in the core region (0.5 < x < 6.15 cm). All types of bubbles generated in the tests are within this flat velocity profile region.

Liquid velocity profiles at the test section were calculated and plotted with the CFD code in Figure 6.2 and Figure 6.3 for 11.5 cm/s and 25 cm/s water inlet velocities respectively. As it is understood from these figures, the velocity profiles are almost flat in the range of 0.5 < x < 6.15 cm along the channel width.

Another verification of uniform velocity profile is from the experimental results of Vasollo and Kumar's work [13]. They measured water velocity profiles with Laser Doppler Velocimeter (LDV) probes in a vertical narrow rectangular channel (62 mm X 2.5 mm) which is almost the same size as the test section of present study (Figure 6.4).

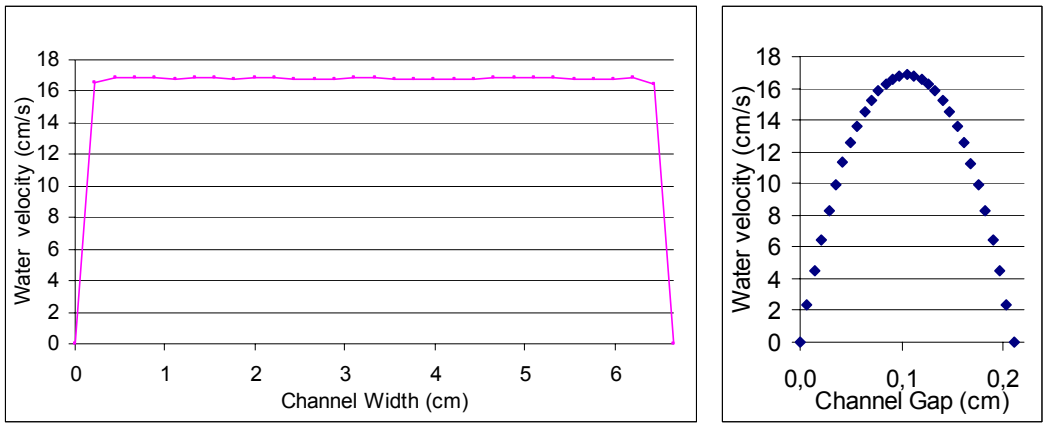

(a) (b)

Figure 6.1 Water velocity profile in the channel with inlet velocity 11.5 cm/s (a: velocity profile along the channel width at the center of channel gap, b: velocity profile along the channel gap at the center of channel width)

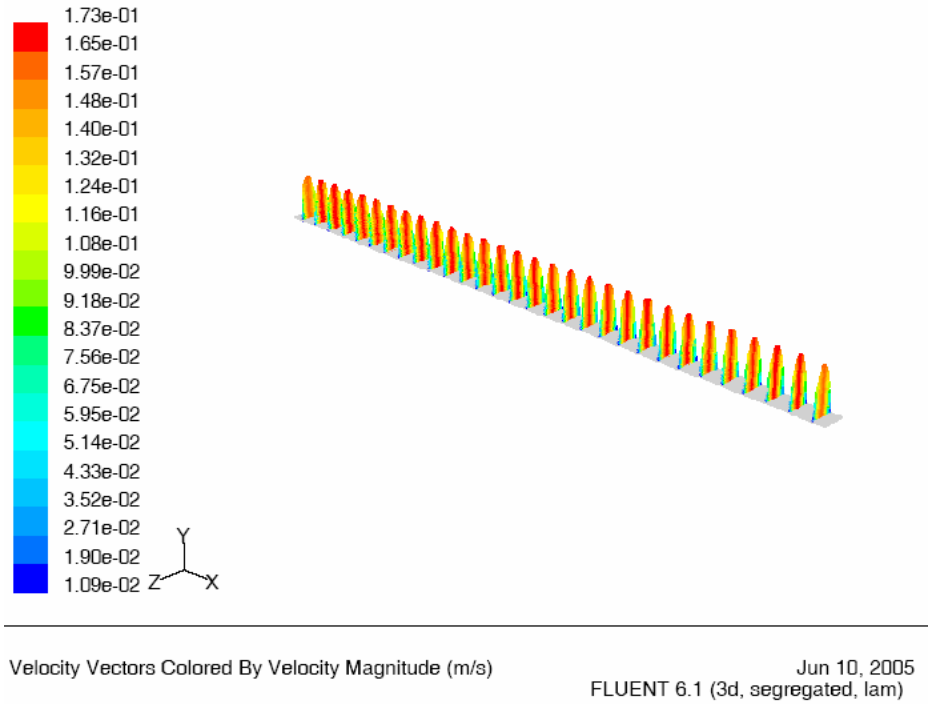

Figure 6.2 Liquid velocity profile at x-z plane where y=50 cm (inlet water velocity is 0.115 m/s)

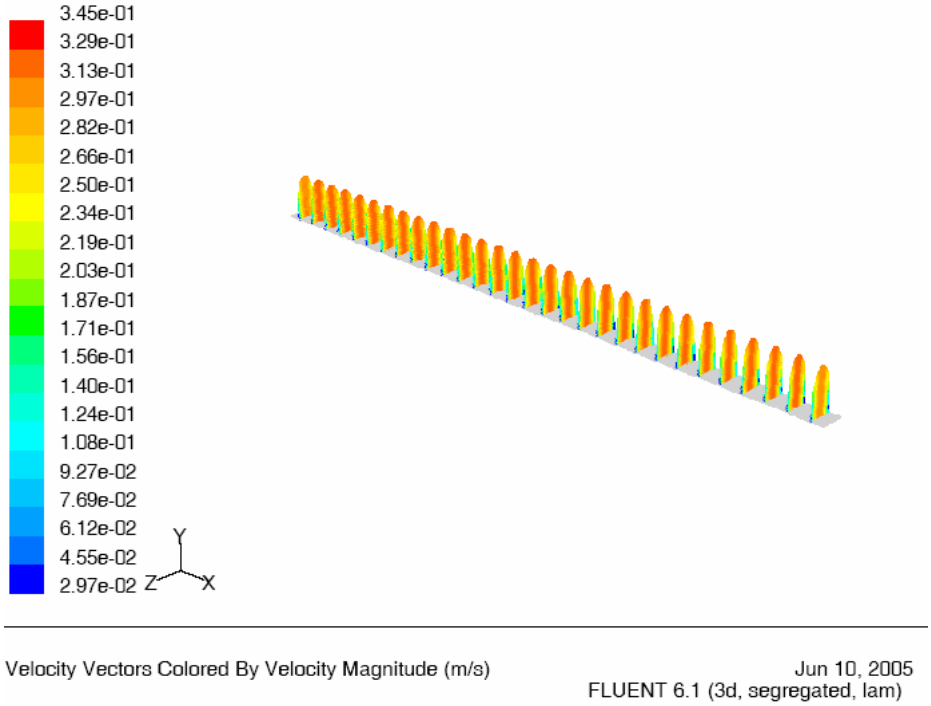

Figure 6.3 Liquid velocity profile at x-z plane where y=50 cm (inlet water velocity is 0.25 m/s)

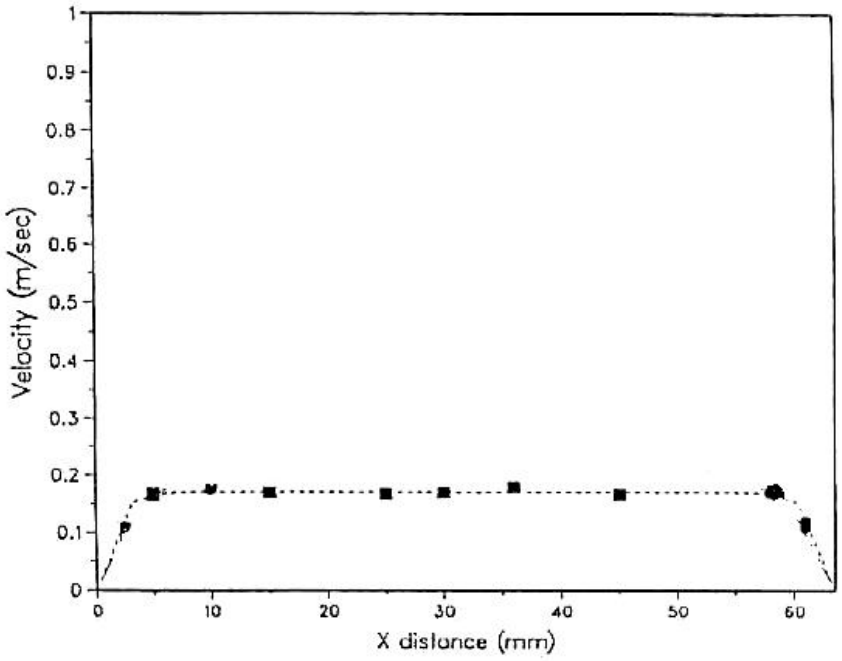

Figure 6.4 Water velocity: measured by Vasollo and Kumar (U_l =0.1425 m/s inlet velocity) [13]

The results of the CFD model and Vasollo and Kumar's [13] work showed that velocity profile can be assumed uniform in lateral direction, except about 5 mm distance from the side walls.

Thus, the air bubble relative velocity can be obtained from the measured bubble velocity and the mean water velocity values by using the following equation;

$$U_b = U_{br} + U_l \tag{6.1}$$

where U_b is the rise velocity of bubble, U_{br} is the relative velocity of the bubble and U_l is the mean vertical water velocity.

Therefore, the relative velocity of the bubble can be calculated from the following equation:

$$U_{br} = U_b - U_l \tag{6.2}$$

To define the air-water system used in this test set, two Reynolds numbers are required. These are the Reynolds number of the water flow based on the channel

hydraulic diameter and Reynolds number of the air bubble based on the area equivalent diameter of bubble, which are defined as;

$$\mathrm{Re}_l = \frac{\rho_l D_h U_l}{\mu_l} \text{ and } \mathrm{Re}_b = \frac{\rho_l d_{ae} U_{br}}{\mu_l} \tag{6.3}$$

It is to be noted that the presence of a single air bubble has a negligible effect on the water bulk velocity.

6.2 Bubble shapes and bubble deformation in water stream

The shape of the bubbles is nearly ellipse when d_{ae} < 15 mm in water stream. At an equivalent bubble diameter above 15 mm, the bubbles tend toward the cap type although there is large oscillation in the major dimensions when the liquid velocity increases (Figure 6.5).

Observations of ellipse bubbles in these experimental runs are in a good consistency with observations under stagnant water conditions as shown in Figure 6.5. The difference is in the bubble paths where the period of the bubble path increases if liquid velocity increases. Cap bubbles are much more deformed when water velocity increases and shape oscillations are more pronounced than those in the stagnant water case.

Bubble shape classification and bubble deformation (bubble height to bubble width ratio) for water velocities of 2.15, 11, 21, and 25 cm/s are given in Figure 6.6, Figure 6.7, Figure 6.8 and Figure 6.9, respectively. Cap-hat type bubbles could not be seen in 11, 21, and 25 cm/s water streams. To be able to compare these results, bubble deformation for water velocities of 2.15, 11, 21, and 25 cm/s are drawn at the same plot as shown in Figure 6.10. Minimum value of bubble deformation is almost same for all water velocities.

Bubble deformation increases in cap-bubble region where $\lambda_{ae} \geq 0.3$ for 2.15, 11, 21, and 25 cm/s liquid velocities. The cap bubble region is shown in Figure 6.11. The trends of the bubble deformation for various water stream velocities are almost similar. Therefore, it is possible to correlate the bubble deformation with an appropriate equation.

$$m = \frac{Bubble \quad height}{Bubble \quad width} = f(U_l) f(\lambda_{ae}) \tag{6.4}$$

where U_l is the mean velocity of water, and λ_{ae} is the area equivalent bubble diameter to channel width ratio. $f(\lambda_{ae})$ part of the equation is independent of water velocity and it shows an exponential behavior. First of all, this part is obtained from the experimental data. After that, $f(U_l)$ was adjusted so as to yield the best correlation with the measured values. As a result, it could be confirmed that the following equation is an applicable correlation for bubble deformation in a vertical narrow channel under co-current water stream for $0.3 < \lambda_{ae} < 1$ and $U_l \leq 25$ cm/s;

$$m = \left[0.264 + 0.0085 U_l^{1/2} \right] e^{1.7 \lambda_{ae}} \tag{6.5}$$

Figure 6.12 shows the comparison of the experimental data and the suggested correlation.

6.3 Rise velocity of bubbles in water stream

The rise velocity of individual air bubbles were determined in a water stream with water bulk velocity ranges from 0 cm/s to 25 cm/s, corresponding to a system Reynolds number range of 0 to 1015. Air bubbles range from 5 mm to 70 mm in area equivalent diameter and corresponding bubble Reynolds number based on relative velocity and d_{ae} ranges from 250 to 16000.

It is expected that the bubble velocity will differ in water stream, since the water velocity affects the bubble rise velocity. To investigate this effect, a series of experimental runs were conducted and the bubble rise velocities have been measured in various water streams by using image processing techniques.

The relative bubble velocities obtained for various flow rates (2.15, 11, 21, 25 cm/s) differ from the so-called terminal velocity of bubbles rising in stagnant water. Figure 6.13 and Figure 6.14 show the variation of individual bubble velocities and relative bubble velocities respectively, as a function of the area equivalent bubble diameter.

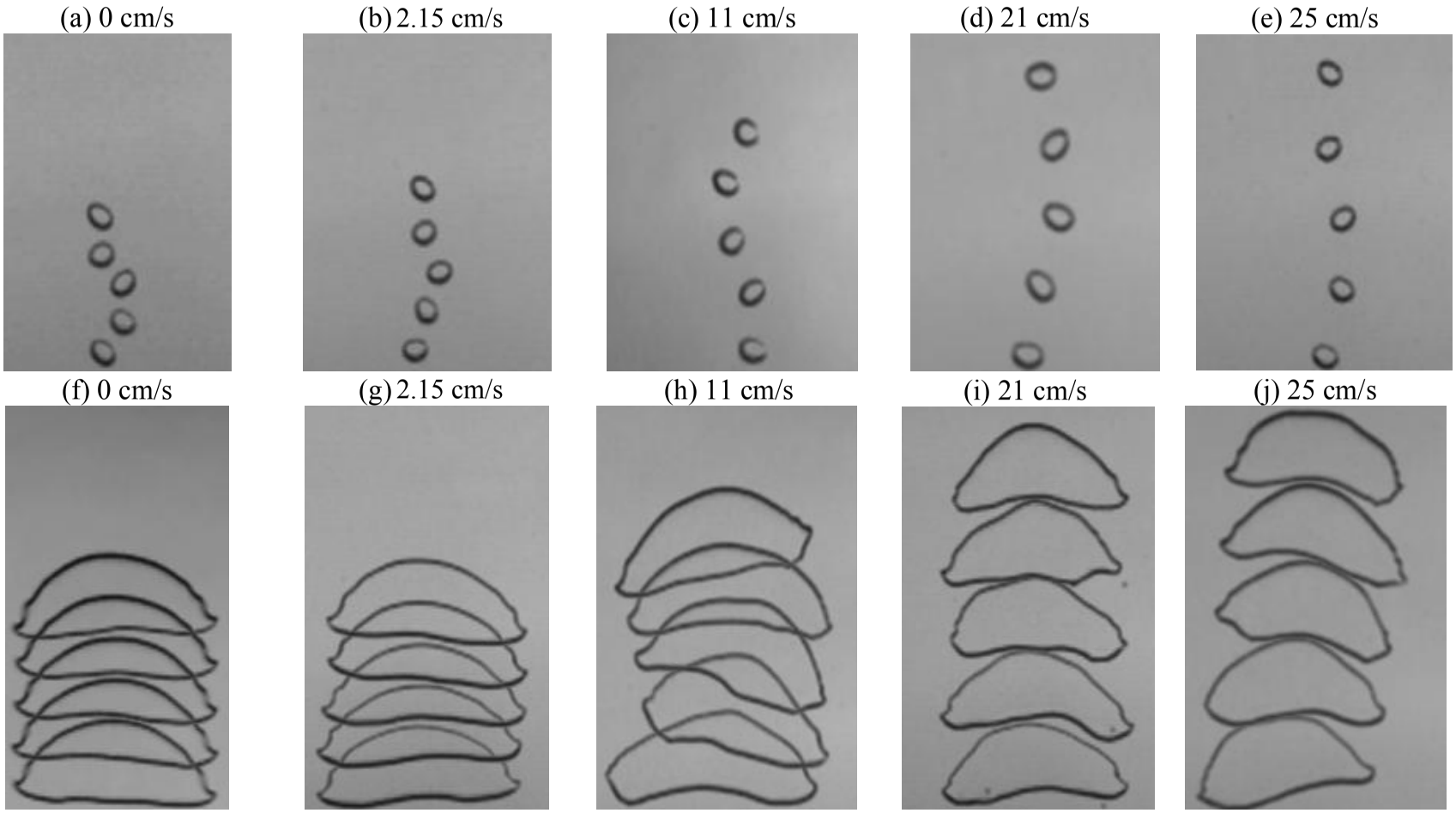

Figure 6.5 Comparison of ellipse bubbles and cap bubbles in stagnant water and in water stream of various flow rates

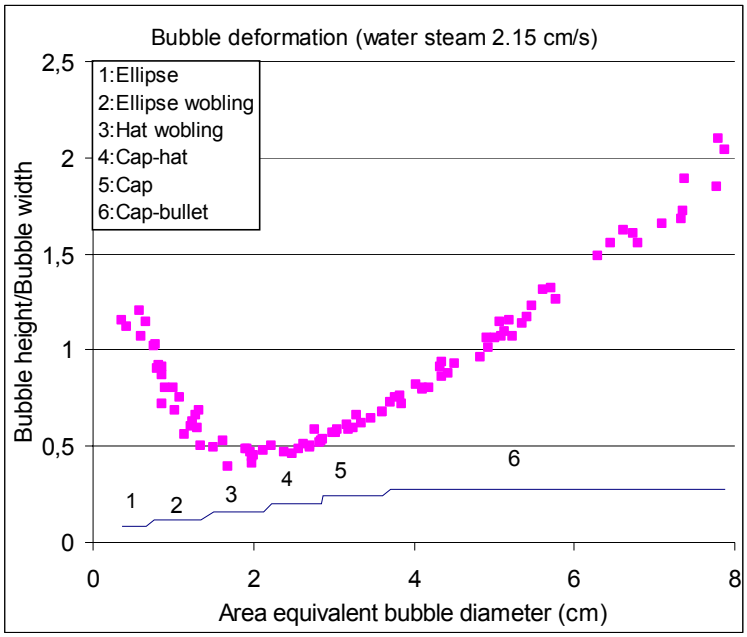

Figure 6.6 Bubble deformation and bubble shape classification versus area equivalent bubble diameter in 2.15 cm/s water stream

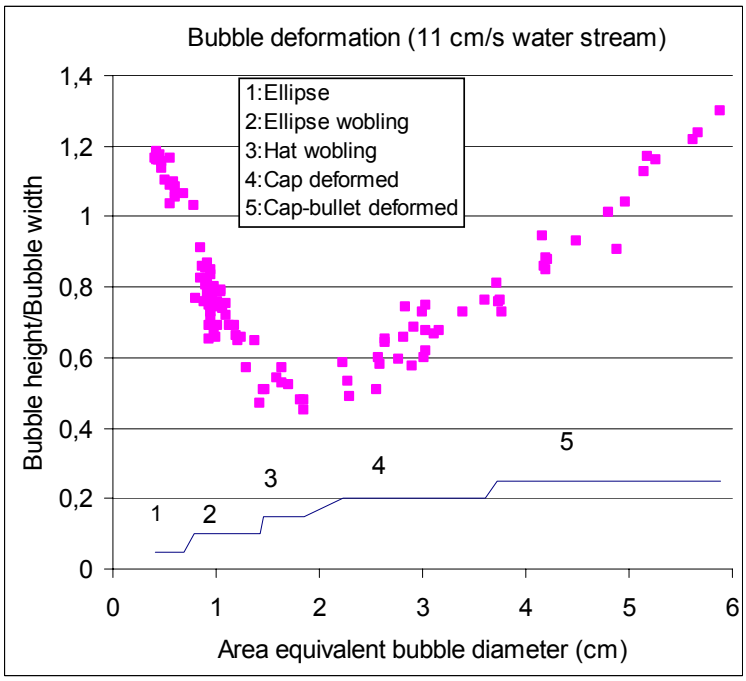

Figure 6.7 Bubble deformation and bubble shape classification versus area equivalent bubble diameter in 11 cm/s water stream

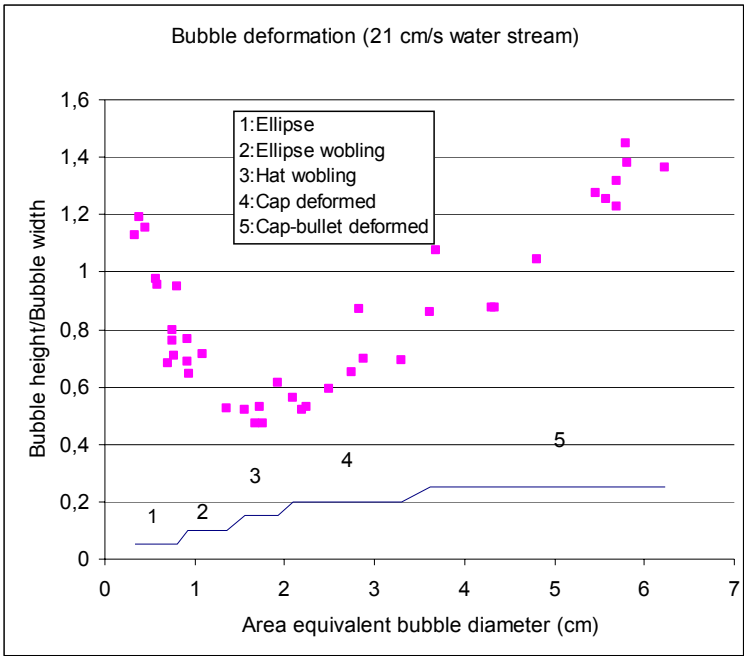

Figure 6.8 Bubble deformation and bubble shape classification versus area equivalent bubble diameter in 21 cm/s water stream

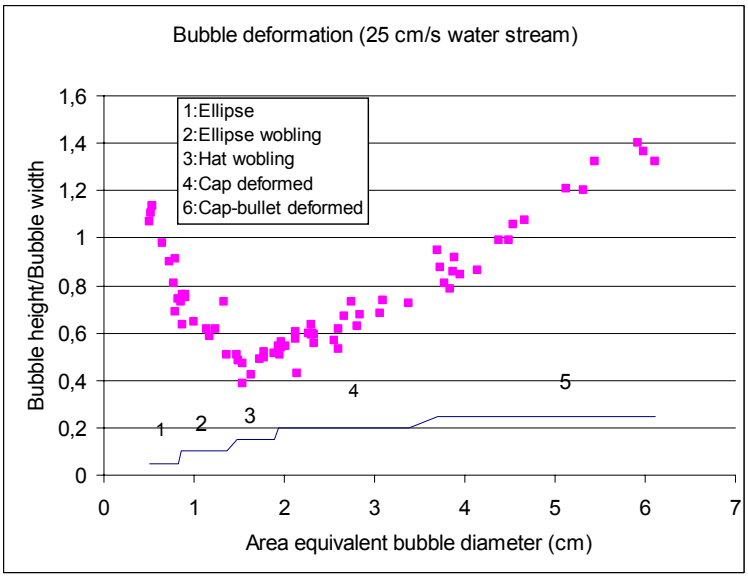

Figure 6.9 Bubble deformation and bubble shape classification versus area equivalent bubble diameter in 25 cm/s water stream

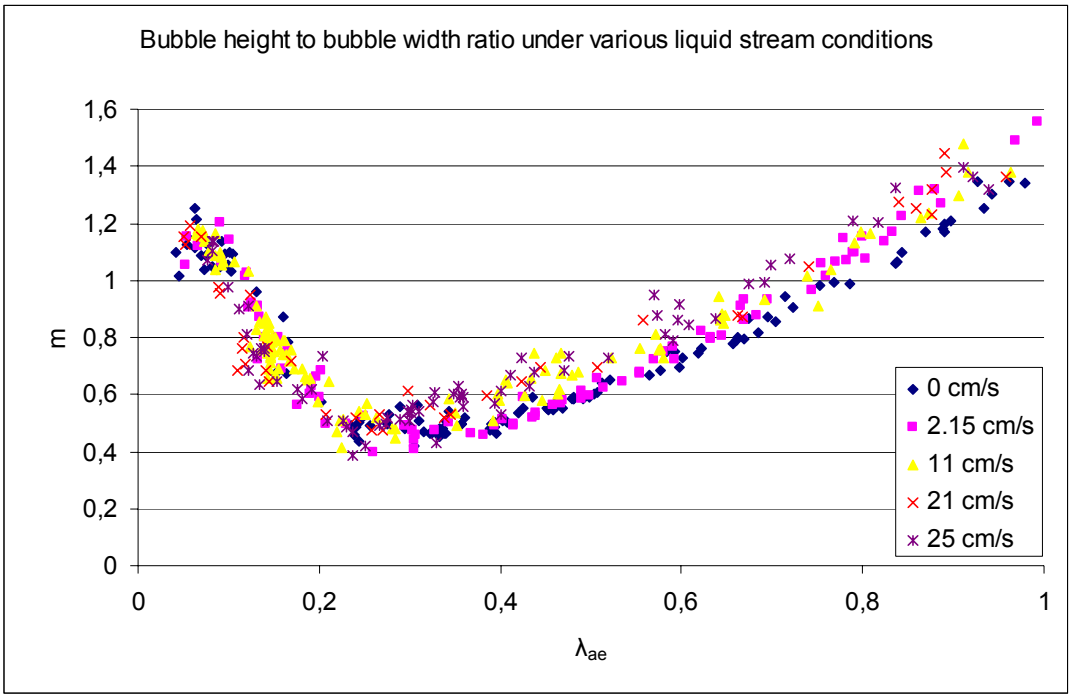

Figure 6.10 Variation of bubble deformation with area equivalent bubble diameter

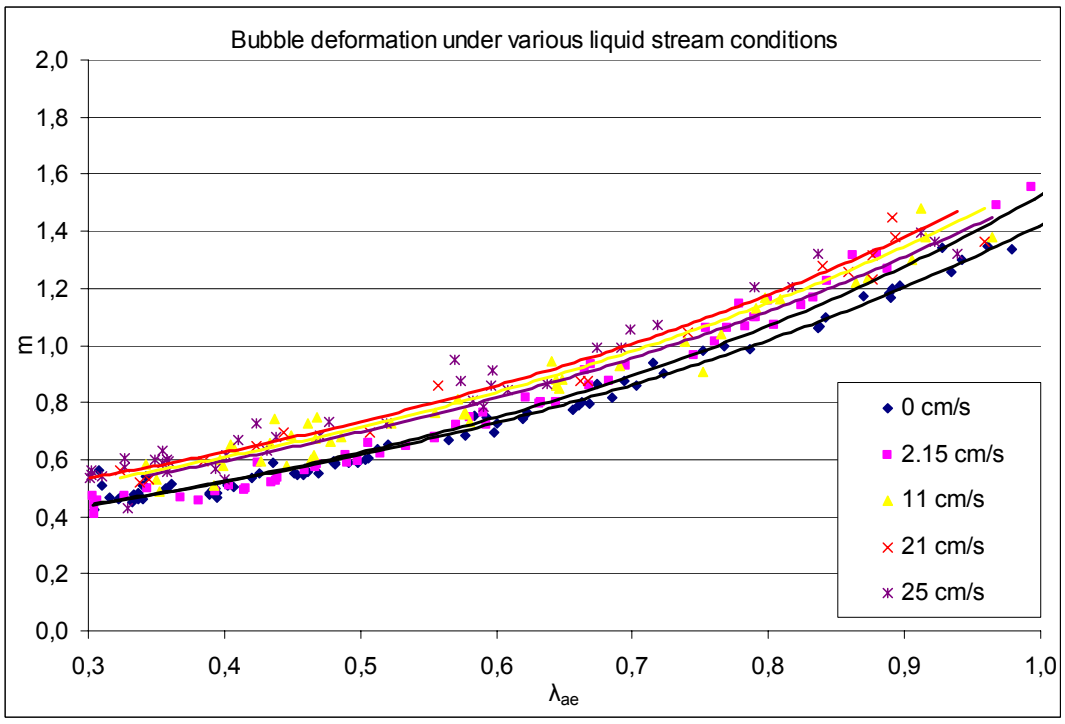

Figure 6.11 Deformation of cap bubbles for various water flow rates

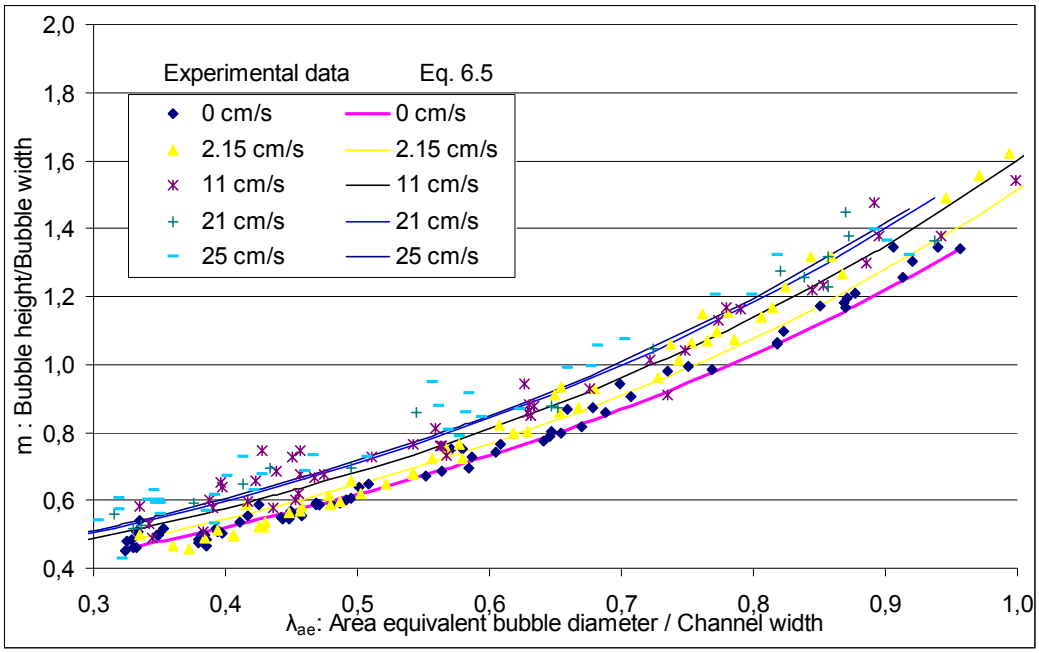

Figure 6.12 Comparison of experimental data with the correlation (Eq. 6.5)

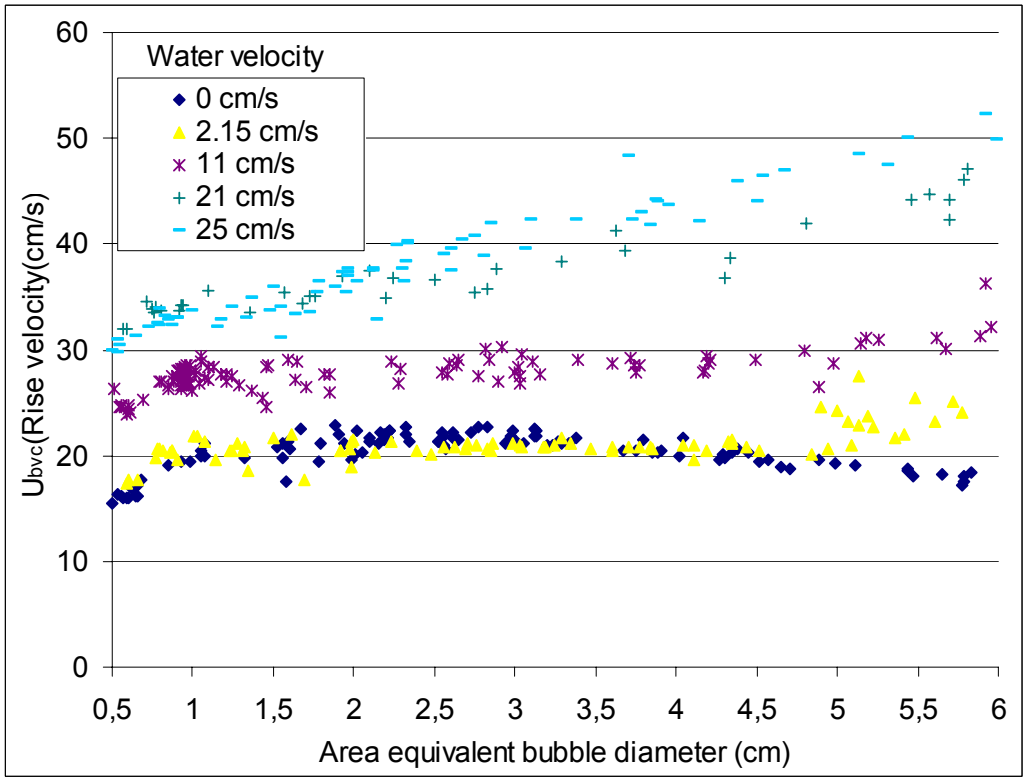

Figure 6.13 Bubble rise velocities in various water streams

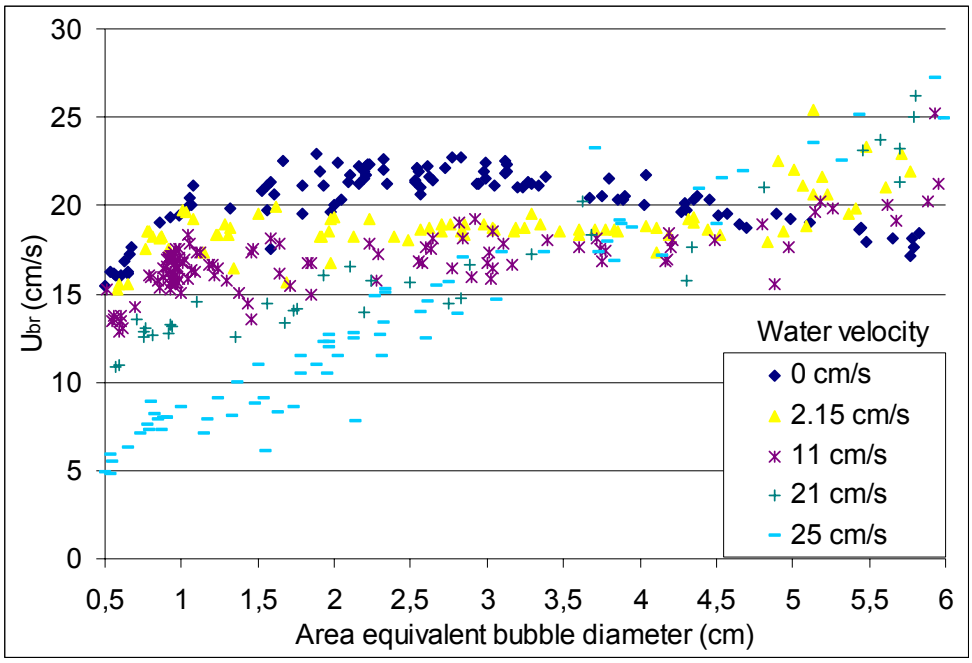

Figure 6.14 Bubble relative rise velocities in various water streams

There are two important points that can be concluded from these experimental results. First, the bubble relative velocity under co-current flow conditions for λ_{ae} <0.6 is less than that under stagnant water condition. Next, after bubble shapes reach to the slug type (λ_{ae} = 0.6), relative bubble velocities pass over the terminal bubble velocities in stagnant water. If the water velocity is increased further, the bubble relative velocity increases in the slug bubble region (see Figure 6.14).

Figure 6.15, Figure 6.16, Figure 6.17, and Figure 6.18 show the bubble rise velocity with bubble shape classification information for 5 < d_{ae} < 70 mm. under different co-current flowing water conditions (U_l = 0, 2.15, 11 21 and 25 cm/s).

6.3.1 Slug bubbles

As for the rise velocity U_b of a single slug bubble in a pipe flow, Nicklin and Collins *et al.* suggested that U_b can be expressed by

$$U_b = C\overline{U}_l + U_T \tag{6.6}$$

where U_l is the mean liquid velocity and C is a constant which is about 1.2 for a turbulent flow condition and about 1.9 for a laminar flow condition [75]. To the best of author's knowledge, there is not any study about the movement of individual bubble under liquid stream in narrow rectangular channels and no correlation for bubble velocity under these conditions is available in literature.

Rising velocities of slug bubbles under the conditions of $0.6 < \lambda_{ae} < 1.0$ were therefore analyzed in the air-water system to obtain correlations for slug bubble rise velocity. Figure 6.19 and Figure 6.20 show the results of slug bubble rise velocities and slug bubble relative rise velocities where $\lambda > 0.6$ ($d_{ae} > 40$ mm) in the channel for various liquid stream conditions.

To obtain a reasonable correlation for slug air bubbles in water stream, the measured bubble rise velocities U_b, were correlated using the following form of equation;

$$U_b = \left[CU_l + U_{bo}\right] f(\lambda) \tag{6.7}$$

where U_l is the mean velocity of the liquid phase, C is a constant and U_{b0} is the bubble rise velocity in stagnant water. $f(\lambda)$ is used to define the shape factor in the narrow channel because the slug velocities in the narrow channel are a function of λ_{ae}, not constant as the circular pipes. The values of C and $f(\lambda_{ae})$ were adjusted so as to yield the best correlation with the measured U_b. The slug bubble velocities in stagnant water were assumed constant and obtained by taking the average of all values. As a result, it could be confirmed that the following equation is an applicable correlation for slug air bubbles rising in water stream through vertical narrow channels under for $0.6 < \lambda < 1$ and $U_l \leq 25$ cm/s;

$$U_b = \left[0.92U_l + 19.67\right] \cdot \left[\lambda + 0.3\right] \tag{6.8}$$

Figure 6.21 shows the comparison of experimental data with the suggested correlation.

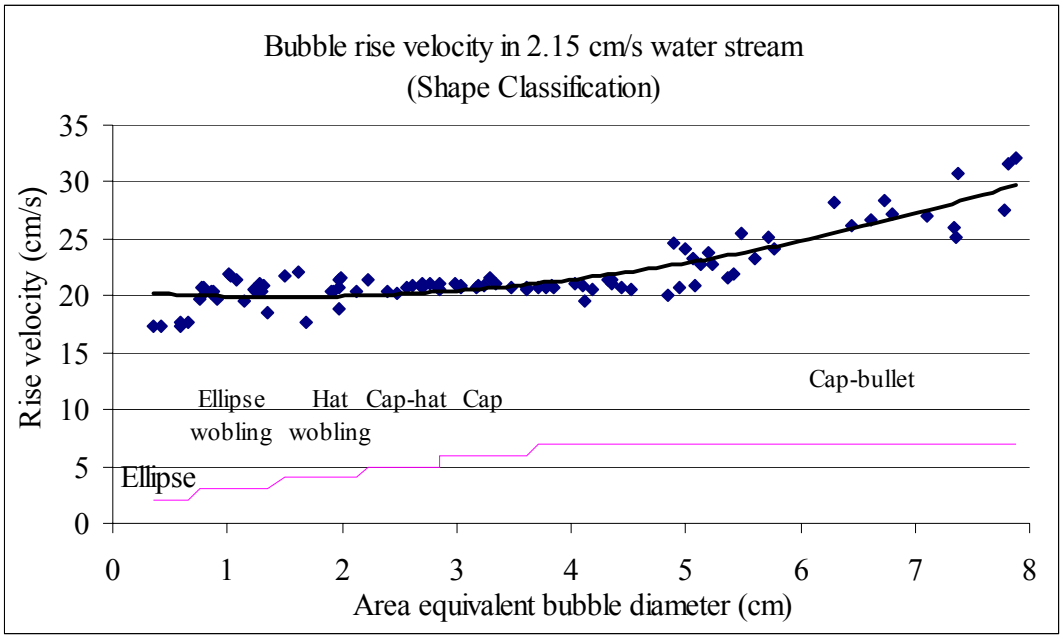

Figure 6.15 Bubble rise velocity and shape classification in 2.15 cm/s water stream through the vertical narrow rectangular channel

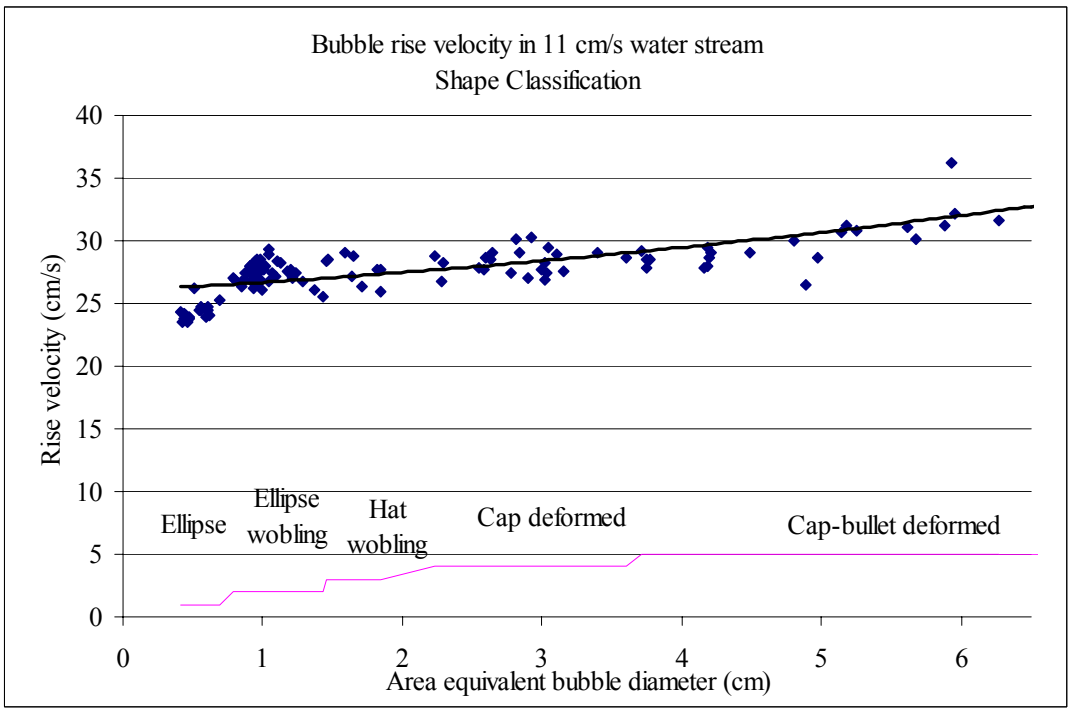

Figure 6.16 Bubble rise velocity and shape classification in 11 cm/s water stream through the vertical narrow rectangular channel

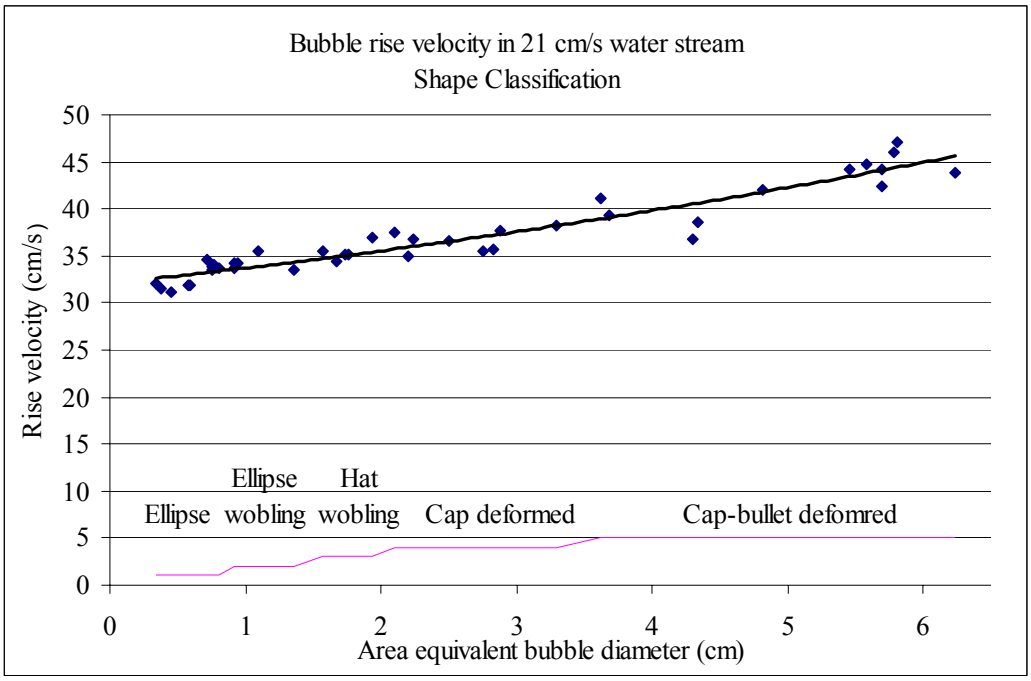

Figure 6.17 Bubble rise velocity and shape classification in 21 cm/s water stream through the vertical narrow rectangular channel

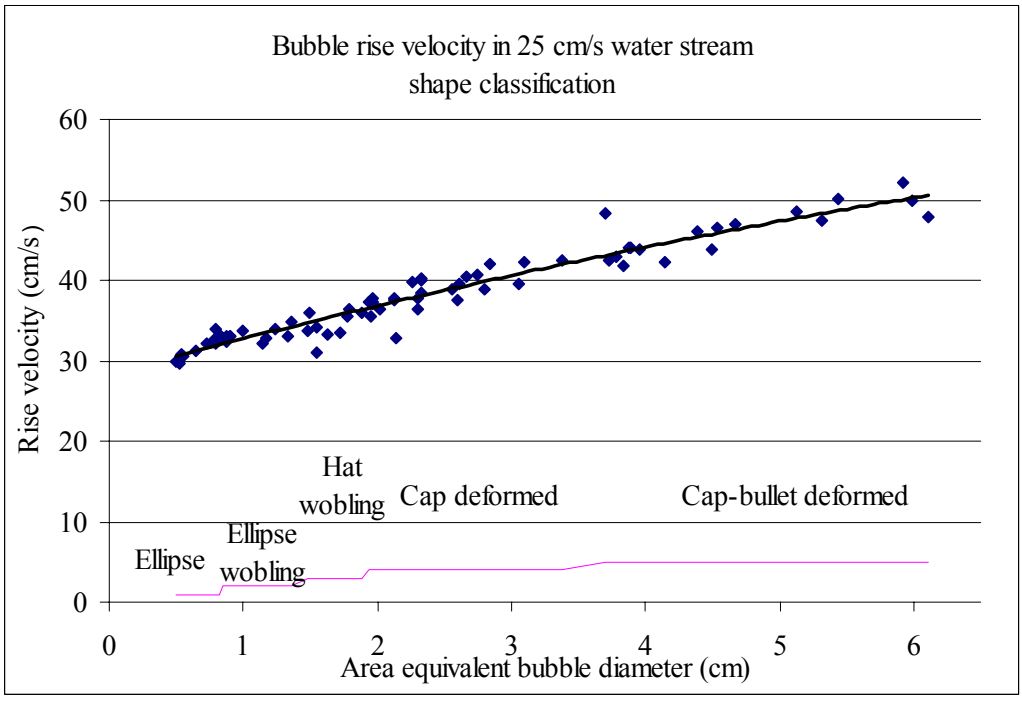

Figure 6.18 Bubble rise velocity and shape classification in 25 cm/s water stream through the vertical narrow rectangular channel

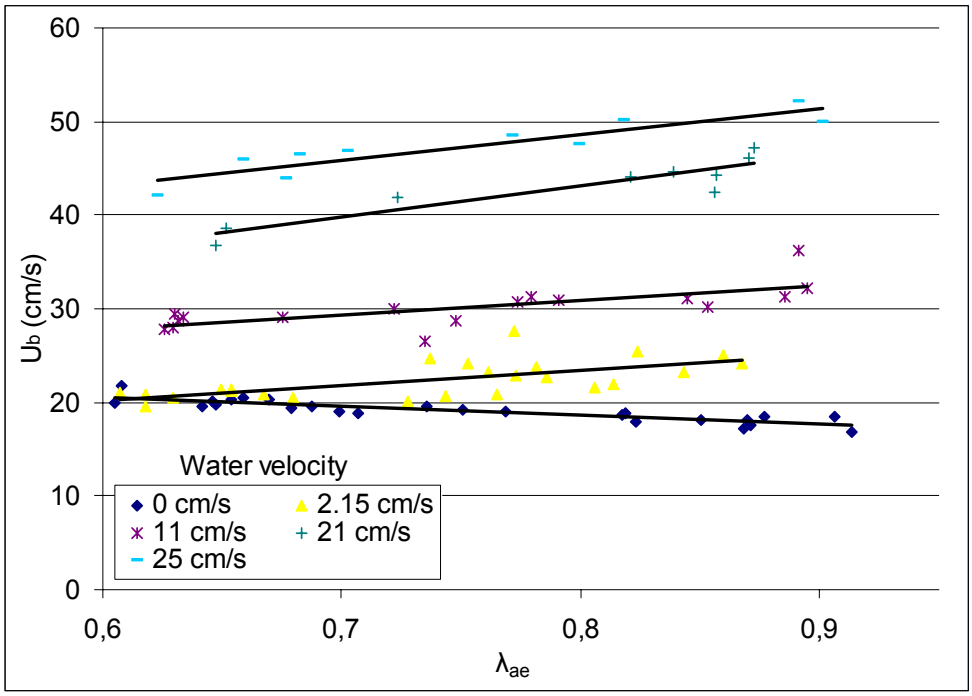

Figure 6.19 Slug bubble rise velocities in various water streams

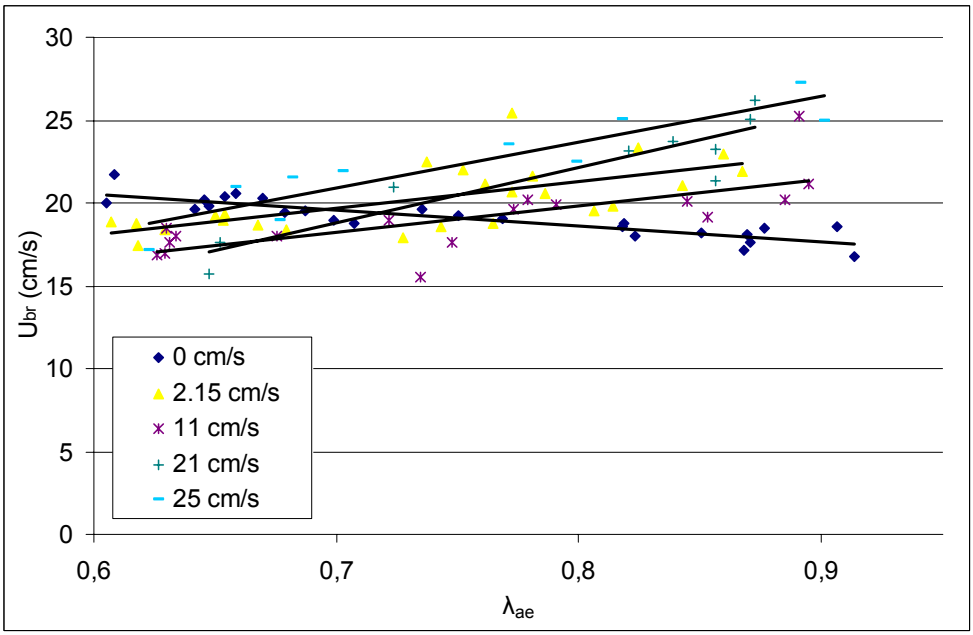

Figure 6.20 Slug bubble relative rise velocities in various water streams

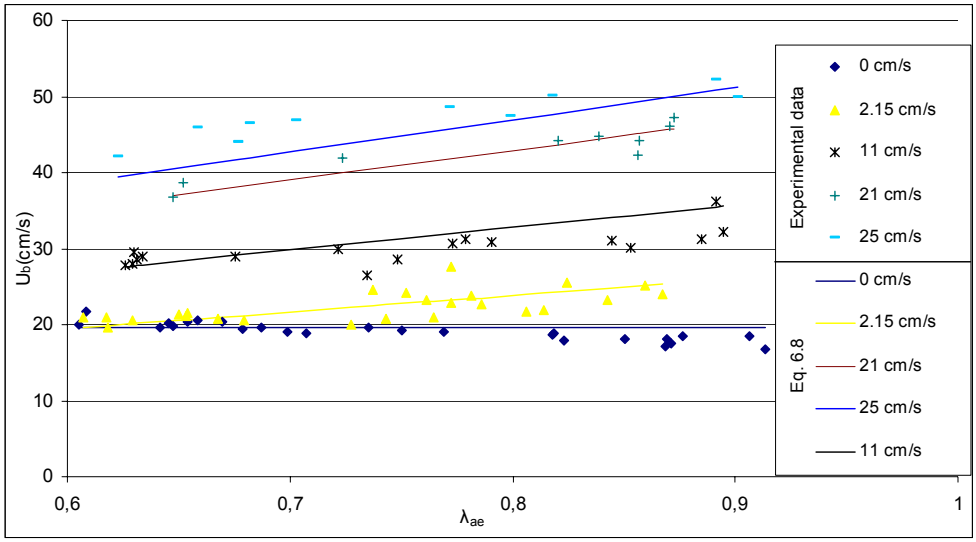

Figure 6.21 Comparison of slug bubble rise velocities with Eq. 6.8

CHAPTER 7

CONCLUSIONS AND SUGGESTIONS

This thesis presents the study of air bubble motion in stagnant water and in flowing water through a vertical narrow rectangular channel of 2.1X66.5 mm cross section by using image processing and analyzing techniques. The investigated bubble size range is 2 - 70 mm in area equivalent bubble diameter and mean water flow velocity is 0-25 cm/s.

7.1 Contributions of this study

The bubble generation technique used in the present experimental study is shown to have several advantages, e.g. the accuracy of the bubble size, repeatability of tests, and controlling the time between consecutive bubbles. The latter ensures that bubbles are not affected by preceding bubbles.

A set of tests were prepared and realized to obtain bubble shapes, paths and rise velocities at 21^{o}C stagnant water in the test section. In this set of tests, bubbles with area equivalent diameter range of 2 mm to 70 mm were analyzed extensively.

Bubble types, area and volume equivalent bubble diameters and bubble paths were obtained. The results are given in terms of Reynolds, Eötvös and Weber Numbers based on the area and volume equivalent bubble diameters to be able to compare them with the existing literature.

Observed bubble shapes consist of circular, ellipse, ellipse wobbling, hat wobbling, cap-hat, cap and cap-bullet types. Ellipse wobbling and hat wobbling type bubble regions show the transition from ellipse to cap region. Rise velocities in the transition region are scattered.

According to the results of tests in stagnant water, the paths of the bubbles can be categorized as follows;

a. Bubbles having d_{ae}< 2.7 (d_{ve} < 2.6) mm move on a rectilinear path if the *Re* based on U_{bvc} and d_{ae} is less than 579. In this range Reynolds number based on U_{bvc} and d_{ve} is less than 527 and bubble shapes are circular in 2D. For 3D case d_{ve} < 1.3 mm is generally acceptable condition for spherical bubbles [22].

b. If the Reynolds number based on U_{bvc} and d_{ae} is greater than 579 and less than 3170 the bubbles are ellipse in shape and move on a sinusoidal path.

c. For 15.3 mm < d_{ae}< 20.9 mm, bubbles move on an unstable sinusoidal or rectilinear irregular path with ellipse wobbling or hat wobbling shape. In this range, Reynolds number based on U_{bvc} and d_{ae} is greater than 3170 and less than 4454.

d. Bubbles rise in rectilinear motion for d_{ae} > 20.9 mm (d_{ve} > 10.8 mm). In this range bubble shapes are in cap type. For 3D case, this criterion is accepted as d_{ve} > 17 mm [22].

Ellipse bubbles rising in stagnant water through the channel were analyzed in detail. The range of ellipse bubbles is 0.27 mm < d_{ae} < 0.85 mm without wobbling and 0.85 mm < d_{ae} < 1.53 mm with wobbling. The results of the ellipse bubble tests and the correlation of rise velocity of ellipsoidal bubbles in 3D infinite medium were compared. An empirical correlation for 2D ellipse bubbles was obtained from the experimental data;

$$U_b = \left[0.5\frac{\sigma}{\rho d_{ae}} + 2.76 g d_{ae} \right]^{1/2} \tag{7.1}$$

This equation can be used for ellipse air bubbles rising in a vertical narrow channel of 2.1 mm gap size under stagnant water condition at 21 ^{o}C temperature when side wall effects are insignificant.

The cap bubble rise velocities measured in this study were compared with the correlations in literature and because of the discrepancy in results, a new empirical correlation for cap bubble rise velocities for a vertical narrow channel was obtained.

Two ways were followed to obtain cap bubble rise velocity correlation. First, experimental data were correlated parallel to the correlation of Grace and Harrison [44] using the bubble deformation information to add the side wall effects to the equation implicitly. The obtained correlation is as follows;

$$U_b = 0.28m^{-0.73}(g)^{\frac{1}{2}}(A)^{\frac{1}{4}} \tag{7.2}$$

or

$$U_b = 0.624e^{-0.77m}(g)^{\frac{1}{2}}A^{1/4} \tag{7.3}$$

The second way was to introduce wall effects multiplier to the 2D infinite medium correlations. The result of this approach is as follows;

$$\frac{U_b}{U_\infty} = 1.31e^{-1.29\lambda_{ae}} \tag{7.4}$$

The experimental results of air bubbles rising in water stream with a velocity range of 0 cm/s < U_l < 25 cm/s is as follows:

The shape of the bubbles is nearly ellipse if d_{ae} < 15 mm. For d_{ae} > 15 mm, the bubbles tend toward the cap type although there is large oscillation in the major dimensions when the liquid velocity increases.

Observations of ellipse bubble shape in flowing water are in a good consistency with the observations in stagnant water. The observed shapes of paths were sinusoidal in both stagnant water and flowing water case. The only difference is in the period of the bubble paths. The periods of the bubble paths increase when the liquid velocity increases. On the other hand, cap bubbles are much more deformed when the liquid velocity increases and shape oscillations are more effective in flowing water than in stagnant water condition.

Bubble deformation, which is defined as bubble height to bubble width ratio, increases in cap-bubble region where $\lambda_{ae} \geq 0.3$ for 2.15, 11, 21, and 25 cm/s water velocities. The trends of the cap bubble deformation for various water streams are almost similar in behavior. To obtain a reasonable correlation for cap bubble deformation in water stream, the measured values were correlated by using the following equation;

$$m = \left[0.264 + 0.0085 U_l^{1/2} \right] e^{1.7 \lambda_{ae}} \tag{7.5}$$

The rise velocity of air bubbles in water stream was analyzed extensively. The water bulk velocity ranges from 0 cm/s to 25 cm/s, corresponding to a system Reynolds number range of 0 to 1015. Air bubble size ranges from 5 mm to 70 mm in area equivalent diameter and corresponding bubble Reynolds number based on bubble relative velocity and d_{ae} varies from 250 to 16000.

The bubble rise velocities with bubble classification information were obtained for different co-current water flow conditions (U_l = 0, 2.15, 11 21 and 25 cm/s) in the range of $5 < d_{ae} < 70$ mm.

There are two important points that can be concluded from the experimental results. First, the bubble relative velocity under co-current flow condition for λ_{ae} <0.6 is less than that under stagnant water condition. Second, after bubble shape reaches to the slug type ($\lambda_{ae} \geq 0.6$), relative bubble velocities pass over the terminal bubble velocities in stagnant water. If the water velocity is increased further, the bubble relative velocity increases in the slug bubble region.

Rising velocities of slug bubbles of $0.6 < \lambda_{ae} < 1.0$ were analyzed to obtain a correlation for vertical narrow rectangular channels. It may be suggested that the following correlation is an applicable equation for slug bubble rising velocity in vertical narrow channels through flowing water in the range of $0.6 < \lambda < 1$ and $U_l \leq$ 25 cm/s;

$$U_b = \left[0.92 U_l + 19.67 \right] \cdot \left[\lambda + 0.3 \right] \tag{7.6}$$

7.2 Suggestions for future work

This study might be extended to cover a large range of geometric dimensions (changing the channel gap size and channel width) and operating parameters (changing pressure and temperature of water) for narrow rectangular channels. The study might also be extended to higher liquid velocities by using high-speed high-resolution digital video camera to investigate the bubble axial and vertical velocities more precisely.

The other subject might be the visualization of the wake structure behind the air bubbles possibly with PIV method having different shape for the stagnant, co-current and counter-current water streams to understand the reason of the bubble rise velocity differences among those cases.

REFERENCES

1. Q. Bi, *"Characteristics of Two-Phase Flow and Boiling Heat Transfer in Miniature Non-Circular Channels"*, Ph.D. Thesis, The Hong Kong University of Science & Technology, 2000

2. A.N. Pavlenko, N.I. Pecherkin, V.Y. Chekhovich, V.E. Zhukov, S. Sunder, P. Houghton, A.F. Serov and A.D. Nazarov, *"The Two-Phase Downflow of Liquid Nitrogen in a Vertical Rectangular Channel",* Actual Problems of Aviation and Aerospace Systems: Processes, Models, Experiment, Russian-American Journal, Kazan, Vol. 2 (18), 2004

3. A. Tomiyama, I. Zun, A. Sou, T. Sakaguchi, *"Numerical Analysis of Bubble Motion with the VOF Method"*, Nuclear Engineering and Design 141, pp. 69-82, 1993

4. D. Qian, *"Bubble Motion, Deformation, and Breakup in Stirred Tanks"*, Ph.D. Thesis, Clarkson University, January, 2003

5. D.R. Todd, *"Methodologies for Analyzing PIV and SIV Results from a Two-Phase Air/Water Experiment"*, Ph.D. Thesis, Texas A&M University, 2002

6. H. Rusche, *"CFD of Dispersed Two-Phase Flows at High Phase Fractions"*, Ph.D. Thesis, Imperial College of Science, Technology & Medicine, December 2002

7. S.V. Paras, A.G. Kanaris, A.A. Mouza, A.J. Karabelas, *"CFD Code Application to Flow through Narrow Channels with Corrugated Walls"* CHISA 2002, 15th International Congress of Chemical and Process Engineering, Prague, August 2002

8. P. Daripa, *"A Computational Study of Rising Plane Taylor Bubbles"*, Journal of Computational Physics 157, pp. 120-142, 2000

9. Z.L. Yang, B. Palm, B.R. Sehgal, *"Numerical Simulation of Bubbly Two-Phase Flow in a Narrow Channel"*, International Journal of Heat and Mass Transfer 45, pp. 631-639, 2002

10. D. Lörstad, L. Fuchs, *"High-Order Surface Tension VOF-Model for 3D Bubble Flows with High Density Ratio"* Journal of Computational Physics, pp. 153-176, 2004

11. B. Bunner, G. Tryggvason, *"Simulation of Large Bubble Systems"*, ASME Fluids Engineering Division Summer Meeting, Report no: FEDSM97-3409, 1997

12. T. Willmarth, M. Ishii, *"Two Phase Flow Regimes in Narrow Rectangular Vertical and Horizontal Channels"*, International Journal of Heat and Mass Transfer, Vol.37, pp. 1749-1758, August 1994

13. P.F. Vassallo, R. Kumar, *"Liquid and Gas Velocity Measurements Using LDV in Air-Water Duct Flow"*, Experimental Thermal and Fluid Science 19, pp. 85-92, 1999

14. V. Hengel, *"Multi-Level Modelling of Gas-Liquid Two-Phase Flow in a Bubble Column"*, Ph.D. Thesis, University of Twente, Enschede, 2004

15. T. Hibiki, K. Mishima, *"Flow Regime Transition Criteria for Upward Two-Phase Flow in Vertical Narrow Rectangular Channels"*, Nuclear Engineering and Design 203, pp. 117-131, 2001

16. I. Zun, J. Groselj, *"The Structure of Bubble Non-Equilibrium Movement in Free-Rise and Agitated-Rise Conditions"*, Nuclear Engineering and Design 163, pp. 99-115, 1996

17. K.Mishima, T. Hibiki, H. Nishihara, *"Some Characteristics of Gas-Liquid Flow in Narrow Rectangular Ducts",* Int. J. Multiphase Flow, Vol. 19, pp. 115-124, 1993

18. IAEA, "Research Reactor Core Conversion from the Use of Highly Enriched Uranium to the Use of Low Enriched Uranium Fuels Guidebook", IAEA-TECDOC-233, Vienna, 1980

19. L.S. Tong, J. Weisman, "Thermal Analysis of Pressurized water reactors", The American Nuclear Society, Illinois, USA, 1979

20. I.S. Lioumbas, A.A. Mouza, S.V. Paras, *"Local Velocities Inside the Gas Phase During Counter-Current Two-Phase Flow in a Narrow Vertical Channel"*, Trans. IChemE, Vol 80, Part A, pp. 667-673, September 2002

21. R. Krishna, M.I. Urseanu, J.M. van Baten, J. Ellenberger, *"Wall Effects on the Rise of Single Gas Bubbles in Liquids"*, Int. Comm. Heat and Mass Transfer, Vol. 26, pp. 781-790, 1999

22. R. Clift, J.R. Grace, M. E. Weber, *"Bubbles, Drops, and Particles"*, Academic Press, London, 1978

23. A.W.G. de Vries, *"Path and Wake of a Rising Bubble"*, Ph.D. Thesis, University of Twente, 2001

24. E.T. White, R.H. Beardmore, *"The Velocity of Rise of Single Cylindrical Air Bubbles through Liquids Contained in Vertical Tubes"*, Chemical Engineering Science, Vol. 17, pp. 351-361, 1962

25. G.P. Celata, M. Cumo, F. D'Annibale, A. Tomiyama, *"Bubble Rising Velocity in Saturated Liquid up to Critical Pressure"*, Experimental Heat Transfer, Fluid Mechanics, and Thermodynamics, pp. 1319-1328, 2001

26. A. Tapucu, *"Durgun Sıvılar İçinde Yükselen Gaz Habbelerinin Hareketlerinin Etüdü"*, Ph.D. Thesis, İTÜ- Faculty of Mechanical Engineering, 1968

27. N.M. Aybers, H. Yavuz, *" The Motion of Gas Bubbles Rising through Moving Liquid"*, İTÜ INER Bulletin, No.23, 1976

28. Bezdegümeli U., *"Investigation of Air Bubble Motion in Counter-Current Water Flow Conditions"*, Ph.D. Thesis, Middle East Technical University, Ankara, September 2003

29. J.L. Xu, P. Cheng, T.S. Zhao, *"Gas-Liquid Two-Phase Flow Regimes in Rectangular Channels with Mini/Micro Gaps"*, International Journal of Multiphase Flow 25, pp. 411-432, 1999

30. K. Mishima, S. Fujine, K. Yoneda, K. Yonebayashi, K. Kanda, H. Nishihara, *"A Study of Air-Water Flow in a Narrow Rectangular Duct Using an Image Processing Technique"*, Dynamics of Two Phase Flows, Edited by Oven C. Jones and Itoru Michiyashi, Japan, 141-159

31. J.W. Coleman, S. Garimella, *"Characterization of Two Phase Flow Patterns in Small Diameter Round and Rectangular Tubes"*, International Journal of Heat and Mass Transfer 42, pp. 2869-2881, 1999

32. K.A. Triplett, S.M. Ghiaasiaan, S.I. Abdel-Khalik, D.L. Sadowski, *"Gas-Liquid Two-Phase Flow in Microchannels Part I: Two-Phase Flow Patterns"*, International Journal of Multiphase Flow 25, pp. 377-394, 1999

33. J. Bonjour, M. Lallemand, *"Flow Patterns During Boiling in a Narrow Space between Two Vertical Surfaces"*, International Journal of Multiphase Flow 24, pp. 947-960, 1998

34. T. Hibiki, K. Mishima, H. Nishihara, T. Motomura, *"Study on Air-Water Two-Phase Flow in a Small Diameter Tube"*, Annual Reports of the Reactor Institute, Kyoto University, Vol.26, pp. 34-44, 1993

35. K. Mishima, H. Nishihara, *"The Effect of Flow Direction and Magnitude on CHF for Low Pressure Water in Thin Rectangular Channels"*, Nuclear Engineering and Design, 86, pp. 165-181, 1985

36. M. Sadatomi, Y. Sato, S. Saruwatari, *"Two-Phase Flow in Vertical Noncircular Channels"*, Int. J. Multiphase Flow Vol. 8, pp. 641-655, 1982

37. P. Spicka, A. A. Martins, M. M. Dias, J. C. B. Lopes, *"Hydrodynamics of Gas-Liquid Flow in 2D Packed/Unpacked Rectangular Reactor"*, Chemical Engineering Science 54, pp. 5127-5137, 1999

38. T.S. Zhao, Q.C. Bi, *"Co-Current Air-Water Two-Phase Flow Patterns in Vertical Triangular Microchannels"*, International Journal of Multiphase Flows 27, pp. 765-782, 2001

39. J. Xu, *"Experimental Study on Gas-Liquid Two-Phase Flow Regimes in Rectangular Channels with Mini Gaps"*, International Journal of Heat and Fluid Flow 20, pp. 422-428, 1999

40. N.A. Vlachos, S.V. Paras, A.A. Mouza, A.J. Karabelas, *"Visual Observations of Flooding in Narrow Rectangular Channels"*, International Journal of Multiphase Flow 27, pp. 1415-1430, 2001

41. M. Kureta, T. Hibiki, K. Mishima, H. Akimoto, *"Study on Point of Net Vapor Generation by Neutron Radiography in Subcooled Boiling Flow along Narrow Rectangular Channels with Short Heated Length"*, International Journal of Heat and Mass Transfer 46, pp. 1171-1181, 2003

42. J.R. Grace, D. Harrison *"The Influence of Bubble Shape on the Rising Velocities of Large Bubbles"*, Chemical Engineering Science, Vol. 22, pp. 1337-1347, 1967

43. K. Tsuchiya, L. Fan, *"Near-Wake Structure of a Single Gas Bubble in a Two-Dimensional Liquid-Solid Fluidized Bed: Vortex Shedding and Wake Size Variation"*, Chemical Engineering Science, Vol. 43, pp. 1167-1181, 1988

44. S.S. Sadhal, P.S. Ayyaswamy, J.N. Chung, *"Transport Phenomena with Drops and Bubbles"*, Springer, 1996

45. D.W.T. Rippin, J.F. Davidson, *"Free Streamline Theory for a Large Gas Bubble in a Liquid"* Chemical Engineering Science, Vol. 22, pp. 217-228, 1967

46. Q. Liao, T.S. Zhao, *"Modeling of Taylor Bubble Rising in a Vertical Mini Noncircular Channel Filled with a Stagnant Liquid"*, International Journal of Multiphase Flow 29, pp. 411-434, 2003

47. S. Polonsky, D. Barnea, L. Shemer, *"Averaged and Time-Dependent Characteristics of the Motion of an Elongated Bubble in a Vertical Pipe"*, International Journal of Multiphase Flow 25, pp. 795-812, 1999

48. G. Das, P.K. Das, N.K. Purohit, A.K. Mitra, *"Rise Velocity of a Taylor Bubble through Concentric Annulus"*, Chemical Engineering Science, Vol. 53, No. 5, pp. 977-993, 1998

49. J.K. Walters, J.F. Davidson, *"The Initial Motion of a Gas Bubble Formed in an Inviscid Liquid Part 1. The Two-Dimensional Bubble"*, J. Fluid Mech. 12, pp. 408-416, 1962

50. H. Yavuz, *"Tabii Sirkulasyonlu Kaynar Sulu Reaktörlerde Buhar Habbelerinin Aşağı Sürüklenmesinin Etüdü"*, Ph.D. Thesis, İTÜ- Faculty of Mechanical Engineering, 1970

51. J.L. Baker, B.T. Chao, *"An Experimental Investigation of Air Bubble Motion in a Turbulent Water Stream"*, A.I.Ch.E Journal, March, pp. 268-273, 1965

52. R.H.S. Winterton, J.S. Munaweera, *"Methods of Predicting Bubble Size in Bubbly Flow"*, Proceedings of the Second International Symposium on Two-Phase Flow Modelling and Experimentation, Pisa, ITALY, 23-26 May, 1999

53. H. Murakawa, Y. Suzuki, H. Kikura, M. Aritomi, *"Liquid Phase Flow Structure Around Bubble in Bubbly Co-current Flow"*, 4th International Conference on Multiphase Flow, ICMF-2001, New Orleans, USA, May 27-June 1, 2001

54. St. Körner, L. Friedel, *"Phase Distribution and Bubble Velocity in Two-Phase Slit Flow"*, International Journal of Multiphase Flow 25, pp. 1181-1194, 1999

55. R.H.S Winterton, J.S. Munaweera, *"Bubble Size in Two-Phase Gas–Liquid Bubbly Flow in Ducts"*, Chemical Engineering and Processing 40, pp. 437-447, 2001

56. N. Sadr-Kazemi, J.J. Cilliers, *"An Image Processing Algorithm for Measurement of Flotation Froth Bubble Size and Shape Distributions"*, Mineral Engineering, Vol. 10, pp. 1075-1083, 1997

57. B. Donevski, T. Saga, T. Kobayashi, S. Segawa, *"A Study of Bubble Dynamics in Subcooled Flow Boiling Using Image Processing Technique"*, Proceeding of the 4th World Conference on Experimental Heat Transfer, Fluid Mechanics and Thermodynamics, 1997

58. Uchimura, G.D. Harvel, T. Matsumoto, M. Kanzaki, J. Chang, *"An Image Processing Approach for Two-Phase Interfaces Visualized by a Real Time Neutron Radiography Technique"*, Flow Measurement and Instrumentation 9, pp. 203-210, 1998

59. P. Daripa, *"The Fastest Smooth Taylor Bubble"*, Applied Numerical Mathematics 34, pp. 373-379, 2000

60. S.G. Kandlikar, M.E. Steinke, S. Tian, L.A. Campbell , *"High-Speed Photographic Observation of Flow Boiling of Water in Parallel Mini-Channels"*, Proceedings of NHTC'01 35th National Heat Transfer Conference, California, June 10-12, 2001

61. M.W. Burke, *"Image Acquisition"*, Chapman&Hall, Meta Vision Atlanta, 1996

62. C.B. Lee, *"Radial Undistortion and Calibration on an Image Array"*, Master Thesis, Engineering in Electrical and Computer Science, Massachusetts Institute of Technology, 2000

63. P.E. Debevec, *"Modeling and Rendering Architecture from Photographs"*, Ph.D. Thesis, Computer Science, Graduate Division of the University of California, Berkeley, 1996

64. Virtualdub Software, *"Virtualdub.org"*, www.virtualdub.org, January, 2004

65. National Institute of Health, *"ImageJ"*, http://rsb.info.nih.gov/ij/, 17 November 2004

66. S. Sternberg, *"Biomedical Image Processing"*, IEEE Computer, January 1983

67. B. Rosenberg, *"The David W. Taylor Model Basin"*, Report No. 727, 1950

68. N.M. Aybers, *"Two Phase Flows and Heat Transfer"*, Vol. 1, Hemisphere, Washington, DC, 1977

69. R. Collins, *"A Simple Model of the Plane Gas Bubble in a Finite Liquid"*, J. Fluid Mech. Vol. 22, pp. 763-771, 1965

70. R. Collins, *"The Cycloidal-Cap Bubble: A Neglected Solution in the Theory of Large Plane Gas Bubbles in Liquids"*, Chemical Engineering Science, Vol. 22, pp. 89-97, 1967

71. J. Berghmans, *"Stability of Large Two-Dimensional Gas Bubbles"*, Chemical Engineering Science, Vol. 29, pp. 1645-1650, 1974

72. G.B. Wallis, *"One-Dimensional Two-Phase Flow"*, McGraw-Hill Book Company, 1969

73. R. Collins, *"A Second Approximation for the Velocity of a Large Gas Bubble Rising in an Infinite Liquid"* Journal of Fluid Mechanics, Vol. 25, pp. 469-480, 1966

74. R. Krishna, J.M. van Baten, M.I. Urseanu, J. Ellenberger, *"Rise Velocity of Single Circular-Cap Bubbles in Two Dimensional Beds of Powders and Liquids"*, Chemical Engineering and Processing 39, pp. 433-440, 2000

75. A. Tomiyama, Y. Nakahara, G. Morita, *"Rising Velocities and Shapes of Single Bubbles in Vertical Pipes"*, 4th International Conference on Multiphase Flow, ICMF-2001, New Orleans, USA, May 27-June 1, 2001

76. Z. Zhang, *"Flexible Camera Calibration by Viewing a Plane from Unknown Orientations"*, International Conference on Computer Vision (ICCV'99), Corfu, Greece, September 1999

77. J-Y. Bouguet, *"Camera Calibration Toolbox for MATLAB"*, www.vision.caltech.edu/bougetj/calib-doc/, MRL-Intel Corp., 1999

78. Z. Zhang, *"A Flexible New Technique for Camera Calibration"*, Technical Report, MSR-TR-98-71, Microsoft Research, Microsoft Corporation, 2002

79. Z. Zhang, *"Easycalib Software"*, Microsoft Corporation, ftp://ftp.research.microsoft.com/users/easycalib/EasyCalib.zip, 2002

APPENDIX A

CAMERA CALIBRATION

Calibration is an important step in any computer graphics application that uses lenses/cameras [62]. Lenses project a real world scene onto a flat image. This projection is different for each lens and it depends on many intrinsic values for the lens. Calibration is the process of finding these intrinsic values. Once these values are found, one could figure out how the pixels in the image correspond to points in the real world.

The first part of the calibration process is to determine an image coordinate remapping that causes images taken by the camera to be true perspective images [63]. The procedure makes use of one or several images with many known straight lines in it. The checkerboard pattern is a natural choice since straight lines with easily localized endpoints and interior points can be found in several orientations (horizontal, vertical, and various diagonals) throughout the image plane.

Video camera images deviate from actual views mostly because of lens distortion. Because of various constraints in the lens manufacturing process, straight lines in the world image through lenses generally become somewhat curved on the image plane. However, since each lens element is radially symmetric, and the elements are typically placed with high precision on the same optical axis, this distortion is almost always radially symmetric, and is referred to as radial lens distortion. Generally, a desktop camera usually exhibits significant lens distortion, especially radial distortion [76].

7.3 A.1. Camera calibration parameters

The list of variables in camera calibration is as follows;

Focal length: The focal lengths measure the distance between the image plane and the focal point (See Figure A.1).

Principal point: The principal point is the point that gets projected perpendicular to the image plane (See Figure A.2).

Skew coefficient: The skew indicates the degree to which the u and v axes are not perpendicular (See Figure A.1)

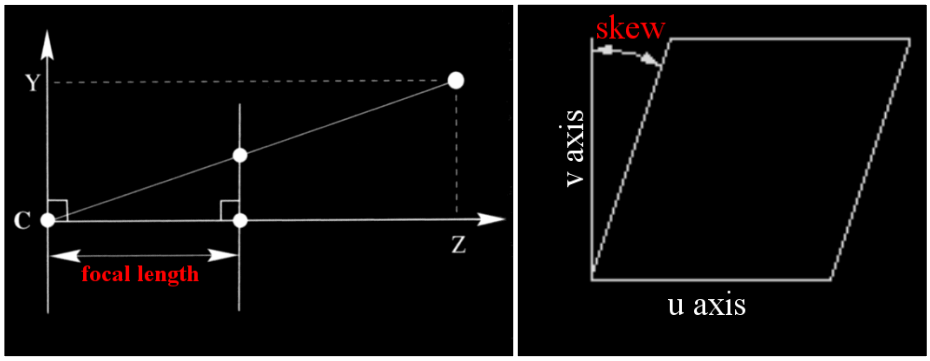

Figure A.1 Focal length and skew coefficient

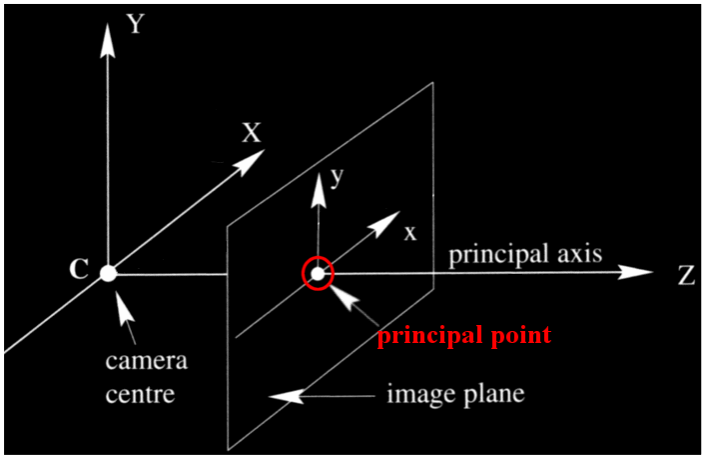

Figure A.2 Camera position and image plane

Once the distortion pattern of a lens is known, one can use any image taken with that lens, undistort it, and then has an image in which straight lines in the world project to straight lines in the image [63]. As a result, the projection is a true perspective projection, and it becomes possible to characterize the lens in terms of its intrinsic parameters.

It should be noted that most prime lenses actually change in focal length depending on the distance at which they are focused. This means that images taken with the same lens on the same camera may exhibit different focal lengths, and thus need separate camera calibrations. The easiest solution to this problem is to fix the focus of the lens at infinity and use a small enough aperture to image the closest objects in the scene in focus [63].

Zhang recently published a paper [78] describing a calibration method that is very easy to do and it only requires a software processing. This method needs at least two images of a planar pattern.

As it can be seen from Figure A.3, at least three calibration images are required in calibration process for reasonably good results [78].One of the questions arising in camera calibration process is at which angle camera calibration rig should be held to obtain better results. Zhang [78] suggests that 45^{o} is the right choice (See Figure A.4).

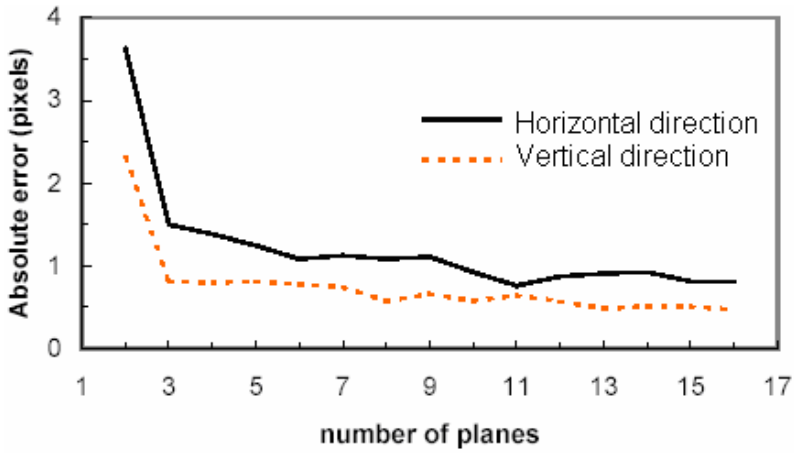

Figure A.3 Required number of planes in camera calibration process

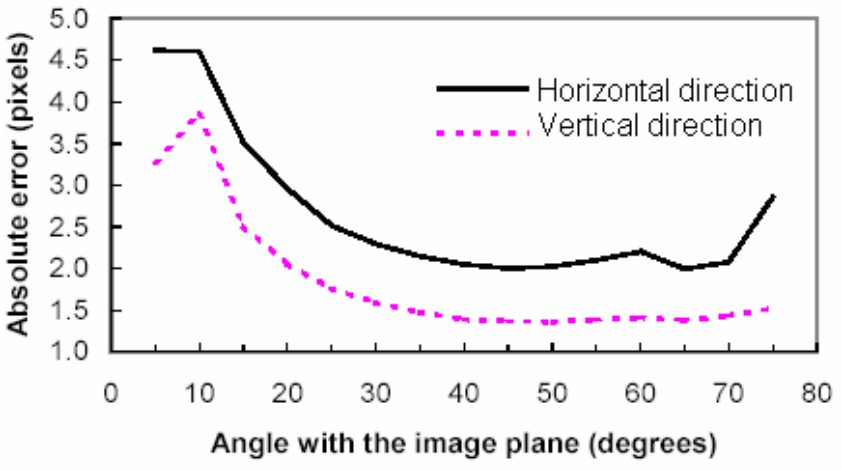

Figure A.4 Required angle with the image planes in camera calibration process

Camera calibration process in present study was made by following the methodology explained before using Camera Calibration Toolbox for Matlab, Jean-Yves Bouguet, MRL - Intel Corp [77]. The C implementation of this toolbox is included in the Open Source Computer Vision library distributed by Intel (http://www.intel.com/research/mrl/research/opencv/index.htm) and freely available online.

This toolbox was installed into the Matlab 6.5 on Windows and used for camera calibration process.

A.1.1. Corner extraction of calibration images

For camera/lens configuration used in the study, eleven photographs of a calibration object were taken. A flat checkerboard patterned plate is used as a calibration object (Figure A.5), and is used to recover the pattern of radial distortion from the images.

To obtain re-projection parameters more image processing operations are needed. The most important step of these operations is corner extraction phase.

The checkerboard corners provide many sets of points which are collinear in the world. In fact, these sets of points can be found in many orientations, including horizontal, vertical, and diagonal.

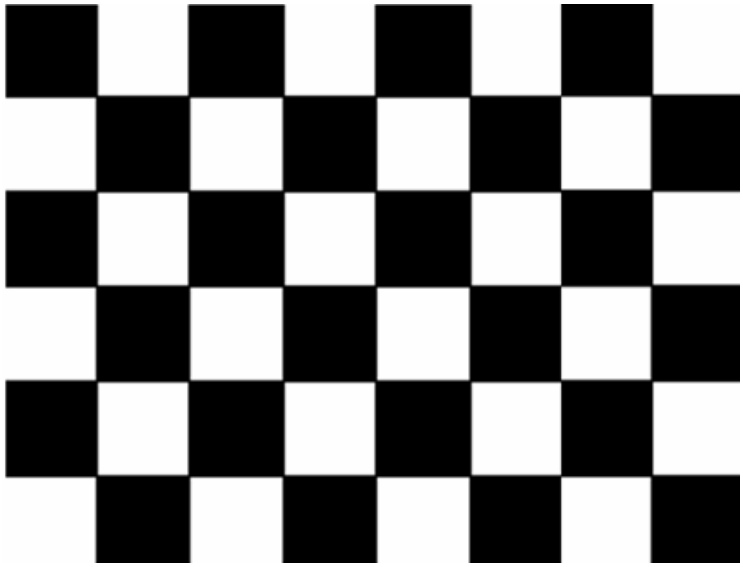

Figure A.5 Calibration image

Using the corner extraction engine in the toolbox, image corners were extracted to an accuracy of about 0.4 pixels (Figure A.6).

After corner extraction, Calibration data file is automatically generated. This file contains all the information gathered throughout the corner extraction stage (image coordinates, corresponding 3D grid coordinates, grid sizes, etc.). After that, calibration was done using the calibration option of the toolbox.

Re-projection error due to lens distortion can be obtained easily from the calibration data (Figure A.7).

In order to make a decision on the appropriate distortion model to use, it is sometimes very useful to visualize the effect of distortions on the pixel image, and the importance of the radial component versus the tangential component of distortion. For this purpose, distortion models are plotted in Figure A.9, Figure A.10 and Figure A.11.

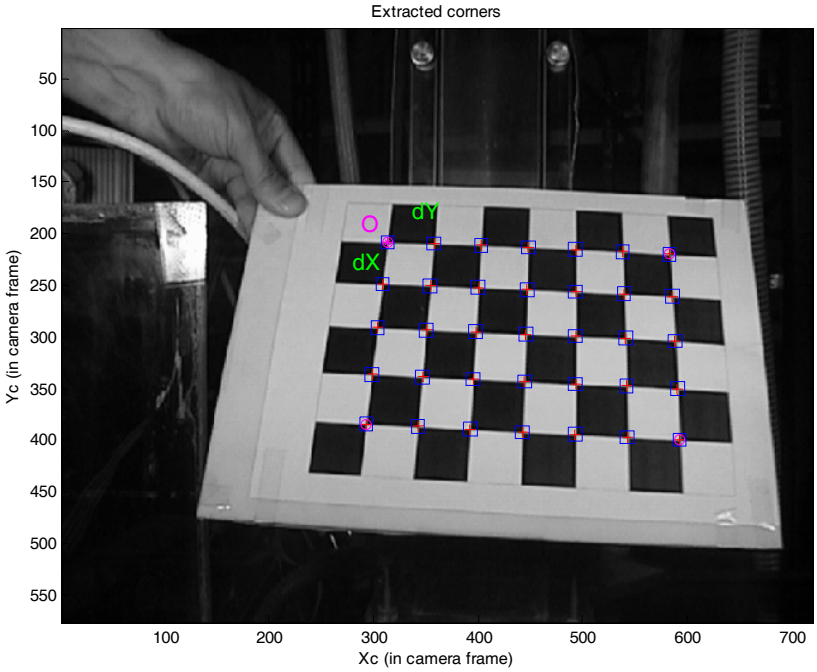

Figure A.6 Corner extraction phase

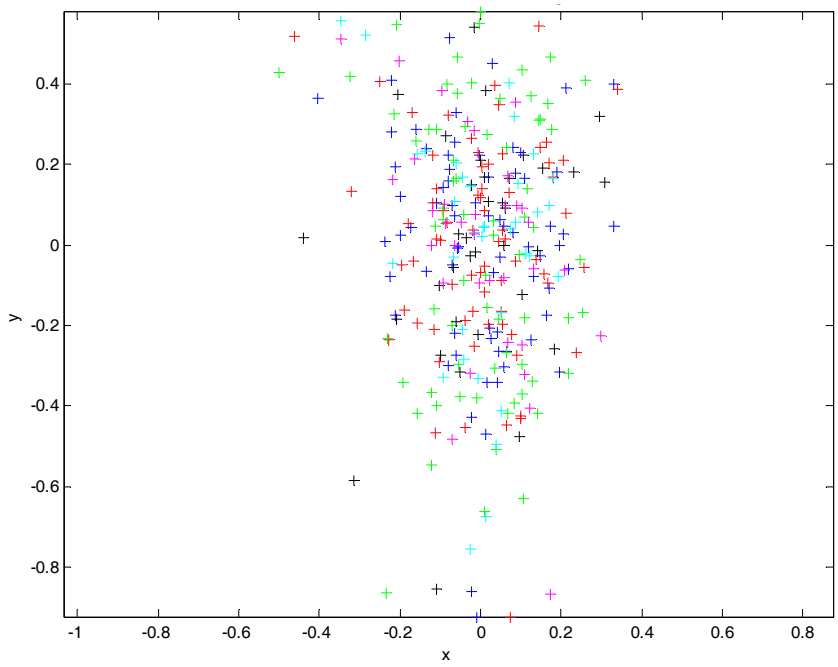

Figure A.7 Re-projection error due to lens distortion

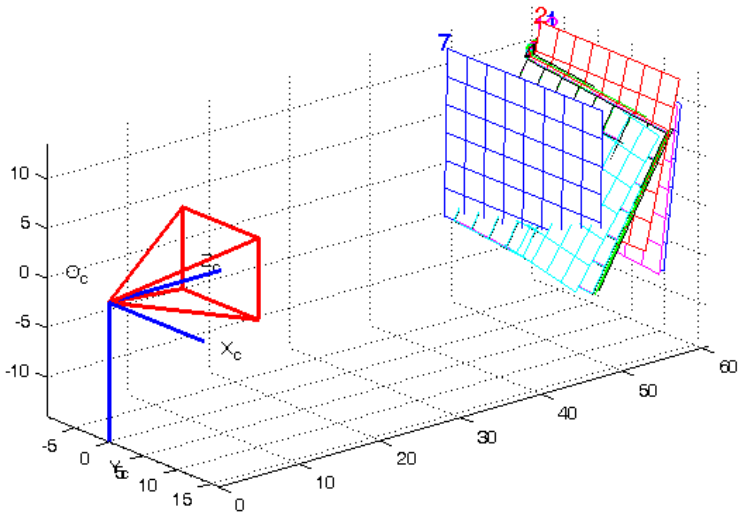

Figure A.8 Extrinsic camera parameters

Figure A.9 shows the impact of the complete distortion model (radial + tangential) on each pixel of the image. Each arrow represents the effective displacement of a pixel induced by the lens distortion. It can be seen from the figure that points at the corners of the image are displaced by as much as 25 pixels. Figure A.10 shows the impact of the tangential component of distortion. On this figure, the maximum induced displacement is 0.14 pixels (at the upper left corner of the image). Finally, Figure A.11 shows the impact of the radial component of distortion. This plot is very similar to the full distortion plot, showing the tangential component could very well be discarded in the complete distortion model. On the three figures, the cross indicates the center of the image, and the circle the location of the principal point.

Camera calibration parameters are as follows;

Focal Length:	[881.68 961.92] ± [26.11 28.80]
Principal point:	[369.66 310.11] ± [14.32 14.67]
Skew:	[0.00] ± [0.00] angle of pixel axes = 90 degrees
Distortion:	[-0.27 0.45 0.00 0.00 0.00] ± [0.08 0.91 0.00 0.00 0.00]
Pixel error:	[0.15443 0.24467]

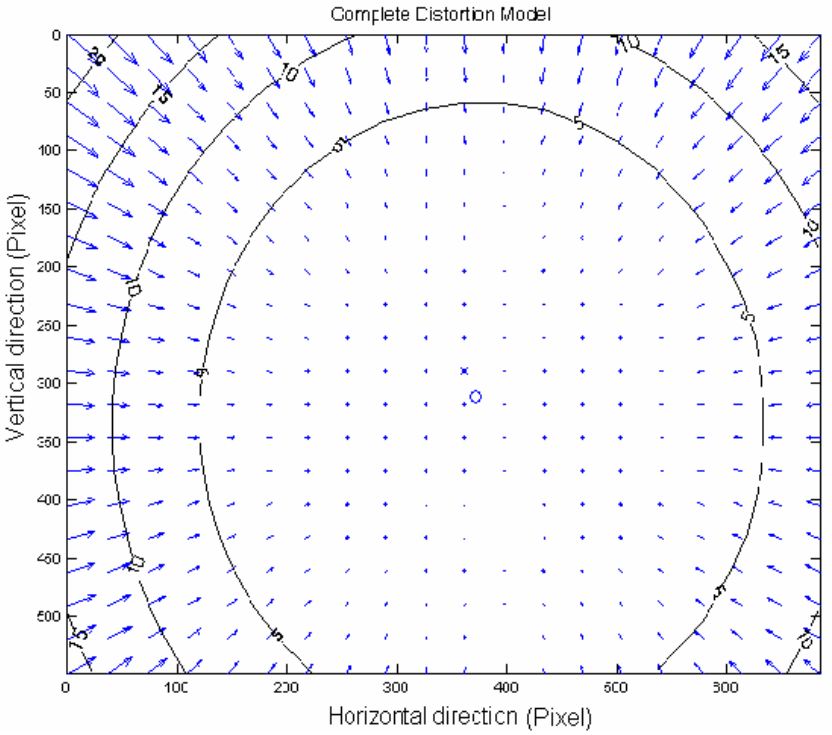

Figure A.9 Complete distortion model

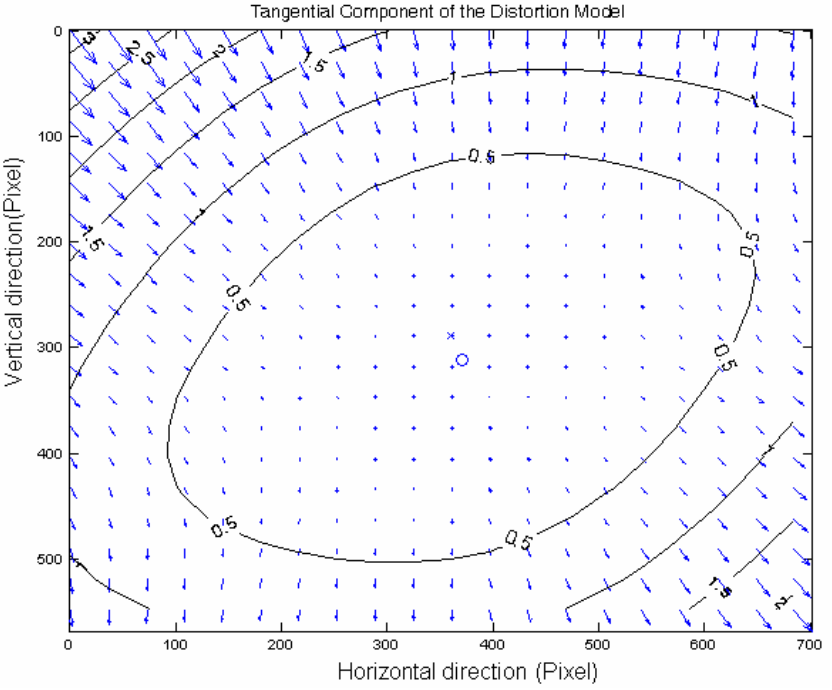

Figure A.10 Tangential component of the distortion model

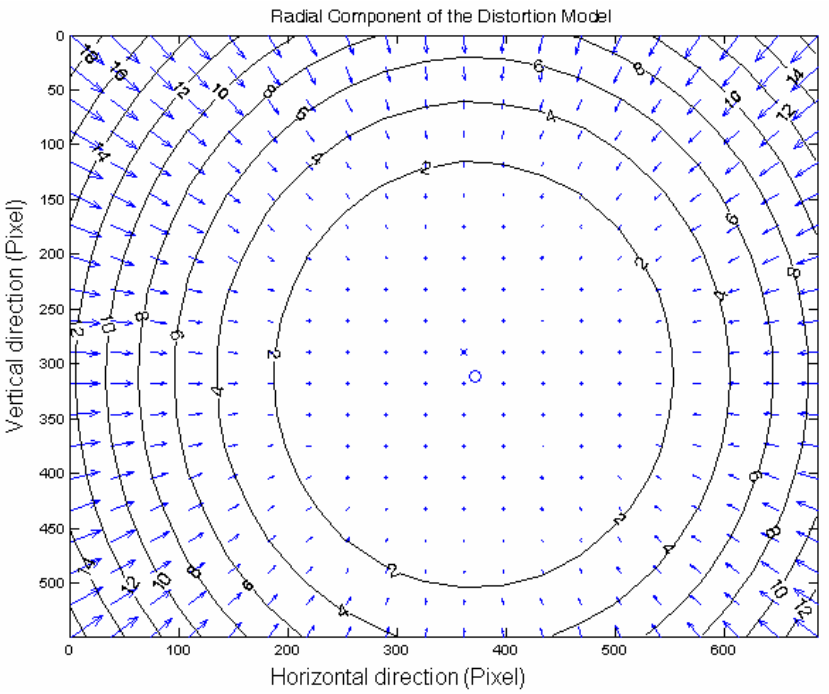

Figure A.11 Radial component of the distortion model

Once the distortion parameters are solved for, it is possible to undistort any image taken with the same lens as the calibration images. Raw video images can be calibrated by using obtained camera calibration parameters.

Calibration data were exported to Zhang [78] format as extracted image corners and associated 3D world coordinates. These corner points were then used as input to the *EasyCalib* software [79].

As a test of the radial distortion calibration, one can undistort the calibration images themselves and see if the original straight lines become straight. Figure A.12 shows the original checkerboard calibration image, and just below the results of undistorting the original checkerboard image in Figure A.13. Straight lines in the calibration images are a bit bowed in Figure A.12.

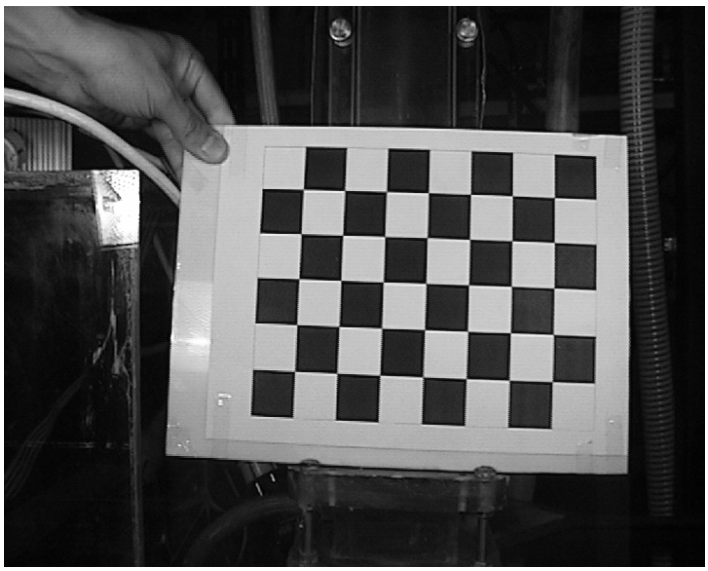

Figure A.12 The distorted original calibration image

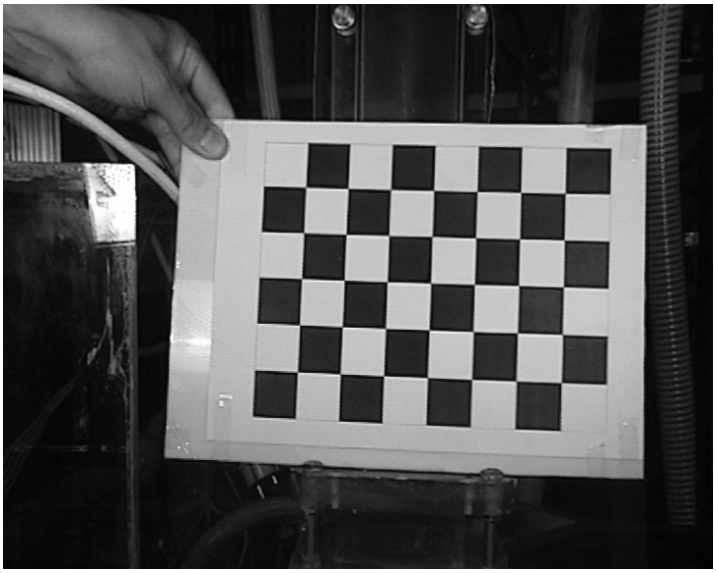

Figure A.13 The undistorted calibration image

APPENDIX B

UNCERTAINTY ANALYSES

When a quantity is measured directly in an experiment, its uncertainty can be determined by the accuracy of the instrumentation used. When a quantity Y is not measured directly, but is rather calculated as a function of one or more variables that are measured directly, i.e.,. $Y = f(X_1, X_2, \ldots)$, the uncertainty of Y is then given as:

$$\delta Y = \sqrt{\sum_i \left(\frac{\partial Y}{\partial X_i} \right)^2 \delta X_i^2} \tag{B.1}$$

Where δ represents the uncertainty of the variable, and δX_i is the uncertainty of the X_i.

The major quantities measured or calculated in this work include the bubble diameter, perimeter, area, volume and rising velocity and mean water velocity. In addition to these quantities, Reynolds, Eötvös and Weber numbers related to air bubbles are calculated. Their uncertainties are given according to Eq. B1.

Important parameters used for the calculation of uncertainties:

- Frame rate = 1/ 25 ; time difference between two consecutive frames= 0,04 s
- One pixel length = 0.029 cm
- Shutter speed = 1/4000 s
- The recording frequency = 25 frames/s
- Maximum bubble terminal velocity ≈ 24 cm/s
- Mean water velocities are 0, 2.15, 11, 21, and 25 cm/s

7.4 B.1. Uncertainties in the experimental data

B.1.1. Bubble rising velocity

Maximum error in water properties (density, viscosity, surface tension) due to water temperature difference (1^oC temperature difference – (See Figure 5.7) is ± 0.1 % and hence, it is negligible. The temperature change effect on bubble rise velocity is less than 1%, so this effect can be ignored.

Maximum uncertainty in bubble diameter due to image recording resolution;

δ_d = ± 1 pixel length = ± 0.029 cm

$$\delta_d/d_{ae} = \pm [0.029 \text{ cm} / d_{ae}(\text{cm})] \quad \text{(B.2)}$$

For 0.3 cm < d_{ae} < 7 cm, 0.4% < δ_d/d_{ae} < 9.7%

Maximum uncertainty in bubble perimeter due to image recording resolution;

$\delta_P = \pi\delta_d$,

$$\delta_P/P = \pm [0.029 \text{ cm} / d_{ae}(\text{cm})] \quad \text{(B.3)}$$

For 0.942 cm < P < 21.98 cm, 0.4% < δ_P/P < 9.7%

Maximum uncertainty in bubble area due to image recording resolution;

$\delta_A = \pi d_{ae}\delta_d/2$,

$$\delta_A/A = \pm [0.058 \text{ cm} / d_{ae}(\text{cm})] \quad \text{(B.4)}$$

For 0.07 cm^2 < A < 38.46 cm^2, 0.83% < δ_A/A < 19.4%

Maximum uncertainty in bubble volume due to image recording resolution;

Uncertainty in volume calculations due to area and perimeter uncertainty can be calculated using Eq. 5.1 and Eq. B.1. As a result, maximum error due to this assumption is as follows;

$$\delta V = \sqrt{0.000091 d_{ae}^2 + 0.0000126} \quad \text{(B.5)}$$

$$\frac{\delta V}{V} = \frac{\sqrt{0.000091 d_{ae}^2 + 0.0000126}}{0.165 d_{ae}^2 - 0.1225 d_{ae}} \quad \text{(B.6)}$$

For 0.3 cm < d_{ae} < 7 cm, 1% < $\delta V/V$ < 20.8%

The distortion on the bubble shape image due to shutter speed when the bubble is moving with its terminal speed

U_b x Shutter speed=24/4000 = 0.006 cm (it is negligible)

Maximum uncertainty in the distance traveled by the bubble between two consecutive frames, due to image recording resolution;

δ_z = ± 1 pixel length = ± 0.029 cm

Maximum error might occur in bubble velocity (U_b) calculations due to the uncertainty in the distance traveled by the bubble between two consecutive frames;

δU_b = δ_z / 0.04 s = ± 0.8 cm/s,

$$\delta U_b/U_b = \pm 0.8 / U_b \quad \text{(B.7)}$$

For 15 cm/s < U_b < 24 cm/s, 3.34 < $\delta U_b/U_b$ < 5.34%

B.1.2. Mean water velocity

Mean water velocity is calculated using mass flow rate data which is measured by weighing the discharged water for a period of time.

$$\dot{m} = \rho U_l A \quad \text{(B.8)}$$

$$U_l = \frac{\dot{m}}{\rho A} \quad \text{(B.9)}$$

Table B.1 Uncertainty of mean water velocity

U_l(cm/s)	m (gr)	*time* (s)	δm	δt	$\dot{m}$	$\delta\dot{m}$	A(cm^2)	δA	δU_l	δU_l%
2.15	540	180	20	1	3.00	0.11	1.4	0.07	0,134	6
11	2760	180	20	1	15.34	0.14	1.4	0.07	0,55	5
21	5250	180	20	1	29.17	0.20	1.4	0.07	1,06	5
25	6300	180	20	1	35.00	0.22	1.4	0.07	1,27	5

As it can be seen from Table B.1, uncertainty of mean water velocity is 5% except 2.2 cm/s case.

B.1.3. Dimensionless numbers

Maximum error might occur in bubble Reynolds number calculations due to uncertainties in the related parameters;

$$\mathrm{Re}_b = \frac{\rho_l U_b d_{ae}}{\mu_l} \tag{B.10}$$

Because the maximum error might occur in water density and dynamic viscosity is negligible, the error comes from the uncertainty in bubble diameter and bubble rise velocity.

$$\delta_{\mathrm{Re}} / \mathrm{Re} = \pm \frac{\sqrt{d_{ae}^2 \delta U_b^2 + U_b^2 \delta d_{ae}^2}}{U_b d_{ae}} \tag{B.11}$$

$$\delta_{\mathrm{Re}} / \mathrm{Re} = \pm \frac{\sqrt{0.64 d_{ae}^2 + 0.00084 U_b^2}}{U_b d_{ae}} \tag{B.12}$$

For 0.3 cm < d_{ae} < 7 cm, and 15 cm/s < U_b < 24 cm/s, 3.34% < δ_{Re}/Re< 11%

Maximum error might occur in bubble *Eö* number calculations due to uncertainties in the related parameters;

$$E\ddot{o} = \frac{g {d_{ae}}^2 \left(\rho_l - \rho_g\right)}{\sigma} \tag{B.13}$$

Because the maximum error in determination of water properties is negligible, the error comes from the uncertainty in bubble diameter measurement.

$$\delta_{E\ddot{o}} / E\ddot{o} = \pm \frac{2\delta d_{ae}}{d_{ae}} \tag{B.14}$$

$$\delta_{E\ddot{o}} / E\ddot{o} = \pm \frac{0.058}{d_{ae}} \tag{B.15}$$

For 0.3 cm < d_{ae} < 7 cm, , 0.83% < $\delta_{E\ddot{o}}/E\ddot{o}$< 19.34%

Maximum error might occur in bubble *We* number calculations due to uncertainties in the related parameters;

Because the maximum error in determination of water and air properties is negligible, the error comes from the uncertainty in bubble diameter and bubble rise velocity measurement.

$$We = \frac{\rho_l U_b^2 d_{ae}}{\sigma} \tag{B.16}$$

$$\delta_{We} / We = \pm \frac{\sqrt{4 d_{ae}^2 \delta U_b^2 + U_b^2 \delta d_{ae}^2}}{d_{ae} U_b^2} \tag{B.17}$$

$$\delta_{We} / We = \pm \frac{\sqrt{2.56 d_{ae}^2 + 0.00084 U_b^2}}{d_{ae} U_b^2} \tag{B.18}$$

For 0.3 cm < d_{ae} < 7 cm, and 15 cm/s < U_b < 24 cm/s, 0.04% < δ_{We}/We < 3.2%

CURRICULUM VITAE

PERSONAL INFORMATION

Surname, Name : Sancak ÖZDEMİR
Nationality : Turkish (TC)
Date and Place of Birth : 2 January 1972, Ardahan
Marital Status : Married
Telephone : +90 312 2871529 Ext: 1818
Fax : +90 312 2859055
E-mail : sancak.ozdemir@taek.gov.tr

EDUCATION

Degree	Place	Years of Graduation
M.Sc.	HU Nuclear Energy Engineering, Ankara	1998
B.Sc.	HU Nuclear Energy Engineering, , Ankara	1994
Electrician Diploma	Demirtaşpaşa EML, Bursa	1988

FOREIGN LANGUAGES

English

COMPLETED INTERNATIONAL COURSES:

"Regional Training Course on the Safety of Research Reactor Facilities" IAEA 28.09.1998 – 16.10.1998, Czech Republic

"Nuclear Power Generation" Basic Course, 06 January - 02 March, 2004, Japan

"Nuclear Leadership", World Nuclear University, Summer Institute, 10 July – 20 August 2005, Idaho Falls, USA

PROFESSIONAL WORK HISTORY

Years of service	Place	Title of position
1994-1995	Hacettepe University	Teaching Assistant
1995-Present	Turkish Atomic Energy Authority	Nuclear Engineer

PUBLICATIONS AND SEMINARS

1. Özdemir S., Çubukçu, E. "Analysis of Uranium-Thorium Fuel Cycle in CANDU-600", September, 1996, VII. National Nuclear Sciences and Technologies Symposium, İstanbul, Turkey
2. Özdemir, S., Master Thesis, "Once through Uranium-Thorium Fuel Cycle in CANDU Reactors", 1998 Ankara, Turkey
3. Özdemir, S., "Once Through Uranium-Thorium Fuel Cycle in CANDU Reactors", Nuclear Option in Countries with Small and Medium Electricity Grid, 19-22 June 2000, Dubrovnik, Croatia
4. Özdemir, S., "Regulatory Influence on Safety Culture at TR-2 Research Reactor (Preliminary Survey Results)", IAEA-Technical Meeting, Vienna, December 2004
5. Bezdegümeli U., Yeşin O., Özdemir S. "Motion of Air Bubbles in Stagnant Water Condition", The Third Eurasian Conference, Nuclear Science and Its Application, October 5-8, 2004, Uzbekistan

HOBBIES

Volleyball, Table Tennis, Photography, Computer and Communication Technologies